ALGORITHMS AND PERFORMANCE ANALYSIS FOR INDOOR LOCATION TRACKING SYSTEMS

YUNYE JIN

(*B. ENG. (Hons.), NUS*)

A THESIS SUBMITTED FOR THE DEGREE OF

DOCTOR OF PHILOSOPHY

DEPARTMENT OF ELECTRICAL AND COMPUTER ENGINEERING

NATIONAL UNIVERSITY OF SINGAPORE

2011

To my parents.

Acknowledgements

I would like to express my heartfelt gratitude to my supervisor, Prof. Soh Wee-Seng, for his continuous guidance and support during my Ph. D. candidature. His insights, knowledge, patience, and enthusiasm have provided great inspirations and set an admirable example for me. He has generously devoted his time and efforts to this thesis, without which its completion would not be possible.

I would like to express my utmost appreciation to my co-supervisor, Prof. Wong Wai-Choong, Lawrence, for always providing me with motivational thoughts and ideas during our discussions. His experience and expertise across various fields have broaden my perspective and extended my dimensions of thinking.

My sincere thanks also goes to Prof. Mehul Motani, for not only his teaching as my lecturer of the computer networks module, but also the collaborations and discussions we had during several research projects and demos, which have greatly benefited me.

I am grateful to Prof. Hari Krishna Garg and Prof. Marc Andre Armand, for their time and efforts in assessing my research work, for the valuable suggestions and critical questions during my qualification examination.

I must thank NUS for financially supporting my study and research through the NUS Research Scholarship.

I am deeply indebted to my parents back in China, who have never lost faith

in me. They have always been there for me with their love and care, during the ups and downs of the past four years.

I would like to thank the lab officers, Mr. Song Xianlin, Mr. Goh Thiam Pheng, and Mr. Siow Hong Lin, Eric, for their help and assistance during all my research projects.

Last but not least, I would like to thank all my colleagues and lab mates in NUS ECE Communications Lab and IDMI Ambient Intelligence Lab.

Summary

The ability to accurately track a user's location in the indoor environment has many applications in the healthcare, logistic, and entertainment industries. This thesis makes a threefold contribution to the realization and analysis of practical indoor location tracking systems.

First, we propose an efficient channel-impulse-response-based (CIR-based) location fingerprint, derived from receiver channel estimation results. Logarithmic transformation is applied to ensure that each element in the fingerprint vector contributes fairly towards the location estimation. Simulation results show that, with the same number of access points and the same amount of training efforts, the proposed method significantly outperforms the existing fingerprint-based methods in the literature. It is also robust to the environmental changes caused by the presence of a crowd of human bodies.

Second, we derive the exact theoretical expressions of both the online error probability density function (PDF) and region of confidence (RoC) for a generalized location fingerprinting system. Computations of both terms require the joint PDF for the location and the online signal parameter vector, which is practically unknown. We therefore propose to approximate this joint PDF by nonparametric kernel density estimation using the training fingerprints, without extra calibration efforts. Experimental results show that, the proposed scheme predicts the empir-

ical error PDF closely for the two most popular location fingerprinting methods, namely, the K nearest neighbour (KNN) and the probabilistic approach.

The third contribution includes two different approaches that we propose to realize a robust pedestrian tracking system using mobile devices with low cost sensors. The first approach fuses the estimates of a dead-reckoning (DR) system with the measurements of a sparsely deployed ranging infrastructure, using a particle filter (PF). Experimental results show that this approach significantly reduces DR tracking error even when (i) initial location is unknown, (ii) range measurements have errors, (iii) range updates are intermittent and sparse both temporally and spatially. The second approach fuses the estimates of two DR modules, carried by the same pedestrian and mounted with stable relative displacement, through a maximum a posteriori estimation scheme. Experimental results show that, the proposed scheme delivers robust tracking performance, with significantly smaller average error compared to traditional DR methods, when using (i) two DR modules, each with a single orientation sensor and arbitrary device orientation, (ii) one DR module, with two different orientation sensors and fixed device orientation.

Contents

List of Figures

List of Tables

List of Symbols

Symbol	Meaning
N_{sc}	number of sub-carriers in OFDM
$\tau_{\max}$	maximum excess delay of indoor channel
BW	system bandwidth
M	number of APs in the service area
$i,\ j,\ k,\ n$	indices
$\mathbf{s}_i$	the i^{th} training fingerprint vector.
$\mathbf{c}_i$	coordinates vector of the location where $\mathbf{s}_i$ is collected
N_{tr}	number of training records
$\mathbf{s}$	online fingerprint vector
D	dimension of a vector
$\mathbf{R_s}$	sample covariance matrix of the training fingerprint vectors
$\mathbf{c}$	location coordinates of the target device
$\hat{\mathbf{c}}$	estimator for the location coordinates of the target device
$E\{\cdot\}$	expected value
$f(\cdot)$	probability density function
$K(\cdot)$	kernel function
$\exp(\cdot)$	exponential function

Symbol	Meaning
$\log(\cdot)$	logarithm function
$\mathbf{H}$	bandwidth matrix
$\lvert\mathbf{H}\rvert$	determinant of the matrix $\mathbf{H}$
$\mathbf{h}$	decimal scale training ACIR vector
$\mathbf{g}$	decimal scale online ACIR vector
T_s	symbol duration
$z(t)$	the transmitted signal
$\lvert z(t)\rvert^2$	instantaneous power of the signal $z(t)$
$a(\cdot),\ b(\cdot)$	channel gain due to propagation pass loss and antenna characteristics
P_0	transmission power
P_n	received power at time instant nT_s, considering only pass loss and antenna characteristics
T	time period over which power is being measured
d	distance travelled by the signal
v_{RF}	propagation speed of the RF signal
G_{tx}	transmitter antenna gain
G_{rx}	receiver antenna gain
λ	carrier wavelength
$\alpha(\cdot),\ \beta(\cdot)$	channel gain due to penetrations, reflections, and diffractions
$\epsilon_{\mathrm{Re}},\ \epsilon_{\mathrm{Im}}$	real and imaginary part of the relative permittivity
$\mathbf{u}_i$	concatenated vector for the i^{th} fingerprint vector and the i^{th} training location coordinates
$\mathbf{u}$	concatenated vector for the online fingerprint vector and the target location coordinates

Symbol	Meaning
$\hat{f}(\cdot)$	estimation of the PDF $f(\cdot)$
ω	a scalar for pilot density estimation
$\mathbf{R}$	sample covariance matrix computed using training records
$\bar{f}'$	geometric mean of the pilot PDF estimation values
$\mathbf{\Phi}$	sub-covariance-matrix
$\mathbf{e}$	vector of location error
η	location error distance
γ	location error angle
$\mathbf{J}$	Jacobian matrix
Pr	probability
N_{te}	number of testing samples
S_{te}	set of testing samples
$\mathbf{l}$	vector of pedestrian location coordinates
ρ	average stride length
θ	stride orientation
$\Delta_{\text{threshold}}$	threshold for step detection
σ_ρ	standard deviation of the error in stride length estimate
σ_θ	standard deviation of the error in stride orientation estimate
b_k	index of the BN from which the k^{th} measurement is taken
μ_k	actual pedestrian-BN separation
σ_r	standard deviation of the error in range measurements
N_s	number of particle filter samples

Symbol	Meaning
N_k	number of steps taken between the $(k-1)^{\text{th}}$ and the k^{th} range measurements
w_j	weight of the j^{th} sample
$\mathbf{l}_k^j$	the j^{th} sample
$\propto$	proportional to
$\delta(\cdot)$	Dirac-Delta function
$A,\ B$	labels for two DR modules
$\mathbf{v}_i$	noise vector
κ	value of a uniform density
ϕ	angle of the displacement between two DR modules
$\mathbf{q}$	displacement vector between two DR modules
$F,\ Q,\ G$	temporary functions
$\mathbf{R}_A,\ \mathbf{R}_B$	covariance matrices of module A and B's location estimates
$\mathbf{I}$	identity matrix

Chapter 1

Introduction

1.1 Background

The ability to accurately track a user's location in the indoor environment has many applications in the healthcare, logistic, and entertainment industries. In an ambient-intelligent environment, obtaining accurate user location information not only facilitates the association of computational resource with the user but also enables the invocation of relevant services based on the user context.

The Global Positioning System (GPS) is the dominating technology in the market of outdoor location tracking. However, the signal of GPS is either entirely blocked by walls and ceilings or severely deteriorated by multipath propagation in the indoor environment. On the other hand, state-of-the-art cellular-network-based methods typically deliver an accuracy at the scale of hundreds of meters [1], which is unacceptable for many real-world indoor applications. Therefore, accurate indoor location tracking must rely on other technologies and infrastructure.

The past decade has witnessed the proliferation of indoor wireless communication infrastructure and the emergence of commercially accessible personal mobile

devices with various sensors and multi-modal communication capabilities. These advances have created new opportunities for the realization of cost-effective *practical* indoor location tracking systems.

1.2 Overview of Existing Indoor Location Tracking Systems

In this chapter, we classify the practical indoor tracking methods into three categories according to their dependence on infrastructure, namely, methods that rely on dedicated extra infrastructure, methods that rely on the existing infrastructure, and methods that rely on the target device itself (Dead-Reckoning). We briefly introduce them with an emphasis on their limitations and difficulties.

1.2.1 Methods Based on Dedicated Infrastructure

The Radio Frequency Identification (RFID) technology has been widely used as dedicated infrastructure for indoor location tracking, especially for autonomous robots [2, 3]. However, such a system requires the dense installation of RFID tags on the floor of the service area. The setup is very expensive in terms of not the tags themselves but the labor input.

Another approach that usually requires dedicated infrastructure is the geometric location tracking methods in the indoor environment. For distance based methods such as Time-of-Arrival (ToA) and Time-Difference-of-Arrival (TDoA), wireless technologies such as ultrasound [4], ultra-wide-band (UWB) [5], wideband with enhanced sampling rate [6] are employed in order to provide satisfactory resolution in time, and hence distance measurements. However, transceivers in such dedicated infrastructure normally covers limited range due to concerns such as

interference control and power conservation.

On the other hand, direction based practical indoor tracking methods rely heavily on the directionality of the antenna. Directionality is achieved by either using a multi-element antenna array [7] in conjunction with computationally intensive algorithm such as MUltiple SIgnal Classification (MUSIC) [8] or a single antenna with actuated reflector [9]. In both ways, the system cost is high in terms of hardware and overhead.

For both distance and direction based methods, in the heavy presence of indoor Non-Line-of-Sight (NLoS) propagation conditions, full location tracking coverage of the indoor service area requires a huge number of such range-limited transceivers, which further incurs high hardware cost.

1.2.2 Methods Based on The Existing Infrastructure

IEEE 802.11 (Wi-Fi) is the most widely adopted wireless communication technology in indoor and urban environments. While providing high speed wireless data access, it also enables the design and implementation of practical indoor location tracking systems on top of existing infrastructure with minimum extra interference.

Among the practical location tracking methods which utilizes the Wi-Fi infrastructure, a small subset adopts the geometric trilateration methods such as ToA [10, 11] or TDoA [6], which require extra hardware modifications or additions to the commercially-accessible Wi-Fi adapters. On the other hand, the majority of the practically implemented Wi-Fi based methods take the fingerprint-based approach, which involves an off-line training phase during which the indoor Wi-Fi received signal strength (RSS) are collected as location fingerprints in the service area [12]. A major drawback of this approach is the heavy labor cost during

the training phase, especially for large service areas. Moreover, after the training phase is completed, this approach is vulnerable to the environmental changes, caused by change of room layout or movement of the crowd.

1.2.3 The Dead-Reckoning Approach

More and more mobile hand-held devices are equipped with low cost MEMS sensors, such as accelerometer, magnetometer, and gyroscope, for purposes such as, flexible user interface orientation, navigation, gaming, and augmented reality. Availability of such sensors has made Dead-Reckoning (DR) a preferable choice for indoor pedestrian tracking.

The DR approach iteratively estimates the current location by adding the estimated displacement to the previously estimated location. In contrast to the afore-mentioned approaches, in which both the target device and the infrastructure deployment are indispensable parts of the tracking system, the DR tracking scheme is almost self-contained in the target device alone (except for the initialization phase). A major drawback of such a system is that, the errors in the estimated displacement accumulate quickly over time because of the iterative nature of estimation. Moreover, compared to using dedicated sensor modules which are fixed at pedestrian body with convenient location and orientation (foot, or center back of waist) for tracking, DR with hand-held device suffers more noise and disturbance due to irregular movements and shifts of the upper body and the arm of the pedestrian.

1.3 Research Emphasis and Contributions

Based on the overview of the existing approaches, we observe that, although the approaches based on the existing infrastructure and hand-held device have various problems and limitations, they are still attractive options upon which practical and robust indoor location tracking methods can be developed, owning to their accessibility and cost-effectiveness. The research contribution of this thesis is threefold, as described in the following sub-sections.

1.3.1 Channel Impulse Response Based Fingerprinting

In order to reduce hardware cost and RF interference, it is desirable to construct a fingerprint-based localization system based on the existing indoor wireless infrastructure, in which a small number of access points (APs) are deployed to provide communication coverage over a large area. Because each AP in such a system contributes only one dimension to the RSS fingerprint vector, the resulting fingerprint vector dimension may be too low to distinguish locations over a large area.

In this thesis, we propose a novel location fingerprint based on the amplitudes of the approximated channel impulse response (ACIR) vector. The ACIR has much higher dimension with the same number of APs compared to the RSS fingerprint. The high dimension and the strong location dependency have given the ACIR higher capability to distinguish locations. We then transform the ACIR into logarithmic scale to ensure that each element within the fingerprint vector contributes fairly to the location estimation. Nonparametric Kernel Regression (NKR) method with a generalized bandwidth matrix formula is applied for location estimation. Using a realistic indoor propagation simulator, our results suggest

that the proposed fingerprint and its associated signal processing technique outperform other fingerprint-based schemes found in the literature, with the same amount of training efforts, under various indoor conditions.

1.3.2 Error Analysis of Fingerprint-based Methods

Compared to the large number of proposals on fingerprint-based localization methods, there are very few works which study the theoretical online error analysis of fingerprint-based localization systems, while taking the current online RSS vector into account.

In this thesis, we derive the exact theoretical expressions of both the online error probability density function(PDF) and Region of Confidence (RoC), conditioned on the observed online RSS vector, for a fingerprint-based localization system. As the computations of the relevant terms require exact knowledge of the joint PDF for the location and the online RSS vector, which is practically not available, we approximate this joint PDF by Nonparametric Kernel Density Estimation (NKDE) techniques using the training fingerprints, without any extra calibration efforts. Experimental results show that the proposed method closely predicts the performance of two widely adopted fingerprint-based schemes.

1.3.3 Robust DR-Based Pedestrian Tracking Methods

Despite the intrinsic cumulative tracking error, DR is still a very attractive option for indoor pedestrian tracking due to the high accessibility of hand-held mobile devices nowadays. In this thesis, we propose two robust DR-based pedestrian tracking methods that reduce and constrain the cumulative tracking error for hand-held mobile devices.

DR-based Robust Pedestrian Tracking with Sparse Infrastructure

In the first approach, we propose an indoor pedestrian tracking system which fuses the DR estimate with range measurements from a sparsely deployed ranging infrastructure. We propose a particle-filter-based (PF-based) sensor fusion scheme to reduce and constrain the tracking error for the general case in which the reporting rate and accuracy of the ranging system may vary. A prototype of the proposed scheme is implemented for experimental verification with sensors on a hand-held device and a practical ranging system. As our experimental results will show, the proposed scheme is able to provide significantly better tracking performance compared to a DR system alone, regardless of whether the knowledge of initial user location is available or not. Moreover, even when the range measurements are noisy and intermittent, both spatially and temporally, our proposed system still delivers fairly accurate tracking performance.

DR-based Robust Pedestrian Tracking with Two Devices

The second approach that we propose for robust pedestrian tracking exploits the fact that, when two sets of DR sensors are carried by the same pedestrian, they have small and limited local random motions, as well as stable relative displacements to each other, which can be utilized to reduce the overall DR tracking error. We formulate the robust tracking task as a maximum a posteriori (MAP) sensor fusion problem and derive the optimal solution with simplifications for computation. We also narrow the generalized algorithm to a special case in which there is only one physical device, containing two different orientation sensors. We implemented prototypes of our proposed system with commercially-accessible mobile devices, and also an effective system for ground truth collection indoors. Through experiments, we evaluate our proposed scheme by using, (i)two DR modules, each

containing a single orientation sensor, mounted with arbitrary device orientations, (ii)one DR module, containing two different orientation sensors, mounted with fixed device orientation. The proposed scheme exhibits robust tracking performance with much lower average tracking errors compared to the traditional DR method, in both scenarios.

1.4 Organization of the Thesis

The thesis is organized in the following manner. Chapter 2 summarizes the related work in the literature of indoor location tracking, categorized according to their working mechanism. Chapter 3 describes our proposed CIR-based location fingerprint and its associated signal processing techniques, with simulation verifications. Chapter 4 describes our proposed theoretical error analysis method for location fingerprinting system, with experimental verifications. In Chapter 5, we propose a DR-based robust pedestrian tracking approach which utilizes a sparse ranging infrastructure for cumulative error reduction. We also include a brief introduction of DR tracking with hand-held devices. In Chapter 6, we propose a different DR-based robust pedestrian tracking approach which exploits the stable relative displacements between two DR modules. We also include a brief introduction of DR tracking with arbitrary device orientation. In Chapter 7, we conclude the thesis and point out future directions.

Chapter 2

Literature Review

In this chapter, we classify the practical indoor tracking methods in the literature into four categories according to their working mechanism, namely, the geometric approach, the fingerprint-based approach, the DR approach, and the hybrid approach, which combines DR with external technologies.

2.1 The Geometric Approach

2.1.1 DoA Based Methods

A typical DoA system locates the target device by estimating the direction of the arrival signal transmitted by the target device, as shown in Fig. 2.1. Algorithms such as MUSIC [8] and ESPRIT [13] have been present in the field of outdoor DoA based localization for decades. The successes of these methods rely on two important assumptions which are normally valid in the outdoor scenario [14]. First of all, there must be a direct Line-of-Sight (LoS) path between the transmitter and receiver. Second, the multiple signals which impinge on the

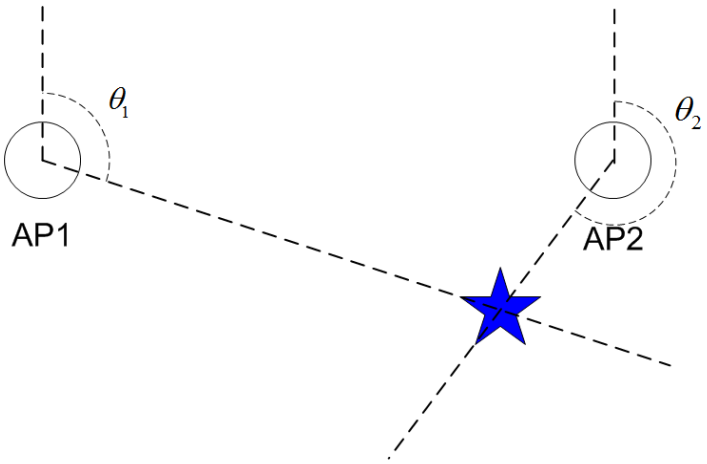

Fig. 2.1: Triangulation with DoA.

receiver antenna array are usually assumed to be uncorrelated (incoherent). However, in the context of indoor localization, these assumptions often break. Even in the situation where the LoS condition is fulfilled, the multi-path versions of the same transmitted signal are perfectly coherent since they are scaled and delayed versions of each other. Additional computation such as sub-array smoothing must be applied to resolve this issue [14, 15].

Recent proposals of practical indoor DoA methods rely heavily on the special enhancements and configurations of antennas. For example, in [7], a six-element switched-beam antenna system is mounted on the ceiling. The computationally-intensive MUSIC algorithm is applied for direction finding. [9] uses an actuated reflector and a omni-directional antenna in order to find the orientation of the strongest received signal strength. Overall, even under LoS conditions, such practical DoA solutions are expensive in hardware.

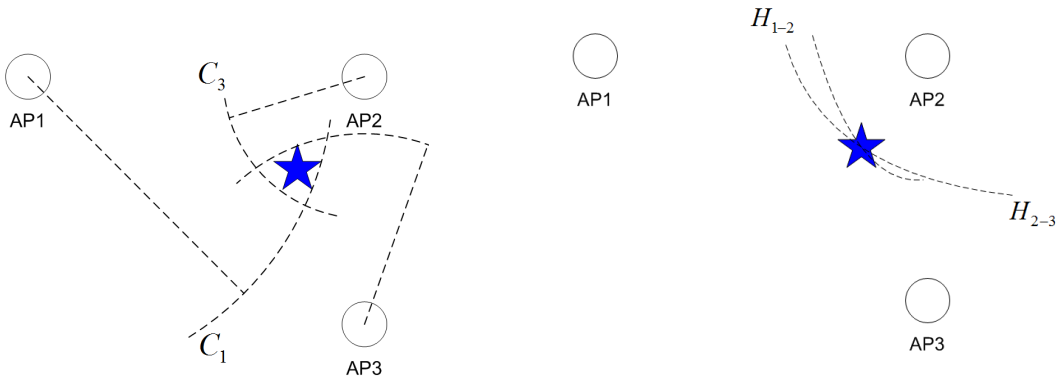

(a) Trilateration with ToA. (b) Trilateration with TDoA.

Fig. 2.2: Trilateration with ToA and TDoA.

2.1.2 ToA and TDoA Based Methods

A practically implemented indoor ToA or TDoA system exploits the distance relationship between the target device and the APs with known locations, as shown in Fig. 2.2. If the target device and the APs have good time synchronization, the ToA information can be utilized to compute distances between the target device and each AP. A circle can be drawn centering each AP with the radius being the corresponding target-AP distance. Ideally, if all distance estimations are accurate and precise, these circles should intersect exactly at one point, which is the location of the target device.

On the other hand, when the APs only have time synchronization with each other but not with the target device, the TDoA measurements can be utilized to compute differences between the distances of the target device to each AP. In this case, a hyperbolic curve can be drawn between any pair of APs. Again, ideally, if all distances estimations are accurate and precise, these hyperbolas should intersect at exactly the same point, which is the location of the target device.

It has been shown that the time (distance) resolution of such ToA and TDoA based trilateration methods are dominated by the system bandwidth [16], [17], [18]. Although Ultra-Wide-Band (UWB) receivers [19] and wideband receivers with enhanced sampling rates [6], or additional hardware [10] can achieve high time resolution, their operating ranges are usually limited in order to reduce interference or conserve power.

Even with very high distance resolution, the ToA measurements obtained in practical situations are still with errors. A simple and effective method in this case will be to search the possible location space in a Gradient Descent manner in order to find the location whose distance relationships to all the APs are closest to the measured distances in a least square sense, as proposed in [20]. Other more advanced methods are also proposed in the literature, such as [21] and [22].

2.1.3 The Non-Line-of-Sight Problem

NLoS conditions are very common in the indoor environments due to the heavy presence of obstacles and barriers. One way to eliminate NLoS conditions is to extensively deploy infrastructure transceivers indoors. However, it is unrealistic in terms of the hardware cost and the wireless interference caused by such a dense deployment.

In the literature, several recent works investigate the problem of localization in the presence of NLoS conditions. [23] assumes a scenario in which both LoS and NLoS conditions co-exist, their proposed algorithm filters out the NLoS signals and only uses the LoS ones for localization. On the other hand, methods that solely utilize NLoS arrival signals themselves for localization [24, 25] require accurate knowledge of bidirectional ToA, DoA, and Direction-of-Departure (DoD). Algorithms for estimating these parameters in heavy multipath environment, such

as MUSIC and ESPRIT, require antenna arrays with a large number of array elements on both transceivers, and signal processing techniques such as sub-array smoothing, which greatly increases the overhead and hardware cost of the system.

2.2 The Fingerprint-based Approach

2.2.1 Algorithms

A typical fingerprint-based system requires a number of reference locations, also known as "training locations", to be selected in the service area. During an off-line training phase, certain location-dependent signal parameters, most commonly RSS, are collected by multiple APs for each training location. The vector of RSS values is then stored as the fingerprint for that particular training location. During the online localization phase, when the RSS vector of the target device is captured, it is used in conjunction with the fingerprints stored in the training database to infer the location of the target device.

One of the earliest fingerprinting methods, the K Nearest Neighbor (KNN) scheme [12], returns the location estimate as the average of the coordinates of the K training locations whose fingerprint vectors have the shortest Euclidean distances to the online RSS vector. A special and primitive case of KNN is the Nearest Neighbor in Signal Space (NNSS) [12], in which $K = 1$. In [26], the K nearest neighbors are weighted by the reciprocal of their signal space Euclidean distance to the online RSS vector to obtain better performance. Both [27] and [28] have taken the probabilistic approach, in which the training data are used to construct PDF for the location and the fingerprint vectors. The conditional expectation of the location is then returned as the estimate. The mathematical expressions of the location estimates are equivalent to the Nadaraya-Watson

Kernel Regression estimator [29]. However, both [27] and [28] assume that the elements of the fingerprint vector are statistically independent from each other for the simplicity of computation, which may not be always true in general.

In [30], fine resolution indoor CIR is collected using a channel sounder and a spectrum analyzer, both operating at a very high bandwidth (200 MHz). A vector of features concerning the power delay characteristics are extracted from the CIR as the location fingerprint. An Artificial Neural Network (ANN) is trained using the training data to infer location when given an online feature vector. Although it has achieved good localization accuracy, this scheme has its own limitations. First, the cost, physical size and weight, and system bandwidth of the devices are unacceptable in an ubiquitous computing context. Second, after the fine resolution measurements are obtained, only a few features are extracted, which is not an efficient utilization of resources devoted to obtain the fine resolution CIR in the first place. Moreover, some features, such as mean excess delay, root mean square of excess delay, and overall gain of channel, are parameters regarding the entire delay spread. In order to acquire such features, a lower bandwidth may be sufficient. However, [30] has not conducted performance study with varying system bandwidth.

2.2.2 Performance Analysis

In practice, error PDF and RoC conditioned on the online RSS vector not only conveniently indicate the reliability of the current location estimate, but also facilitate the fusion of multiple sensors [31]. Due to the presence of multipath propagation, noise, and interference, there can be significant temporal and spatial variations in the online RSS vectors. As illustrated in Fig. 2.3, different samples of online RSS vectors can result in different estimated locations and radii of RoCs,

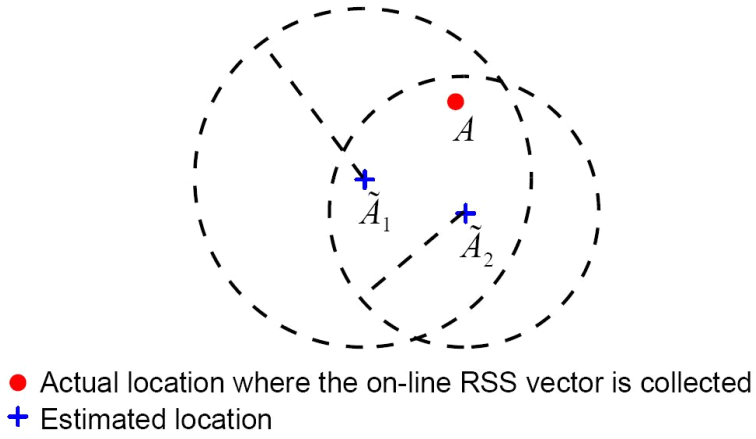

Fig. 2.3: Estimated locations and RoCs based on two different online RSS vectors collected at the same actual location.

even if they are collected at the same actual target location.

Compared to the huge amount of proposals of fingerprint-based localization methods, there are very few works which study the theoretical error analysis of fingerprint-based localization systems, while taking the current online RSS vector into account. The analyses in [32] and [33] are only applicable to the special and primitive case of NNSS, which is not widely applied due to its poor performance. Online error analysis for more advanced and popular schemes such as KNN and probabilistic approach have not been explored theoretically. [34] formulates RoC geometrically in order to filter outliers in localization results. However, the formulation is only validated empirically, without any theoretical justifications.

2.3 The DR based Approach

Early DR tracking scheme estimates location by double integration of acceleration measurements to obtain displacement. It has been shown experimentally in [35] that, double integration of accelerometer measurements introduces fast error accumulation over time.

In order to reduce this cumulative tracking error, the "zero velocity update" (ZUPT) algorithm has been proposed [36]. This algorithm exploits an intrinsic property of pedestrian walking: the bottom of the sole has static contact with the floor which results in both zero acceleration and zero velocity during a certain phase of each step taken. Therefore, any non-zero acceleration or velocity computed from the noisy sensor measurements during this particular phase should be eliminated because they must be the results of the accumulated error. Both [36] and [37] propose to reset the velocity error during the zero-velocity phase of each detected step, while [38] applies ZUPT as pseudo-measurements (observations), fed to an extended Kalman filter (EKF) for tracking error reduction. This algorithm is capable of effectively reducing errors in pedestrian DR systems. However, the extra hardware cost of such a sensor module and the cumbersomeness of wearing such a module on the foot limits this algorithm only to special types of pedestrians, such as battle combatants and emergency responders.

For the case of non-foot-mounted pedestrian DR systems, the step-based DR tracking approach is a preferable choice because it avoids double-integration. In the literature, most of the works which adopt this approach mount DR sensors on fixed parts of the user body with fixed orientation which is convenient for DR. For example, [39] mounts the sensor module on the center back of the pedestrian's waist. [40] mounts the sensor module on a helmet. However, there are also several works which implement DR tracking with arbitrary sensor placement and orientation in practical scenarios. For example, [41] proposes a simple algorithm to find the horizontal plane when the 3-axis accelerometer is oriented arbitrarily. In [42], the principal component analysis (PCA) technique is applied to find the heading orientation, whose effectiveness is also verified experimentally by [43].

2.4 The Hybrid Approach

In the domain of outdoor location tracking, hybrid schemes are proposed in order to reduce the cumulative DR tracking error with the aid of external technologies. Many works in this category use the location coordinates reported by the GPS device as a complete piece of location information for the purpose of tracking error reduction [44–46].

A correction scheme using range information is proposed in [47] for outdoor on-wheel robot tracking. The DR is accomplished with a fine accuracy wheel encoder (with 0.001 m/meter error standard deviation) and a gyroscope, which is not applicable for tracking indoor pedestrian. Tracking errors are frequently corrected using range measurements that arrive at an average rate of 7 times/second. Ranging beacon nodes (BNs) are deployed such that two or more of them can be heard at any point along the robot's path.

For the indoor scenario, a hybrid scheme utilizing WLAN based localization result and map information for DR error correction is proposed in [48]. However, a complete set of location information is used for correction in [48].

Chapter 3

Channel Impulse Response Based Location Fingerprinting

In this chapter, we propose a fingerprint-based localization scheme that exploits the location dependency of the CIR. We approximate the CIR by applying inverse fourier transform (IFT) to the receiver's channel estimation result. The amplitudes of the approximated CIR (ACIR) vector are further transformed into the logarithmic scale in order to ensure that elements in the ACIR vector contribute fairly towards location estimation, which is accomplished through Non-parametric Kernel Regression. As shown in our simulations, when both the number of APs and density of training locations are the same, our proposed scheme exhibits significant advantages in localization accuracy, compared to other fingerprint-based methods found in the literature. Moreover, absolute localization accuracy of the proposed scheme is shown to be robust in the presence of real time environmental changes caused by human bodies with random positions and orientations.

3.1 The Channel Impulse Response Based Fingerprint

Channel impulse response, which completely characterizes the multipath channel and preserves the location dependency [49], is a good choice for location fingerprint to be developed upon. In order to make the localization service more cost-effective and accessible for users of the emerging wideband Orthogonal Frequency Division Multiplexing (OFDM) technologies with different system bandwidths, we propose to approximate the CIR from the receiver's channel estimation result. In OFDM systems, channel estimation can be seen as a vector of N_{sc} complex elements describing the channel in the frequency domain, where N_{sc} is the number of sub-carriers [50]. The time domain CIR can therefore be approximated by taking the IFT of the frequency domain discrete channel estimation vector. Our proposed fingerprint is based on the *amplitudes* of the approximate CIR vector. Fig. 3.1 shows the resemblance between two ACIR vectors collected from two transmitters located 1 m apart from each other in our simulation testbed, at a system bandwidth of 60 MHz (The map of the testbed is shown in Fig. 3.2 with the coordinate axes, dimensions, and the origin indicated).

As shown also in Fig. 3.1, the time range of the ACIR vector is inefficiently large. The bandwidth of the system is 60 MHz in this case, yielding a time resolution of 16.67 ns. In this chapter, we have used $N_{\text{sc}} = 128$ for the IFT. Therefore the overall time range is 2133.7 ns. However, the maximum excess delay of indoor channel, $\tau_{\max}$, is usually smaller than 500 ns, which corresponds to at most the first 30 time samples in this case. Therefore, the remaining 98 samples are irrelevant for localization purpose. When the Signal-to-Noise-Ratio (SNR) is not high enough, the receiver-end Additive White Gaussian Noise (AWGN) at these

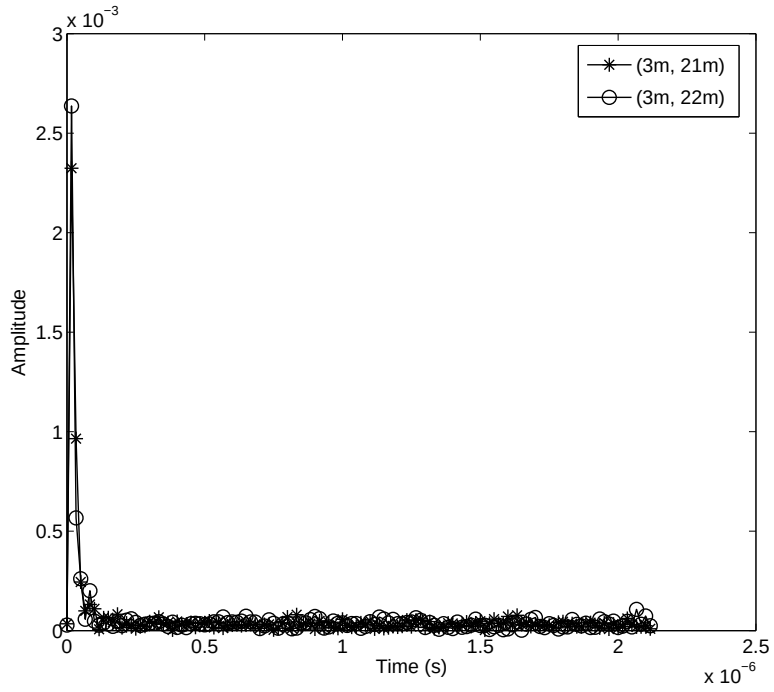

Fig. 3.1: ACIR vectors with transmitters located 1 m apart, at 60 MHz.

time samples will only make the localization accuracy worse. As system bandwidth goes higher, the time resolution becomes better and the number of irrelevant time samples becomes smaller. Therefore, based on the system bandwidth, a reasonable number of relevant time samples should be chosen for the sake of computation efficiency and accuracy. In this chapter, we preserve the first $\lfloor \frac{\tau_{\max}}{1/\mathrm{BW}} \rfloor$ samples in the ACIR vectors for localization purpose, where $\tau_{\max}$ (in seconds) can be determined by experimental measurement or simulation for each specific testbed, and BW is the system bandwidth in Hz.

3.2 System Implementation Issues

Currently, the receiver channel estimation result is not accessible in off-the-shelf wireless adapters or APs. However, hardware and firmware modifications can

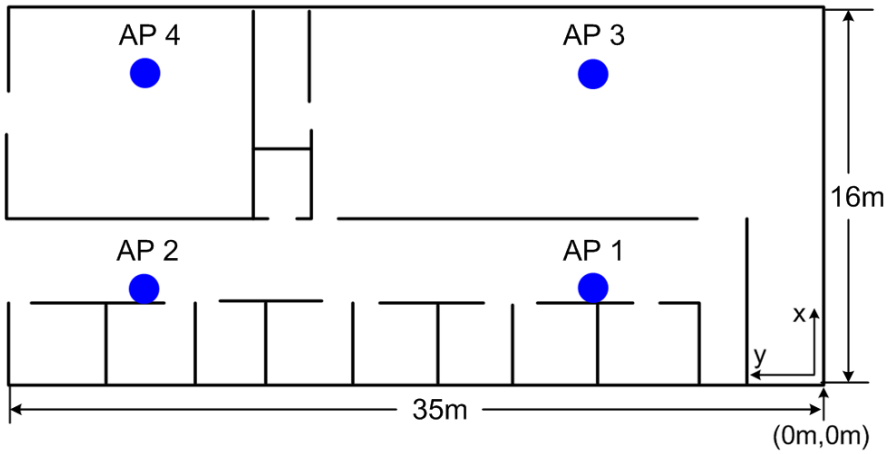

Fig. 3.2: Simulation testbed.

be made in the future to reveal the channel estimation result, which is demanded by more and more localization methods [18],[30]. Alternatively, the raw samples of the received signal at the output of the receiver's Analog-to-Digital Converter (ADC) can be obtained through special hardware interfaces and utilized for CIR approximation. The latter approach is adopted in [10] experimentally. However, [10] has used the debug version of the Intel Pro/Wireless adapter, which is restricted to internal debugging and research purpose only and not commercially available.

3.3 Localization by Nonparametric Kernel Regression

Assume that there are M APs installed in the indoor service area. During the off-line training phase, in order to obtain the i^{th} training fingerprint, $\mathbf{s}_i$, the ACIR vectors obtained from the M APs are first transformed into the logarithmic scale (as discussed later in Section 3.3.2) and then concatenated in a fixed order.

The training location at which $\mathbf{s}_i$ is collected is denoted as $\mathbf{c}_i$. Together, $(\mathbf{s}_i,\ \mathbf{c}_i)$ is referred to as a training record. Note that, different fingerprint vectors collected at the same physical training location are still considered to belong to different training records. Assume there are overall N_{tr} training records, $(\mathbf{s}_i,\ \mathbf{c}_i),\ i = 1,\ 2, ..., N_{\text{tr}}$.

During the online localization operation, the ACIR vectors collected by the M APs are also transformed and concatenated in the same order and denoted as $\mathbf{s}$. Let D denote the dimension of the concatenated ACIR vector. Let the $D \times D$ matrix, $\mathbf{R}_{\mathbf{s}}$, denote the sample covariance matrix, which is computed from the fingerprint vectors, $\mathbf{s}_1, \mathbf{s}_2, ..., \mathbf{s}_{N_{\text{tr}}}$.

The localization task is to find an estimator $\hat{\mathbf{c}}$, for the actual target device location $\mathbf{c}$, based on the observed online signal parameter vector $\mathbf{s}$. Probabilistic localization methods, such as those in [27] and [28], normally use the conditional expectation, $\hat{\mathbf{c}} = E\{\mathbf{c}|\mathbf{s}\}$, as the location estimator, which minimizes the mean square error conditioned on $\mathbf{s}$ [51]. Notice that,

$$\begin{aligned} E\{\mathbf{c}|\mathbf{s}\} &= \int \mathbf{c} f(\mathbf{c}|\mathbf{s})\ d\mathbf{c} \\ &= \frac{\int \mathbf{c} f(\mathbf{c},\mathbf{s})\ d\mathbf{c}}{f(\mathbf{s})} \\ &= \frac{\int \mathbf{c} f(\mathbf{c},\mathbf{s})\ d\mathbf{c}}{\int f(\mathbf{c},\mathbf{s})\ d\mathbf{c}}. \end{aligned} \tag{3.1}$$

Therefore, the computation of $E\{\mathbf{c}|\mathbf{s}\}$ requires exact knowledge of the joint PDF, $f(\mathbf{c},\mathbf{s})$, which is usually not available in practice. However, recall that from the training phase, we have obtained N_{tr} pairs of training records, $(\mathbf{s}_i, \mathbf{c}_i), i = 1, 2, ..., N_{\text{tr}}$. When the online user signal parameter vector $\mathbf{s}$ is collected, $E\{\mathbf{c}|\mathbf{s}\}$

can be approximated by the Nadaraya Watson Kernel Regression estimator [29],

$$E\{\mathbf{c}|\mathbf{s}\} \approx \frac{\sum_{i=1}^{N_{\text{tr}}} \mathbf{c}_i K_{\mathbf{H}_s}(\mathbf{s}-\mathbf{s}_i)}{\sum_{i=1}^{N_{\text{tr}}} K_{\mathbf{H}_s}(\mathbf{s}-\mathbf{s}_i)}, \tag{3.2}$$

where,

$$K_{\mathbf{H}_s}(\mathbf{s}-\mathbf{s}_i) = \frac{1}{|\mathbf{H}_s|} K[\mathbf{H}_s^{-1} \cdot (\mathbf{s}-\mathbf{s}_i)]. \tag{3.3}$$

In the above equation, the term $|\mathbf{H}_s|$ is the determinant of the matrix $\mathbf{H}_s$. The function $K(\mathbf{y}-\mathbf{z})$ is known as the kernel function. Generally, it is chosen in such a way that its value is larger when $\mathbf{y}-\mathbf{z}$ has smaller magnitude in all dimensions. In other words, the more similar $\mathbf{y}$ and $\mathbf{z}$ are, the larger the resulting kernel function's value is. Intuitively, the Nadaraya-Watson Kernel Regression estimator is the normalized weighted average of all the training locations' coordinates. A training location with a fingerprint vector more/less similar to the online ACIR vector receives a higher/lower weight, accordingly.

In this chapter, we adopt the popular Gaussian kernel function,

$$K(\mathbf{y}-\mathbf{z}) = \frac{1}{(2\pi)^{D/2}} \exp\left[-\frac{1}{2}\,(\mathbf{y}-\mathbf{z})^T \cdot (\mathbf{y}-\mathbf{z})\right]. \tag{3.4}$$

The $D \times D$ matrix $\mathbf{H}_s$ in (4.3) is called the "bandwidth matrix". It controls the shape and orientation of the kernel function. Note that the term "bandwidth" here refers to the spread of the kernel. It should not be confused with the system bandwidth in the RF spectrum. The choice of the bandwidth matrix is critical to the accuracy of the kernel density estimator. For simplicity of computation, both [27] and [28] have chosen a diagonal bandwidth matrix so that only D kernel bandwidth parameters need to be selected. This is implicitly assuming that the elements in the fingerprint vector are always independent from each other. In this

chapter, we drop this assumption of independence between the fingerprint vector elements. Instead, we use the multivariate generalization of the Scott's Rule of Thumb for bandwidth selection [52],

$$\mathbf{H}_s = N_{\text{tr}}^{-1/(D+4)} \mathbf{R_s}^{1/2}, \tag{3.5}$$

in which N_{tr} is the size of training data set, D is the dimension of the concatenated fingerprint vector, and $\mathbf{R_s}$ is the sample covariance matrix computed from the training samples. This formula of bandwidth matrix computation takes into consideration the general statistical inter-dependence between the fingerprint vector elements by first transforming them using their sample covariance matrix.

Note that, detailed description and derivation of NKR techniques and bandwidth matrix selection is beyond the scope of this thesis. Interested readers are referred to [29], [52], and [53] for more detailed information.

3.3.1 Low-Pass Smoothing

We apply a simple low-pass smoothing technique in order to smooth out the individual variations among fingerprint vectors collected within close proximity while preserving their common location dependency. For each training record $(\mathbf{s}_i, \mathbf{c}_i)$, the smoothed fingerprint vector is obtained by taking the average of training ACIR vectors in the set, $\{\mathbf{s}_k | \ \|\mathbf{c}_k - \mathbf{c}_i\| \leq r_0\}$, where the constant r_0 determines the size of the smoothing window. We have found experimentally that a good choice for the 2-D window size, r_0, is to make it equal to the training grid spacing.

3.3.2 Logarithmic Scale Transformation

In order to understand the necessity and effect of transforming the decimal scale ACIR vector into the logarithmic scale, consider an online ACIR vector in decimal scale, $\mathbf{h} = [h_1, h_2, ...h_{N_{\text{sc}}}]^T$, which is the discrete time domain description of the multipath channel's amplitude gain at delay time instances, nT_s, $n = 1, 2, ..., N_{\text{sc}}$, where T_s is the symbol duration. For any n, the amplitude gain h_n can be expressed as the product of two terms, which will be described below.

The first term is the amplitude gain which is purely caused by the propagation path loss and the antenna characteristics. Assume that a signal $z(t)$ is transmitted at time instant 0. The multipath version of the transmitted signal received at time instant nT_s will be, $a(nT_s) \cdot z(t - nT_s)$, where $a(nT_s)$ is the gain purely caused by propagation path loss. If the transmitted power at the transmitter end is P_0, we have,

$$P_0 = \frac{1}{T} \int_0^T |z(t)|^2 dt, \tag{3.6}$$

where T is the time over which the power is measured. If we only consider the effect of propagation path loss and antenna characteristics, the power of the signal received at time instant nT_s at the receiver end will be,

$$\begin{aligned} P_n &= \frac{1}{T} \int_{nT_s}^{nT_s+T} |a(nT_s) \cdot z(t - nT_s)|^2 dt \\ &= |a(nT_s)|^2 \cdot \frac{1}{T} \int_{nT_s}^{nT_s+T} |z(t - nT_s)|^2 dt \\ &= |a(nT_s)|^2 \cdot P_0 \end{aligned} \tag{3.7}$$

On the other hand, the overall distance travelled by the signal received at nT_s seconds after transmission is,

$$d = v_{\text{RF}} \cdot nT_s, \tag{3.8}$$

where v_{RF} is the propagation speed of the RF signal in the medium. Here, we assume that the differences in propagation speeds among different media are negligible. Since we are only considering the pure effects of propagation path loss and antenna characteristics here, by Friis transmission formula [54], we have,

$$P_n = G_{\mathrm{tx}} G_{\mathrm{rx}} (\frac{\lambda}{4\pi d})^2 P_0, \tag{3.9}$$

where G_{tx} and G_{rx} are the gains of transmitter and receiver antennas respectively, and λ is the carrier wavelength. Using (3.7) and (3.9), the amplitude gain at delay instant nT_s purely caused by propagation path loss and antenna characteristics is therefore,

$$|a(nT_s)| = \frac{\sqrt{G_{\mathrm{tx}} G_{\mathrm{rx}}}\lambda}{4\pi v_{\mathrm{RF}}} \cdot \frac{1}{nT_s}. \tag{3.10}$$

The second term is the amplitude gain caused by the penetrations, reflections, and diffractions experienced by the signal travelling through the indoor environment. The location dependency is mainly caused by this term. We model the aggregated result of these phenomena by $\alpha(nT_s)$ for the multipath version of the signal received at nT_s. Note that if there is no multipath signal received at nT_s, $\alpha(nT_s) = 0$. Therefore, the overall amplitude gain caused by the indoor channel on a signal that is received at time nT_s is,

$$h_n = \alpha(nT_s) \cdot \frac{\sqrt{G_{\mathrm{tx}} G_{\mathrm{rx}}}\lambda}{4\pi v_{\mathrm{RF}}} \cdot \frac{1}{nT_s}, \tag{3.11}$$

for $n = 1, 2, ..., N_{\mathrm{sc}}$ in the online ACIR vector $\mathbf{h}$.

The location estimation in (3.2) involves computing kernel functions using the online ACIR vector and every fingerprint ACIR vector. Consider any fingerprint ACIR vector, $\mathbf{g} = [g_1, g_2, ...g_{N_{\mathrm{sc}}}]^T$, whose n^{th} element can be similarly expressed

as,

$$g_n = \beta(nT_s) \cdot \frac{\sqrt{G_{\text{tx}}G_{\text{rx}}}\lambda}{4\pi v_{\text{RF}}} \cdot \frac{1}{nT_s}, \tag{3.12}$$

where $\beta(nT_s)$ accounts for the aggregated amplitude gain other than propagation path loss or antenna characteristics, introduced by the indoor channel on the multipath version of the signal received at nT_s. When computing $\mathbf{h} - \mathbf{g}$ for the kernel function, the difference at the n^{th} vector element is,

$$\begin{aligned} h_n - g_n &= \alpha(nT_s) \cdot \frac{\sqrt{G_{\text{tx}}G_{\text{rx}}}\lambda}{4\pi v_{\text{RF}}} \cdot \frac{1}{nT_s} - \beta(nT_s) \cdot \frac{\sqrt{G_{\text{tx}}G_{\text{rx}}}\lambda}{4\pi v_{\text{RF}}} \cdot \frac{1}{nT_s} \\ &= [\alpha(nT_s) - \beta(nT_s)] \cdot \frac{\sqrt{G_{\text{tx}}G_{\text{rx}}}\lambda}{4\pi v_{\text{RF}}} \cdot \frac{1}{nT_s}. \end{aligned} \tag{3.13}$$

For a given SNR and bandwidth condition, as long as the ACIR vector length is still within the relevant range, the values of $\alpha(nT_s)$ and $\beta(nT_s)$ for all n should be treated with equal importance, as far as location estimation is concerned. However, as seen in (3.13), simply taking the difference between the corresponding vector elements in the decimal scale ACIR vectors leaves the time index term n in the denominator. This means that the contribution from the channel amplitude gains with larger delays, corresponding to those elements with larger indices in the ACIR vector, is unnecessarily reduced due to a larger n.

On the other hand, if we transform the elements of the two ACIR vectors to the logarithmic scale, we have,

$$\begin{aligned} \log h_n - \log g_n = &[\log \alpha(nT_s) + \log (\tfrac{\sqrt{G_{\text{tx}}G_{\text{rx}}}\lambda}{4\pi v_{\text{RF}}} \cdot \tfrac{1}{nT_s})] \\ &-[\log \beta(nT_s) + \log (\tfrac{\sqrt{G_{\text{tx}}G_{\text{rx}}}\lambda}{4\pi v_{\text{RF}}} \cdot \tfrac{1}{nT_s})] \\ &= \log \alpha(nT_s) - \log \beta(nT_s). \end{aligned} \tag{3.14}$$

As can be seen in (3.14), the difference between $\log h_n$ and $\log g_n$ is not scaled by

the time index term n anymore. In other words, all the elements in the ACIR vector within the relevant time range contribute fairly to the kernel computation and the location estimation.

It should be noted that, the cancellation of the time index term can also be achieved by directly dividing h_n by g_n. The two methods are equivalent in this sense. However, in order to be consistent with the kernel function computation in which a substraction between two vectors is involved, we take the logarithmic transformation approach in this chapter.

3.4 Simulations and Discussions

Since the channel estimation results are currently not accessible in off-the-shelf wireless adapters and APs, the localization performance of the proposed method is evaluated through simulations as a first step. We have chosen a 3-D ray-tracing based simulator, the Radiowave Propagation Simulator (RPS) [55], in order to closely emulate the realistic indoor RF propagations. RPS is able to generate fine-resolution CIR, taking into consideration the effects of the path loss, penetrations, reflections, and diffractions experienced by an RF signal, after the environment model, transmitter-receiver locations, antenna characteristics, and carrier frequency are specified by the user. The accuracy of RPS simulator has been verified via comparison with real indoor experimental measurements in [56].

The CIR generated by RPS are used as the practical channel models. Transceiver operations, such as sampling, channel estimation, and AWGN, are simulated using MATLAB programmes.

We have constructed the 3-D model for one part of our campus. It is 16 m$\times$35 m in dimension, including two laboratory rooms on one side, eight staff offices on

Table 3.1: Material characteristics for the testbed

Object	$\epsilon_{\mathbf{Re}}$	$\epsilon_{\mathbf{Im}}$	**Thickness (m)**
Floor and Ceiling	4	-0.2	0.5
Wall	4	-0.4	0.15
Human Body	11	-2.04	0.25

the other, and a corridor between them. As shown in Fig. 3.2, this indoor simulation testbed is a mixture of both LoS and NLoS propagation conditions. The material characteristics of the testbed elements affecting the RF propagation are summarized in Table 3.1, in which ϵ_{Re} and ϵ_{Im} are the real and imaginary parts of the relative permittivity of the material respectively. As also shown in Fig. 3.2, the two shaded circles at the bottom correspond to the locations of the actual Wi-Fi APs deployed in the building for campus wireless communication coverage, while the two on the top are added to the testbed to study the effects of varying the number of APs on the localization accuracy, in our simulation. The APs and the user mobile device are placed 2 m and 1.2 m above the ground, respectively. We assume that all the transmitters and receivers are equipped with omni-directional antennas. The carrier frequency is set to 5 GHz, which conforms to the IEEE 802.11a standard. The transmission power is set to 20 dBm, which is a common power setting for indoor Wi-Fi APs.

Training grid spacing of 1 m [30] or 2 m [27],[28] are commonly chosen for indoor fingerprint-based systems. In our simulations, we use 1.5 m training grid spacing to evaluate the localization accuracy of the proposed system under varying factors such as system bandwidth, number of APs, and number of people in the testbed which create random environmental changes. We also study the effect of changing the training density itself by setting the training grid spacing from

1 m to 2.5 m, with a 0.5 m step size. There are 173 testing locations picked in the testbed. Twenty testing samples, each injected with pseudo-random noise, are taken at each testing location, resulting in 3460 testing samples overall for the entire testbed in each set of simulations. Note that, in order to compare the performance of the schemes under the variations of different factors, the average localization error of these 3460 testing samples are used as the performance metric. Whenever applicable, the 95% confidence interval [57] for each data point is also shown in the figures to indicate the reliability of the results.

3.4.1 Performance with Varying System Bandwidth

The localization accuracy of the proposed logarithmic-scale ACIR fingerprint with Nonparametric Kernel Regression (LOG-ACIR-NKR) is first compared with three other methods, namely, RSS fingerprint with Kernel distance method (RSS-Kernel), as described in [28], decimal-scale ACIR fingerprint with Nonparametric Kernel Regression (ACIR-NKR), and decimal-scale ACIR fingerprint with General Regression Neural Networks (ACIR-GRNN), generalized from [30], with system bandwidth increasing from 20 MHz to 200 MHz, at a step size of 20 MHz, when two APs, 1.5 m training grid spacing are used. In order to implement the ACIR-GRNN scheme, five features are extracted from the ACIR vector, namely, the mean excess delay, the root mean square (rms) of the excess delay, the overall power gain of the channel, as well as the power gain and delay of the first arrival path. A GRNN [58] is used to map features to location coordinates.

As shown in Fig. 3.3, the proposed LOG-ACIR-NKR scheme has achieved much higher localization accuracy compared to the RSS-Kernel scheme and the ACIR-GRNN scheme for all the system bandwidths tested. The higher dimensionality of the LOG-ACIR fingerprint preserves more location dependency compared

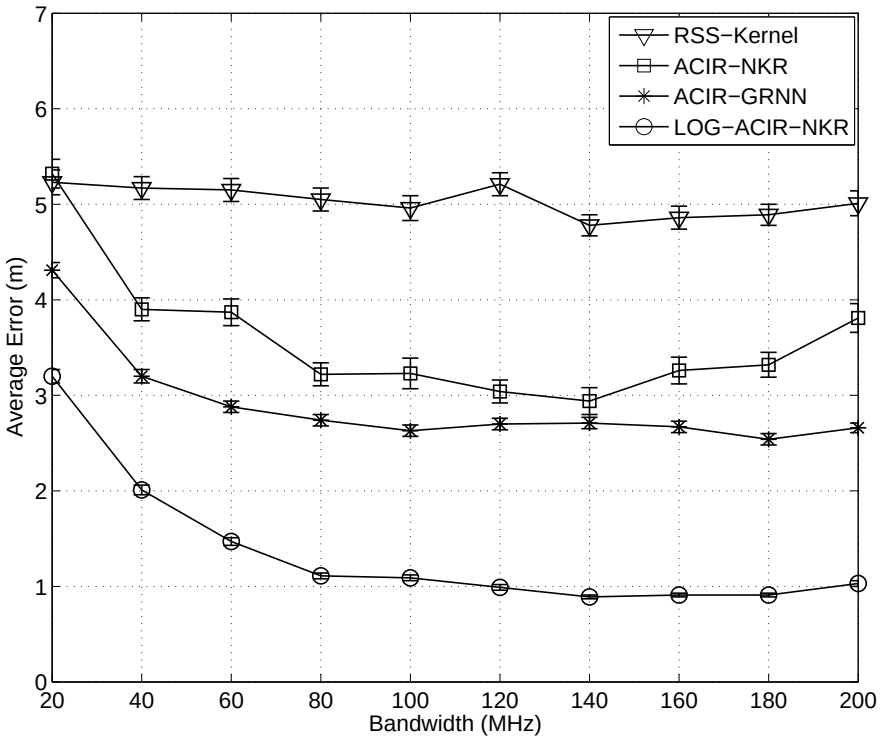

Fig. 3.3: Localization accuracy vs. system bandwidth (using only AP 1 and AP 2).

to both RSS and features extracted from the decimal scale ACIR. It is also important to note that, the logarithmic transformation is critical to the superior performance advantage, as can be shown by the huge difference in performance between LOG-ACIR-NKR scheme and the ACIR-NKR scheme. As explained earlier, this is because the elements in the logarithmic scale ACIR vector now have fair contributions to the location estimation.

3.4.2 Cumulative Error Distribution

Fig. 3.4 shows the cumulative error distribution functions of RSS-Kernel, ACIR-GRNN, and the proposed LOG-ACIR-NKR, when two APs, a training grid spacing of 1.5 m, and a system bandwidth of 60 MHz are used. As can be seen, the proposed scheme achieves a localization error of under 2.05 m for 80% of the

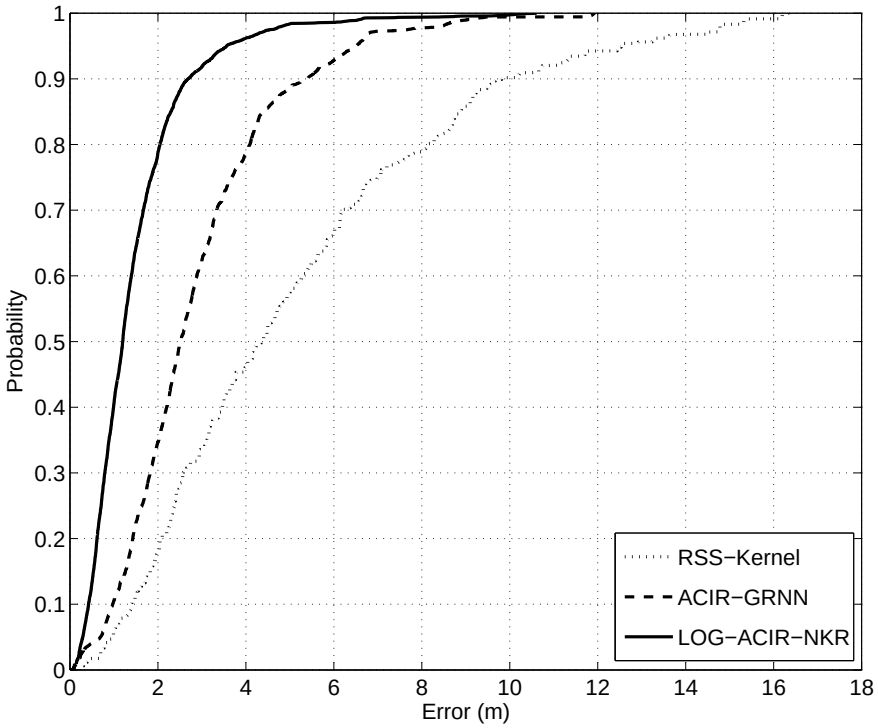

Fig. 3.4: Cumulative error probability (using only AP 1 and AP 2).

testing samples, which is significantly smaller than those of ACIR-GRNN (4.09 m) and RSS-Kernel (8.15 m) with the same probability.

3.4.3 Effect of Varying Training Location Density

The effect of varying training location density can be examined by choosing different subsets of the training locations with different training grid spacing. The localization error of RSS-Kernel, ACIR-GRNN, and LOG-ACIR-NKR at 60 MHz with two APs are shown in Fig. 3.5. When training grid spacing increases from 1 m to 2.5 m, with a step size of 0.5 m, the performance of all the three methods becomes worse. However, it should be noted that, the error of the proposed LOG-ACIR-NKR scheme with 2.5 m training grid spacing, which corresponds to 78 training locations, is smaller than that of ACIR-GRNN scheme with 1 m training

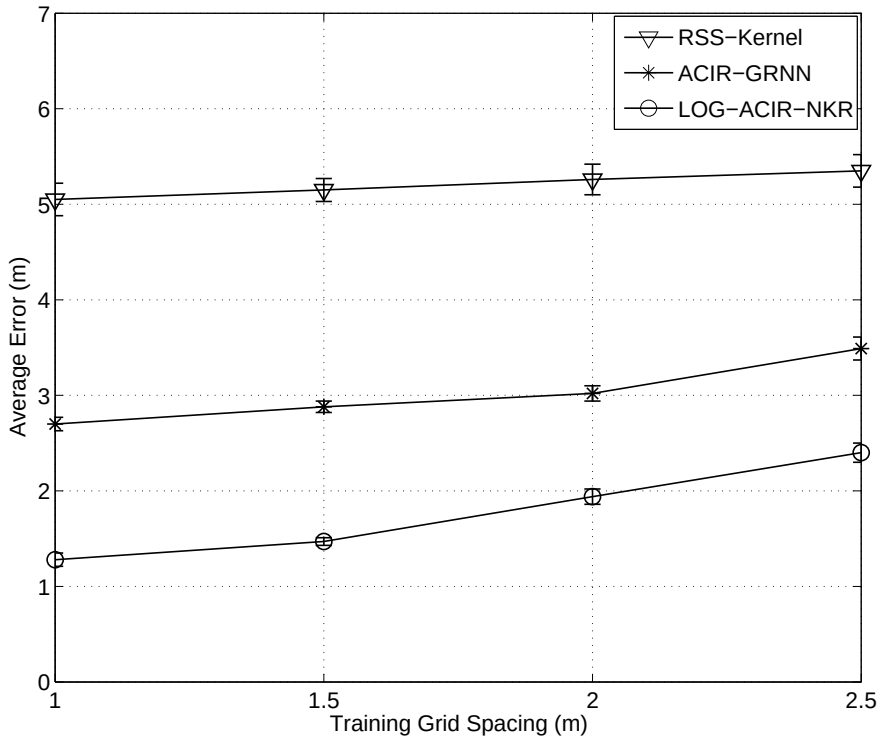

Fig. 3.5: Localization accuracy vs. training density (using only AP 1 and AP 2).

grid spacing, which corresponds to 544 training locations. This means that the proposed LOG-ACIR-NKR scheme is much more efficient in utilizing the available training data and training efforts.

3.4.4 Effect of Varying the Number of Access Points

Next, we keep the training grid spacing at 1.5 m, system bandwidth at 60 MHz, and vary the number of APs. As shown in Fig. 3.6, all the three algorithms benefit from an increase in the number of APs. When there are four APs, the average localization error for RSS-Kernel is 3.23 m, which is comparable with the experimental results presented in the literature for RSS fingerprint-based localization, under similar settings. It should be emphasized that, even with only two APs, the localization error of the proposed LOG-ACIR-NKR scheme is still

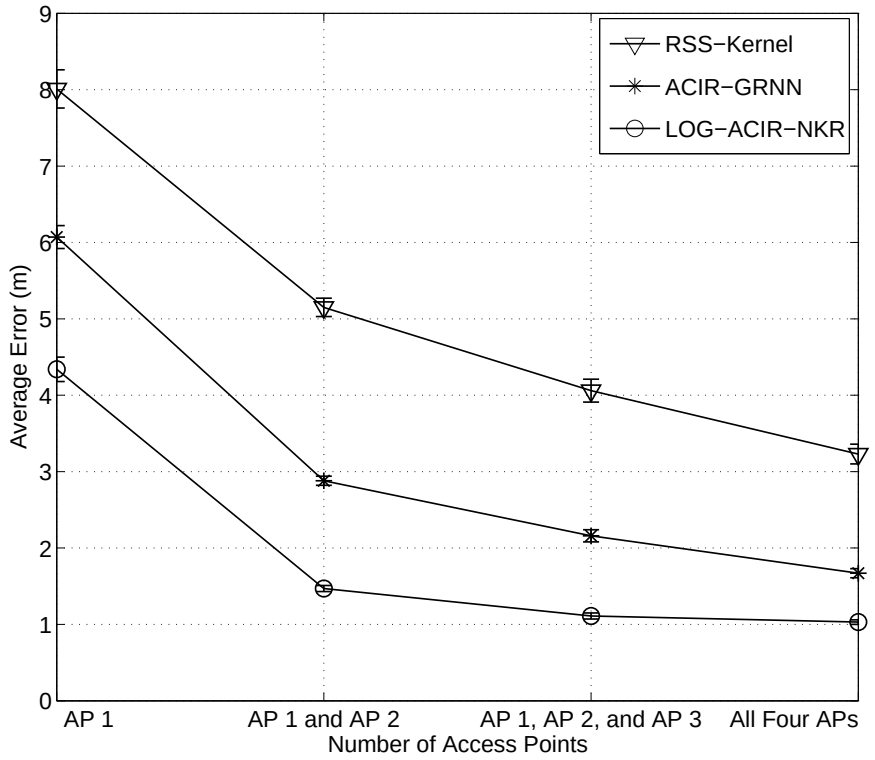

Fig. 3.6: Localization accuracy vs. number of APs.

better than that of the ACIR-GRNN scheme with 4 APs. This result implies that, when we have to construct a localization system in an area where there can only be limited number of APs, the proposed scheme is a preferred choice which utilizes the available hardware efficiently.

3.4.5 Effect of Real Time Variation in Environment

One major cause of real time changes in the indoor environment is the crowd of people with random positions and body orientations. This is because the human body contains a large amount of water, which is an excellent absorber of RF radiation. In this section, we model the human body by a 0.5 m×0.25 m×1.8 m cuboid with the same relative permittivity as pure water. As shown in Fig. 3.7,

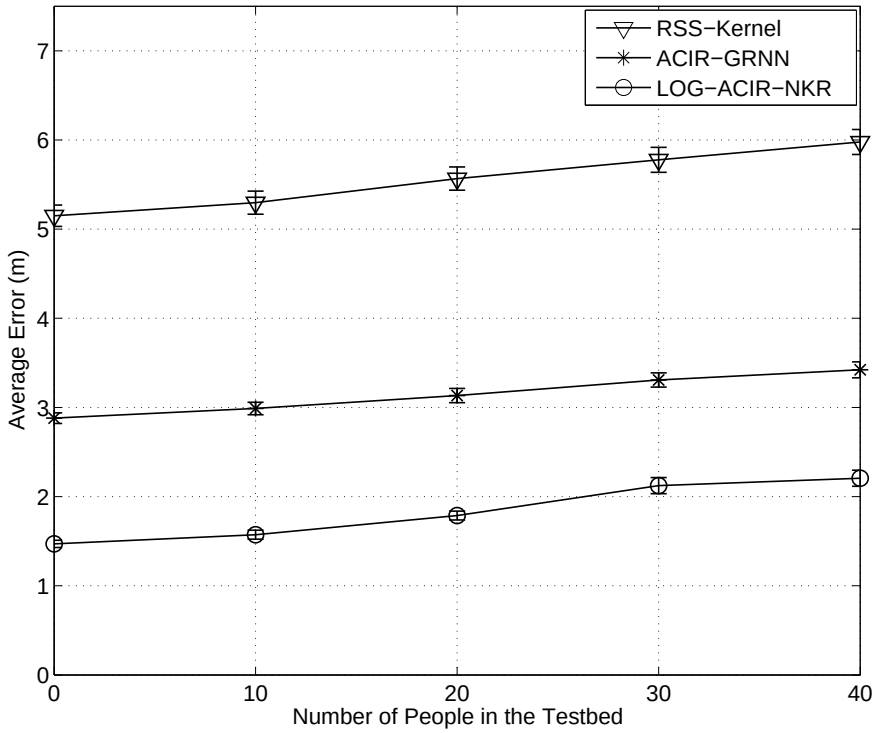

Fig. 3.7: Localization accuracy vs. number of people randomly placed and oriented in the testbed (using only AP 1 and AP 2).

based on the training data collected when no one is in the testbed, the localization accuracy of RSS-Kernel, ACIR-GRNN, and LOG-ACIR-NKR schemes are tested in cases where different number of people are randomly positioned and oriented in the testbed, which operates with 60 MHz bandwidth, two APs, and 1.5 m training grid spacing. For each data point, the average location errors are computed and plotted for 10 random snapshots. In each snapshot, the same number of people are randomly placed and oriented in the testbed. As can be seen in Fig. 3.7, the performance of all three methods become worse when there are more people in the environment. However, the LOG-ACIR-NKR scheme maintains its superior advantage in absolute localization accuracy among the three methods. Even in the random presence of 40 people, it is still able to outperform the ACIR-GRNN scheme with no one in the testbed. Note that, for each data point, the worst-case

95% confidence interval among the 10 snapshots is shown.

3.4.6 Computation Time

The low-pass smoothing and logarithmic transformation of the fingerprint vectors can be pre-computed off-line, after training is completed. During the on-line location estimation, as can be seen from (3.2), most of the time is spent on computing the kernel function values for the N_{tr} training sample vectors. For each Gaussian kernel computation, the most time-consuming operation is the matrix multiplication in the exponent. Therefore, if the fingerprint vector's dimension is D, the localization scheme has a complexity $O(D^2)$. For our simulation, we have carried out the localization computation in MATLAB, running on a desktop PC with Intel Core 2, 2.83 GHz Quad CPU, and 3 GB RAM. The average time (over 3460 samples) spent in locating one testing sample is 3.33 ms for the proposed fingerprint, when two APs, a training grid spacing of 1.5 m, and a system bandwidth of 60 MHz are used. The absolute overhead incurred in locating a single user can be very small if a powerful, dedicated localization server is used to implement the proposed scheme.

Chapter 4

Error Analysis for Fingerprint-based Localization

In this chapter, we derive the theoretical expression of the error PDF and RoC conditioned on the online signal parameter vector, for a generalized fingerprint-based localization system. As the computation of these terms require the exact expression of the joint PDF for both the target device location and the online signal parameter vector, which is often not available practically, we propose to approximate this joint PDF by Nonparametric Kernel Density Estimation (NKDE) techniques using the existing training fingerprints, without any extra calibration efforts.

4.1 Nonparametric Kernel Density Estimation

Before proceeding to derive the error PDF and RoC, we first briefly describe the relevant NKDE technique in this section, in the context of an indoor RSS-

based fingerprinting localization system. Note that, our proposed scheme in this chapter is applicable to generalized fingerprint-based systems. However, for the convenience of discussion and experimental evaluation with accessible hardware, we take the example of a RSS-based fingerprinting system in our derivation.

Assume that, for a RSS-based fingerprinting system, we have collected N_{tr} data samples as the training records, $(\mathbf{s}_i, \mathbf{c}_i)$, $i = 1, 2, ..., N_{\text{tr}}$, in which $\mathbf{s}_i = [s_{i,1}, s_{i,2}, ..., s_{i,M}]^T$ is the M-dimensional fingerprint vector of the i^{th} training fingerprint, and $\mathbf{c}_i = [x_i, y_i]^T$ is the 2-dimensional coordinates of the training location at which the i^{th} fingerprint is collected. Note that, different RSS vectors taken at the same training location are treated as different training fingerprints in this chapter. Also, let the vectors, $\mathbf{s} = [s_1, s_2, ..., s_M]^T$ and $\mathbf{c} = [x, y]^T$, denote the online RSS vector and the actual target device location coordinates, respectively. For the convenience of discussions, let,

$$\mathbf{u} = [x, y, s_1, s_2, ..., s_M]^T, \tag{4.1}$$

and

$$\mathbf{u}_i = [x_i, y_i, s_{i,1}, s_{i,2}, ..., s_{i,M}]^T. \tag{4.2}$$

The dimension of both vectors $\mathbf{u}$ and $\mathbf{u}_i$ is therefore $D = M + 2$.

In order to approximate the joint PDF of $\mathbf{c}$ and $\mathbf{s}$, $f_{\mathbf{c},\mathbf{s}}(\mathbf{u})$, which is now the multivariate PDF of $\mathbf{u}$, a kernel function,

$$K_{\mathbf{H}_i}(\mathbf{u} - \mathbf{u}_i) = \frac{1}{|\mathbf{H}_i|} K(\mathbf{H}_i^{-1} \cdot (\mathbf{u} - \mathbf{u}_i)), \tag{4.3}$$

can be placed at each training sample $\mathbf{u}_i$. In (4.3), $|\mathbf{H}_i|$ denotes the determinant of the matrix $\mathbf{H}_i$. The choice of $K(\mathbf{z})$ determines the functional form of the kernel.

The "bandwidth matrix", $\mathbf{H}_i$, controls the spread and orientation of the kernel function.

Therefore, the multivariate density estimation of $f_{\mathbf{c},\mathbf{s}}(\mathbf{u})$ is,

$$\hat{f}_{\mathbf{c},\mathbf{s}}(\mathbf{u}) = \frac{1}{N_{\text{tr}}} \sum_{i=1}^{N_{\text{tr}}} K_{\mathbf{H}_i}(\mathbf{u} - \mathbf{u}_i). \tag{4.4}$$

In this chapter, we still adopt the popular Gaussian kernel,

$$K(\mathbf{z}) = \frac{1}{(2\pi)^{D/2}} \exp\left(-\frac{1}{2}\mathbf{z}^T \cdot \mathbf{z}\right). \tag{4.5}$$

The choice of the bandwidth matrix, $\mathbf{H}_i$, is critical to the density estimation. In this chapter, we have adopted the local adaptive bandwidth selection method which is introduced in [53]. In the following paragraphs, we briefly describe this technique for the sake of better understanding.

First, we compute a fixed "pilot bandwidth matrix",

$$\mathbf{H}' = \omega \cdot \mathbf{R}^{1/2}. \tag{4.6}$$

In equation (4.6), the scalar,

$$\omega = \left(\frac{4}{2D+1}\right)^{1/(D+4)} \cdot (N_{\text{tr}})^{-1/(D+4)}, \tag{4.7}$$

is the theoretically optimal plug-in bandwidth for each dimension, when the distribution of the underlying D-dimensional vector elements are independent and Gaussian distributed [53]. The matrix, $\mathbf{R}$, is the sample covariance matrix computed from the vectors, $\mathbf{u}_i, i = 1, 2, ..., N_{\text{tr}}$. It is used to reduce the inter-dependence between elements in the vector $\mathbf{u}$. Using $\mathbf{H}'$ and (4.4), a "pilot density" value,

$\hat{f}'(\mathbf{u}_i)$, for each training data point $\mathbf{u}_i$ can be computed. Let

$$\bar{f}' = \sqrt[N_{\text{tr}}]{\prod_{i=1}^{N_{\text{tr}}} \hat{f}'(\mathbf{u}_i)}, \tag{4.8}$$

be the geometric mean of the pilot density values. The local adaptive bandwidth for the training data sample, $\mathbf{u}_i$, is then [53],

$$\mathbf{H}_i = (\frac{\hat{f}'(\mathbf{u}_i)}{\bar{f}'})^{-1/2} \cdot \mathbf{H}'. \tag{4.9}$$

Intuitively, the fixed bandwidth matrix, $\mathbf{H}'$, in the pilot density computation underestimates the difference between large and small density values. Such a formulation of the local adaptive bandwidth matrix, $\mathbf{H}_i$, re-adjusts the local density value based on its comparison with the geometric average in order to obtain better density estimation.

Similar to (4.4), $f_{\mathbf{s}}(\mathbf{s})$ can be estimated as,

$$\hat{f}_{\mathbf{s}}(\mathbf{s}) = \frac{1}{N_{\text{tr}}} \sum_{i=1}^{N_{\text{tr}}} K_{\mathbf{H}_i^s}(\mathbf{s} - \mathbf{s}_i). \tag{4.10}$$

Obtaining $\mathbf{H}_i^s$ is relatively easy given that $\mathbf{H}_i$ has already been computed. This is because, theoretically,

$$\begin{aligned} \hat{f}_{\mathbf{s}}(\mathbf{s}) &= \int \hat{f}_{\mathbf{c},\mathbf{s}}(\mathbf{u})\ d\mathbf{c} \\ &= \frac{1}{N_{\text{tr}}} \sum_{i=1}^{N_{\text{tr}}} \int K_{\mathbf{H}_i}(\mathbf{u} - \mathbf{u}_i)\ d\mathbf{c}, \end{aligned} \tag{4.11}$$

where each $K_{\mathbf{H}_i}(\mathbf{u}-\mathbf{u}_i)$ is equivalently a multivariate Gaussian PDF characterized by mean vector $\mathbf{u}_i$ and covariance matrix $\mathbf{H}_i\mathbf{H}_i^T$. Therefore, each integration in

(4.11) results in a marginal Gaussian PDF characterized by mean vector $\mathbf{s}_i$, and the $M \times M$ covariance matrix $\mathbf{\Phi}_i^{\mathbf{ss}}$, which is a sub-matrix of $\mathbf{H}_i\mathbf{H}_i^T$ corresponding to the auto-covariance of $\mathbf{s}$, i.e.,

$$\mathbf{H}_i\mathbf{H}_i^T = \begin{bmatrix} \mathbf{\Phi}_i^{\mathbf{cc}} & \mathbf{\Phi}_i^{\mathbf{cs}} \\ \mathbf{\Phi}_i^{\mathbf{sc}} & \mathbf{\Phi}_i^{\mathbf{ss}} \end{bmatrix}. \tag{4.12}$$

Therefore, $\mathbf{H}_i^s = [\mathbf{\Phi}_i^{\mathbf{ss}}]^{1/2}$.

4.2 Theoretical Error Performance Analysis

Recall that $\mathbf{c} = [x, y]^T$ is the actual online target device location, which is unknown. Let $\hat{\mathbf{c}} = [\hat{x}, \hat{y}]^T$ be the location estimate provided by any one of the existing fingerprint-based algorithms. The error vector from the location estimate to the actual target device location is defined as,

$$\mathbf{e} \;=\; [x - \hat{x},\ y - \hat{y}]^T. \tag{4.13}$$

Let η and γ be the length and angle of the error vector $\mathbf{e}$, respectively. We have,

$$[\eta\cos\gamma,\ \eta\sin\gamma]^T = [x - \hat{x},\ y - \hat{y}]^T. \tag{4.14}$$

Hence,

$$[x,\ y]^T = [\hat{x} + \eta\cos\gamma,\ \hat{y} + \eta\sin\gamma]^T. \tag{4.15}$$

The Jacobian matrix $\mathbf{J}$ is,

$$\mathbf{J} = \begin{bmatrix} \frac{\partial x}{\partial \eta} & \frac{\partial x}{\partial \gamma} \\ \frac{\partial y}{\partial \eta} & \frac{\partial y}{\partial \gamma} \end{bmatrix} = \begin{bmatrix} \cos\gamma & -\eta\sin\gamma \\ \sin\gamma & \eta\cos\gamma \end{bmatrix}. \tag{4.16}$$

Therefore, the determinant of $\mathbf{J}$ is simply the error distance, η.

If $f_{\mathbf{c},\mathbf{s}}(\mathbf{c},\mathbf{s})$ is the joint PDF of the online RSS vector $\mathbf{s}$ and the actual target device location $\mathbf{c}$, we can perform the transformation of variables from $[x,\ y]^T$ to $[\eta,\ \gamma]^T$, as follows:

$$f_{[\eta,\ \gamma]^T,\mathbf{s}}([\eta,\ \gamma]^T,\mathbf{s}) = f_{\mathbf{c},\mathbf{s}}([\hat{x}+\eta\cos\gamma,\ \hat{y}+\eta\sin\gamma]^T,\mathbf{s})\cdot\eta. \tag{4.17}$$

Integrating over γ, we have,

$$f_{\eta,\mathbf{s}}(\eta,\mathbf{s}) = \int_0^{2\pi} f_{[\eta,\ \gamma]^T,\mathbf{s}}([\eta,\ \gamma]^T,\mathbf{s})\ d\gamma. \tag{4.18}$$

Once the joint PDF of η and $\mathbf{s}$ is obtained, the PDF of the localization error distance η conditioned on the online RSS vector $\mathbf{s}$ is simply,

$$\begin{aligned} f_{\eta|\mathbf{s}}(\eta|\mathbf{s}) &= \frac{f_{\eta,\mathbf{s}}(\eta,\mathbf{s})}{f_{\mathbf{s}}(\mathbf{s})} \\ &= \frac{\int_0^{2\pi} f_{\mathbf{c},\mathbf{s}}([\hat{x}+\eta\cos\gamma,\ \hat{y}+\eta\sin\gamma]^T,\mathbf{s})\cdot\eta\ d\gamma}{f_{\mathbf{s}}(\mathbf{s})}. \end{aligned} \tag{4.19}$$

Substituting (4.4) and (4.10) into (4.19), we have,

$$\hat{f}_{\eta|\mathbf{s}}(\eta|\mathbf{s}) = \frac{\int_0^{2\pi} \sum_{i=1}^{N_{\text{tr}}} K_{\mathbf{H}_i}(\begin{bmatrix} \hat{x} + \eta\cos\gamma \\ \hat{y} + \eta\sin\gamma \\ \mathbf{s} \end{bmatrix} - \mathbf{u}_i) \cdot \eta \; d\gamma}{\sum_{i=1}^{N_{\text{tr}}} K_{\mathbf{H}_i^s}(\mathbf{s} - \mathbf{s}_i)} \tag{4.20}$$

The conditional probability that the localization error is less than a given distance, r_0, can then be estimated as,

$$\text{Pr}_0 = \hat{\text{Pr}}(\eta \leq r_0|\mathbf{s}) = \int_{\eta=0}^{r_0} \hat{f}_{\eta|\mathbf{s}}(\eta|\mathbf{s}) \; d\eta. \tag{4.21}$$

For a given Pr_0, (4.21) could be used to obtain the radius of the corresponding RoC (e.g. 90% RoC) numerically, which is commonly shown as a circle centering the estimated location on a map.

4.3 Experimental Verifications and Discussions

4.3.1 Testbed Setup and Experimental Equipments

In order to verify the effectiveness of our proposed method, we have set up the experimental testbed in our lab, as shown in Fig. 4.1. Three Linksys-WRT54G wireless routers are deployed in the testbed as APs, broadcasting beacon frames periodically in channels 1, 6, and 11, respectively, in order to minimize frame collisions. A Fujitsu S6410 notebook equipped with an Intel Wireless WiFi Link 4965AGN adapter, is used to collect RSS measurements. The Linux packet sniffer, tcpdump, is used to monitor the beacon frames transmitted by the APs. The MAC addresses of APs, timestamps, and the Received Signal Strength Indicator (RSSI)

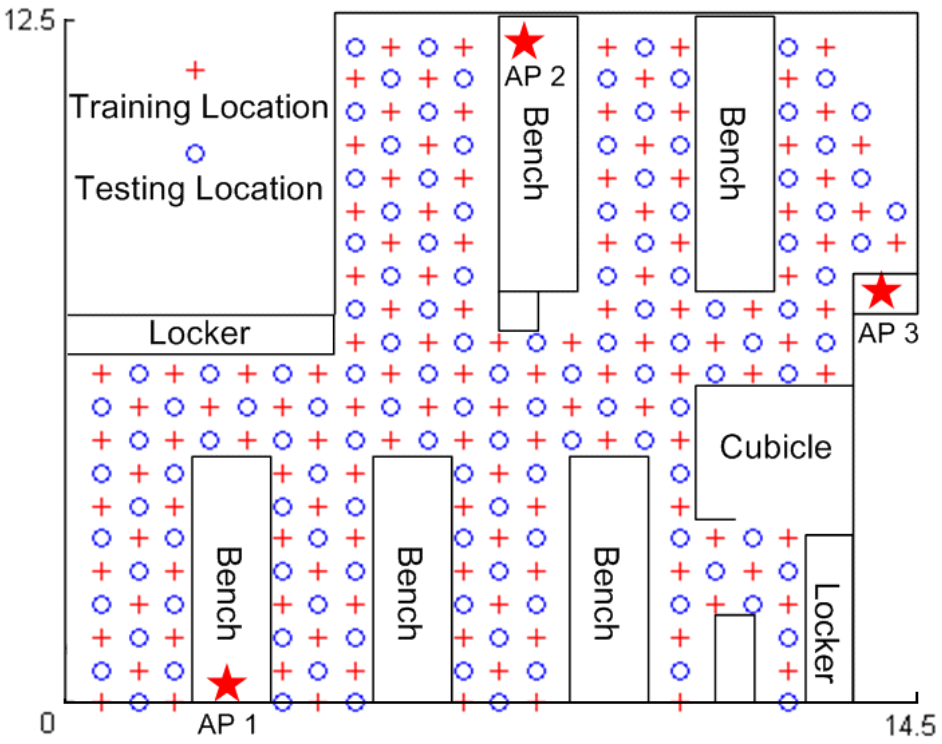

Fig. 4.1: Layout of the experimental testbed.

values are retrieved from the radiotap header of each captured packet. Note that, although the beacon frames from the APs arrive asynchronously, we can still use the timestamps of the arriving packets to synchronize the reported RSSI values and form RSS vectors.

The size of the testbed is approximately 130 m^2. Within the accessible area of the testbed, 125 training locations and 126 testing locations are uniformly selected, such that the spacing between adjacent training locations is 0.85 m and the spacing between a training location and its nearest testing location is 0.6 m. At each training location, 50 training RSS vectors are collected. At each testing location, 5 testing RSS vectors are collected, resulting in 630 testing cases in our experiment.

4.3.2 Statistical Verification

Let us denote the j^{th} testing data sample as, $(\mathbf{c}^{(j)}, \mathbf{s}^{(j)})$, and the corresponding location estimate as $\hat{\mathbf{c}}^{(j)}$, for $j = 1, 2, ..., N_{\text{te}}$, where $N_{\text{te}} = 630$. From the testing samples, we can compute the error PDF, $\hat{f}_{\eta|\mathbf{s}^{(j)}}(\eta|\mathbf{s}^{(j)})$, for each testing online RSS vector, $\mathbf{s}^{(j)}$. However, it is not possible to verify its correctness individually, since the pair of estimated location and ground truth corresponding to $\mathbf{s}^{(j)}$ only gives us a single error distance value for η. Therefore, rather than verifying each error PDF individually, we derive the overall error PDF conditioned on the entire testing set, S_{te}, i.e.,

$$\hat{f}(\eta|S_{\text{te}}) = \frac{\sum_{j=1}^{N_{\text{te}}} \hat{f}_{\eta|\mathbf{s}^{(j)}}(\eta|\mathbf{s}^{(j)}) \cdot \hat{f}_{\mathbf{s}^{(j)}}(\mathbf{s}^{(j)})}{\sum_{j=1}^{N_{\text{te}}} \hat{f}_{\mathbf{s}^{(j)}}(\mathbf{s}^{(j)})}, \tag{4.22}$$

where $\hat{f}_{\eta|\mathbf{s}^{(j)}}(\eta|\mathbf{s}^{(j)})$ and $\hat{f}_{\mathbf{s}^{(j)}}(\mathbf{s}^{(j)})$ can be obtained from (4.20) and (4.10). From here, we can estimate the overall error Cumulative Density Function (CDF) and compare it with the empirical error CDF to indirectly verify the correctness of our approach. In order to predict the error CDF, we compute $\hat{f}(\eta|S_{\text{te}})$ for η ranging from 0 m to 10.5 m (experimentally determined), with a step size of 0.5 m. Simple rectangle-rule-based numerical integration is then applied to give the discrete error CDF prediction. For the empirical error CDF, we apply the Kaplan-Meier algorithm implemented in the MATLAB "ecdf()" function, on the actual error distances.

We have chosen the two most widely adopted fingerprint-based localization methods, namely, KNN and probabilistic approach, for our study. As shown in Fig. 4.2, our empirical error CDFs are comparable with that in [28] although our testbed is different from theirs. In both cases, the predicted error CDFs computed by our proposed scheme track the empirical error CDFs closely. In particular, comparison of the mean error distance, and error distances corresponding to 0.25,

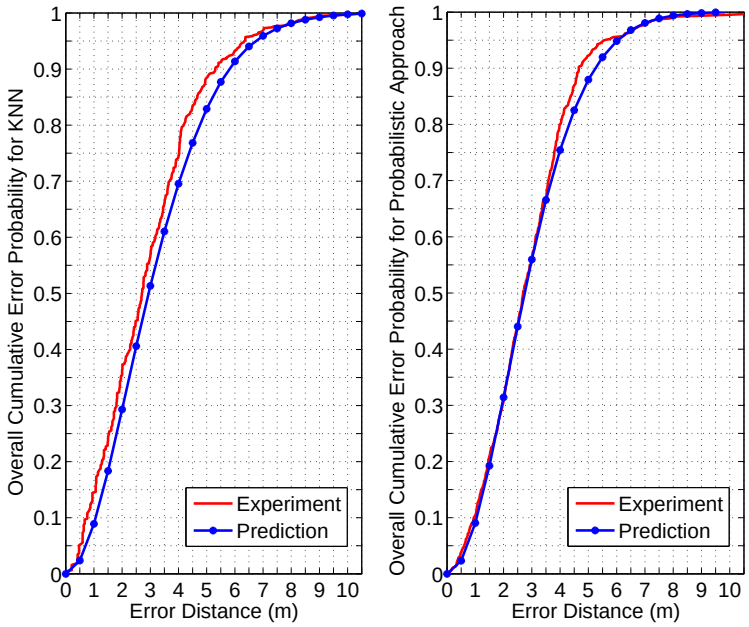

Fig. 4.2: Comparison of predicted and empirical error CDFs.

Table 4.1: Comparison between empirical and predicted error (in meters)

	KNN		Probabilistic	
	Empirical	Predicted	Empirical	Predicted
CEP = 0.25	1.51	1.81	1.74	1.73
CEP = 0.50	2.69	2.93	2.69	2.75
CEP = 0.75	4.02	4.37	3.79	3.97
Mean Error	2.94	3.24	2.88	2.99

0.50, and 0.75 overall cumulative error probabilities (CEP) between the predicted and the empirical data, are presented in Table I.

Chapter 5

DR-based Robust Pedestrian Tracking with Sparse Infrastructure Support

---

In this chapter, we propose an indoor pedestrian tracking system which fuses the DR estimate with range measurements from a sparse infrastructure. The DR estimate is obtained by a digital step counter and a digital compass, implemented using low cost sensors on a hand-held mobile device. The ranging infrastructure can be deployed in such a sparse manner that, at any point within the service area, *at most one* LoS ranging BN can be heard, as it is done in our experimental testbed. The DR location estimate has a cumulative tracking error. Occasionally, when a range measurement from one infrastructure BN is heard, it can be used to constrain and correct the accumulated tracking error. We propose a particle-filter-based (PF-based) sensor fusion scheme to correct the tracking error for the general case in which the reporting rate and accuracy of the ranging system may vary.

A prototype of the proposed scheme is implemented for experimental verification with sensors on a hand-held device and a practical ranging system. As shown in the experimental results, the proposed scheme is able to provide significantly better tracking performance compared to a DR system alone, regardless of whether the knowledge of initial user location is available or not. Moreover, even when the range measurements are intermittent and noisy, our proposed system still delivers fairly accurate tracking performance.

5.1 Step-based Dead Reckoning with Hand-held Mobile Device

Before proceeding to describe the proposed method, we first briefly describe the step-based DR algorithm on a hand-held mobile device in this section. We have built the step-based DR sub-system using the accelerometer and magnetometer embedded in the Apple iPhone 4. Therefore we base our discussion on these sensors in this device for the rest of this chapter. However, despite the differences in the implementation details, the proposed scheme is applicable to a generalized hand-held mobile device equipped with similar sensors.

A typical step-based DR tracking system estimates pedestrian location by iteratively computing,

$$\mathbf{l}_i = \mathbf{l}_{i-1} + [\rho_i \cos\theta_i,\ \rho_i \sin\theta_i]^T, \tag{5.1}$$

in which $\mathbf{l}_{i-1}$ and $\mathbf{l}_i$ denote the locations before and after the i^{th} step is detected, respectively. ρ_i and θ_i denote the stride length and stride orientation of the i^{th} step, respectively. Next, we introduce the techniques to estimate both parameters.

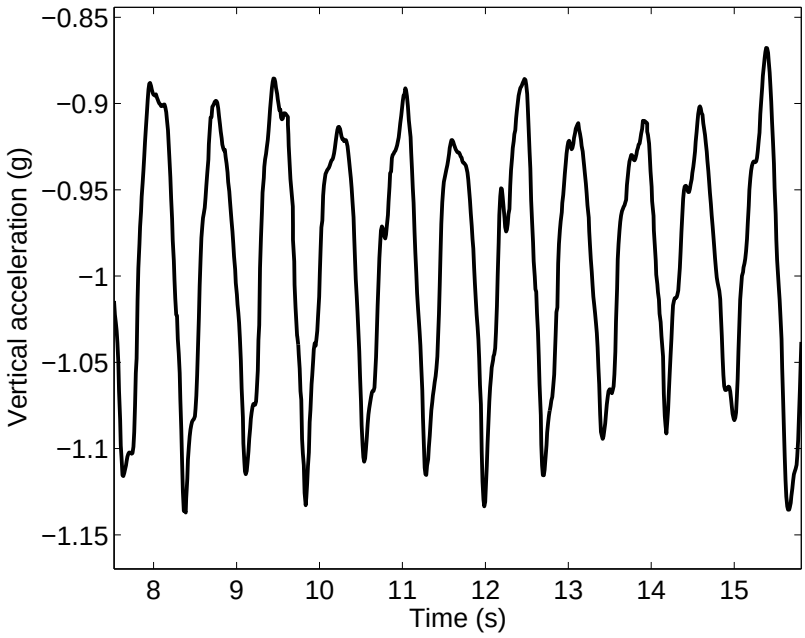

Fig. 5.1: Vertical acceleration variations over time for 11 steps.

5.1.1 Step Detection

In order to reduce the effect of measurement noise, the accelerometer's measurements on the vertical axis are first passed to a low-pass filtering window containing the readings of the most recent 200 ms, yielding smoothed vertical acceleration readings.

Fig. 5.1 shows the temporal variation of the smoothed vertical accelerations for 11 steps taken at normal walking speed. A new step is detected if a valid local minimum and a valid local maximum are detected in sequence. A local minimum is valid if it occurs at least 200 ms after the most recent valid local maximum, and the value of the vertical acceleration at the local minimum is smaller than that of the most recent local maximum by at least a threshold value, $\Delta_{\text{threshold}}$. Similarly, a local maximum is valid if it occurs at least 200 ms after the most recent valid

local minimum, and the value of the vertical acceleration at the local maximum is higher than that of the most recent local minimum by at least $\Delta_{\text{threshold}}$. The choice of the 200 ms time difference threshold is due to the fact that, at normal walking speed, humans approximately take two steps per second, which leads to four peaks correspondingly. Hence, it is reasonable to pick 200 ms as the minimum inter-peak time difference.

5.1.2 Stride Length Estimation

Practically, stride length varies from step to step even for the same pedestrian. An empirical adaptive model [59] relying on the walking acceleration pattern has been used to estimate the stride length in [39], in which the sensor module is mounted at the center back of the waist. However, in our case of a hand-held device, a user holds his device in one hand, off the center of his body, such that the steps from both legs can create different impact on the acceleration variations sensed by the device. Moreover, random movements of the upper body and arm of the pedestrian introduce more noise into the acceleration measurements. These factors have rendered the adaptive model in [59] unsuitable. We therefore resort to an average stride estimation scheme which also brings computational simplicity.

5.1.3 Step Parameter Calibration

The optimal values for both the step detection threshold, $\Delta_{\text{threshold}}$ and the average stride length vary among different users. Simple and convenient calibrations can be carried out to determine them. For example, $\Delta_{\text{threshold}}$ can be determined by requiring the user to walk a known number of steps and adjust $\Delta_{\text{threshold}}$ such that the correct number of steps are detected. On the other hand, the stride length can be determined by obtaining the actual distance covered by a user during a

calibration walking trial in which a fixed number of steps are taken.

5.1.4 From Magnetometer to Digital Compass

The magnetometer in the iPhone reports magnetic field strength measured in the device's local x, y, z coordinate system. Using the average accelerometer reading during a step, we first estimate the pose of the phone relative to the vertical direction. The Earth magnetic field strength can then be projected onto the horizontal plane, which indicates the North direction. Therefore, the yaw direction of the device can be retrieved.

In this section, for ease of implementation, we assume that, when a hand-held device is being used, the yaw direction of the device is aligned with the user's heading. Therefore, a simple method to estimate the direction of a step and to reduce the measurement noise would be to take the average of the yaw readings between the starting and ending time of that step. However, in a step taken when the user is turning, the yaw direction of the device will only be aligned with the true step orientation at the end of that step. By considering this fact, we estimate the user's heading by averaging over only the yaw readings collected during the last 200 ms of a step.

5.2 The Ranging Infrastructure

In this chapter, we have employed the Cricket Motes as BNs of our indoor ranging infrastructure. The Cricket-based range measurement is carried out between a BN and a listener node (LN). The BN periodically sends out an RF packet and an ultrasound pulse at almost the same time, t_0. Upon receiving the RF packet at time t_{RF}, the LN starts to wait for the ultrasound pulse to arrive.

Upon receiving the ultrasound pulse at time t_{US}, or upon a timeout event, the LN stops waiting and starts to listen for new RF packets.

Due to the huge difference between the speed of RF and ultrasound propagation, the difference between $t_{\mathrm{US}} - t_0$ and $t_{\mathrm{US}} - t_{\mathrm{RF}}$ is almost negligible. Therefore, $t_{\mathrm{US}} - t_{\mathrm{RF}}$ can be treated as the propagation time of the ultrasound signal. The LN-BN separation, d, can be computed as,

$$d = v_{\mathrm{US}} \cdot (t_{\mathrm{US}} - t_{\mathrm{RF}}), \tag{5.2}$$

where v_{US} is the speed of ultrasound in air at room temperature.

In order to reduce blocking of signals, the BNs are normally mounted on ceilings. Let h_v denote the vertical height difference between a BN mounted on the ceiling and the LN carried by the user. The distance, r, projected onto the 2-D plane is,

$$r = \sqrt{d^2 - h_v^2}. \tag{5.3}$$

For the rest of this chapter, unless otherwise stated, the term "range measurement" shall refer to the projected 2-D distance after taking the height difference into consideration.

5.3 The Value of Sparse Information

Suppose we have a DR-based indoor pedestrian tracking system in place and we would like to deploy an infrastructure in order to provide side information to improve location tracking. In this context, there is contention between several factors: having a finite set of resources; meeting coverage specifications; and satisfying accuracy requirements. One design choice is to use the limited infrastruc-

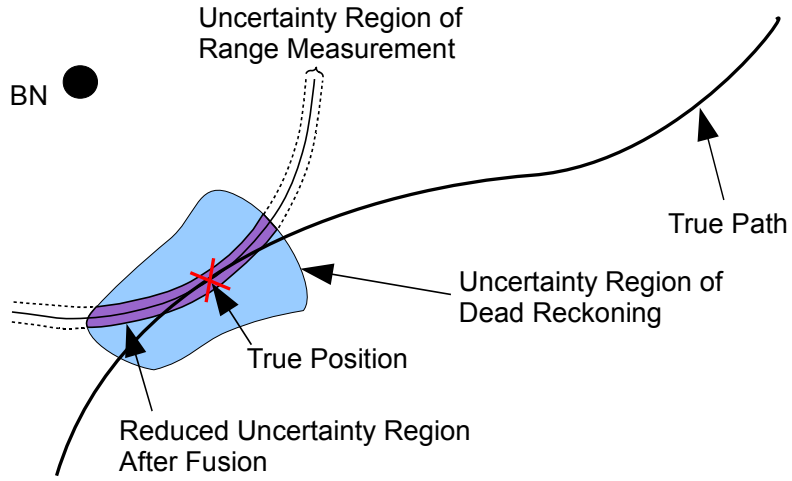

Fig. 5.2: Snapshot of uncertainty regions at a particular time instance.

ture resources to provide reliable and complete location information (e.g., using trilateration) for a small fraction of the service area. However, in real-life indoor environments such as museums, shopping malls, and campus buildings, users are constantly moving over a large service area. A better design tradeoff may be to deploy the limited infrastructure resources to provide partial location information over a larger service area in a sparse and intermittent manner. The intuition is that, although partial information such as the range from a single BN is ambiguous for location purposes on its own, it can be used as side information to reduce the uncertainty region for another location tracking system. This point can be illustrated in Fig. 5.2. The lightly shaded area is a snapshot of the uncertainty region of a mobile user being tracked by a DR system. The ringed area between the dotted lines is the uncertainty region of a sparse ranging system, which can lead to a large location uncertainty on its own. However, it can be used to significantly reduce location tracking error by considering its intersection with the DR uncertainty region. The reduced uncertainty region is represented by the dark shaded area.

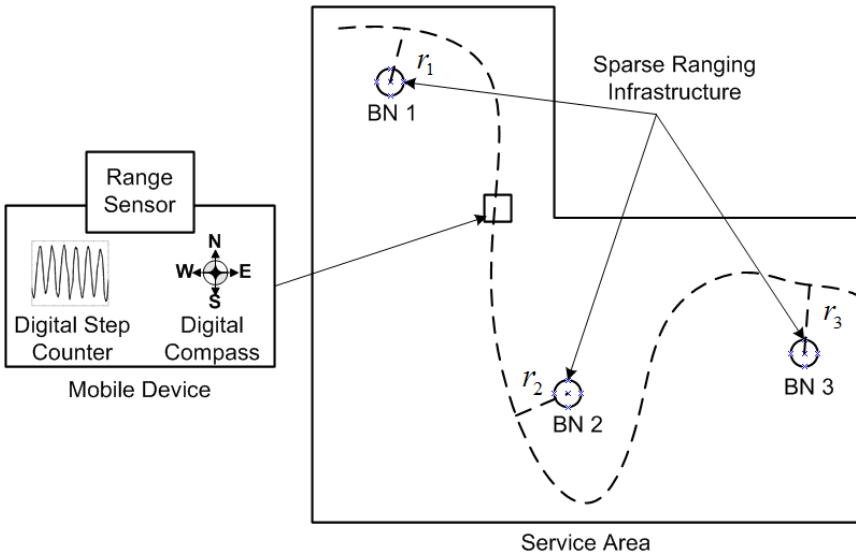

Fig. 5.3: The proposed system architecture.

5.4 System Architecture

In our proposed system as shown in Fig. 5.3, several ranging BNs are sparsely installed in the service area. Since occasional ranging coverage from only one LoS BN is sufficient for error reduction within the service area, the number of BNs is much smaller than that of a typical indoor trilateration system.

On the user side, a digital step counter, a digital compass, and a range sensor are integrated into a mobile device to be hand-held by the user. The digital step counter and the digital compass form the DR sub-system, which provides the displacement estimate relative to the initial user location, or to the last estimated user location. The range sensor and the ranging infrastructure form the ranging sub-system. The distance measurement to a nearby BN provided by this sub-system can be utilized to correct the accumulated tracking error. More importantly, when a mobile user first appears in the service area, the ranging sub-system is able to constrain the possible initial user locations.

Therefore, our tracking system is able to fuse the DR estimate and the range measurement. In the following sections, we first characterize both inputs probabilistically. Afterwards, we describe the PF-based tracking scheme.

5.5 Statistical Characterization

5.5.1 Step Estimates of the DR Sub-system

The i^{th} step is described by the stride length ρ_i and step orientation θ_i. The displacement vector of a step is $\mathbf{s}_i = [\rho_i \cos\theta_i, \rho_i \sin\theta_i]^T$.

The error in the estimated stride length is caused by the variations of stride length for each step taken, device noise, and irregular movements of the user's arm and body. We model this error by a zero-mean Gaussian random variable with standard deviation σ_ρ. The error in the orientation measurement is caused by device noise, irregular user arm movements, and distortion of Earth's magnetic field by nearby metallic objects. We similarly model this error by a zero-mean Gaussian random variable with standard deviation σ_θ.

5.5.2 Distance Estimates of the Ranging Sub-system

In order to correct the cumulative DR tracking error, the range measurements are treated as observations in the PF-based fusion scheme.

Let r_k denote the k^{th} range measurement. Let b_k denote the index of the BN from which this measurement is taken, and $\mathbf{l}_k = [x_k, y_k]^T$ denote the pedestrian location at which this measurement is taken, respectively. We assume that $r_k \sim N(\mu_k, \sigma_r^2)$, in which,

$$\mu_k = \sqrt{(x_k - x^{(b_k)})^2 + (y_k - y^{(b_k)})^2}, \tag{5.4}$$

where $[x^{(b_k)}, y^{(b_k)}]^T$ denotes the location of the BN indexed by b_k. σ_r denotes the standard deviation of the noise in the range measurements.

Therefore, we have,

$$f_{b_k}(r_k|\mathbf{l}_k) = \frac{1}{\sqrt{2\pi}\sigma_r} \exp\,[-\frac{(r_k - \mu_k)^2}{2\sigma_r^2}], \tag{5.5}$$

in which $f_{b_k}(r_k|\mathbf{l}_k)$ is the PDF to obtain a range measurement r_k from the BN indexed by b_k at the location $\mathbf{l}_k$.

5.6 Fusion by Particle Filter

In order to track $\mathbf{l}_k$, a PF uses a collection of N_s weighted samples, $\{\mathbf{l}_k^j, w_k^j\}, j = 1, 2, ..., N_s$, to approximate its conditional PDF, $f(\mathbf{l}_k|o_{0:k})$ [60],

$$f(\mathbf{l}_k|o_{0:k}) \approx \sum_{j=1}^{N_s} w_k^j \delta(\mathbf{l}_k - \mathbf{l}_k^j), \tag{5.6}$$

where $\delta(\cdot)$ is the Dirac-Delta function. The term $o_{0:k}$ denotes all the observations obtained up until the k^{th} update.

In this chapter, we choose the Sampling Importance Resampling (SIR) PF. The implementations, including initialization, sampling, weight update, and re-sampling, are briefly described as follows. More details regarding PF and SIR PF can be found in [60].

5.6.1 Initialization

In the special case where the starting location of the pedestrian is known and given as $[x_0, y_0]^T$, N_s identical samples can be generated as, $\{\mathbf{l}_0^j = [x_0, y_0]^T, w_0^j = \frac{1}{N_s}\}, j = 1, 2, ..., N_s$.

On the other hand, when the starting location is unknown, the initialization is performed based on the first range measurement, r_0, from the BN indexed by b_0, as follows. A collection of N_s samples, $\{\mathbf{l}_0^j, w_0^j = \frac{1}{N_s}\}, j = 1, 2, ..., N_s$, are uniformly generated in the service area. The weight, w_0^j, for each sample $\mathbf{l}_0^j$, is then multiplied by $f_{b_0}(r_0|\mathbf{l}_0^j)$, which is defined in (5.5).

Therefore, samples are weighted by their likelihood to obtain the first range measurement r_0 from the BN with index b_0.

5.6.2 Importance Sampling

Assume there are N_k steps detected between $(k-1)^{\text{th}}$ and k^{th} range measurements. Let the displacement vector of the i^{th} step detected between the $(k-1)^{\text{th}}$ and the k^{th} range measurements be denoted as,

$$\mathbf{s}_{k,i} = [\rho_{k,i} \cos\theta_{k,i}, \rho_{k,i} \sin\theta_{k,i}]^T, \tag{5.7}$$

in which $\rho_{k,i}$ and $\theta_{k,i}$ are the estimated stride length and orientation of this step, respectively.

Upon hearing the k^{th} range measurement, we first draw each of the N_s samples from the so-called "importance density", $f(\mathbf{l}_k|\mathbf{l}_{k-1}^j)$, based on these N_k detected steps between the $(k-1)^{\text{th}}$ and the k^{th} iteration, $\mathbf{s}_{k,i},\ i = 1,\ 2, ..., N_k$, and the samples from the previous iteration, $\{\mathbf{l}_{k-1}^j, w_{k-1}^j = \frac{1}{N_s}\}, j = 1, 2, ..., N_s$. In other words, we generate,

$$\mathbf{l}_k^j = \mathbf{l}_{k-1}^j + \sum_{i=1}^{N_k} \mathbf{s}_{k,i}^j, \text{ for } j = 1,\ 2, ...,\ N_s. \tag{5.8}$$

Note that for each sample j, we have,

$$\mathbf{s}_{k,i}^{j} = [\rho_{k,i}^{j} \cos\theta_{k,i}^{j}, \rho_{k,i}^{j} \sin\theta_{k,i}^{j}]^{T}, \tag{5.9}$$

in which the sample $\rho_{k,i}^{j}$ is obtained by adding a zero-mean Gaussian random number with variance σ_{ρ}^{2} to the estimated stride length $\rho_{k,i}$, and the sample $\theta_{k,i}^{j}$ is obtained by adding a zero-mean Gaussian random number with variance σ_{θ}^{2} to the estimated step orientation $\theta_{k,i}$.

5.6.3 Weight Update and Resampling

According to [60], when the importance density is $f(\mathbf{l}_k|\mathbf{l}_{k-1}^{j})$, the weight update from the $(k-1)^{\text{th}}$ iteration to the k^{th} iteration is accomplished as,

$$w_k^j \propto w_{k-1}^j \cdot f(o_k|\mathbf{l}_k^j). \tag{5.10}$$

The term $f(o_k|\mathbf{l}_k^j)$ denotes the likelihood for the observation o_k to be obtained at sample location, $\mathbf{l}_k^j$, at the k^{th} update. When the observation o_k is a range measurement, r_k, obtained from the BN indexed by b_k, we have,

$$f(o_k|\mathbf{l}_k^j) = f_{b_k}(r_k|\mathbf{l}_k^j), \tag{5.11}$$

in which $f_{b_k}(r_k|\mathbf{l}_k^j)$ is defined in (5.5).

The particle degeneracy problem may occur because the range measurement correction may cause some samples to receive very small weights. After several iterations, few particles would remain with meaningful weights. In order to address this problem, the SIR PF resamples the N_s particles $\{\mathbf{l}_k^j\}$ from the approximated PDF, $\sum_{j=1}^{N_s} w_k^j \delta(\mathbf{l}_k - \mathbf{l}_k^j)$. Each resampled particle is then weighted by $w_k^j = \frac{1}{N_s}$.

5.6.4 Location Estimator

Once the PDF $f(\mathbf{l}_k|r_{0:k})$ is approximated by the SIR PF, the real-time pedestrian location can be estimated. The minimum mean square error (MMSE) estimator is chosen in this chapter because it can be efficiently computed as,

$$\begin{aligned}
\mathbf{l}_{k|k} &= E\{\mathbf{l}_k|r_{0:k}\} \\
&= \int \mathbf{l}_k f(\mathbf{l}_k|r_{0:k}) d\mathbf{l}_k \\
&= \int \mathbf{l}_k \sum_{j=1}^{N_s} \frac{1}{N_s} \delta(\mathbf{l}_k - \mathbf{l}_k^j) d\mathbf{l}_k \\
&= \frac{1}{N_s} \sum_{j=1}^{N_s} \int \mathbf{l}_k \delta(\mathbf{l}_k - \mathbf{l}_k^j) d\mathbf{l}_k \\
&= \frac{1}{N_s} \sum_{j=1}^{N_s} \mathbf{l}_k^j, \qquad (5.12)
\end{aligned}$$

which is simply the average of the resampled particles.

It is easy to see that, when the initial location is unknown, the MMSE estimator for the initial location is simply the location of the BN from which the first range measurement is made.

5.7 Experiments and Discussions

5.7.1 Sensor Evaluation for Sub-systems

DR Sub-system

The proposed PF-based tracking scheme requires two parameters to be determined for the DR sub-system, namely, the standard deviation of stride length estimation error σ_ρ, and the standard deviation of stride orientation estimation

error σ_θ.

In order to obtain σ_ρ, 20 ten-step straight-line walking trials are carried out. The actual distance covered in each trial is measured. The resulting error standard deviation for ten-step straight-line walking is 0.203 m. If we treat the ten strides as independent and identically distributed (iid) random variables, the standard deviation of stride length estimation error for each step is $\frac{0.203}{\sqrt{10}} = 0.064$ m. In order to account for the disturbance caused by irregular body movements and noise in the acceleration measurements, we set σ_ρ to be 0.1 m in our experiments.

Note that, the average stride length of the 20 trials is 0.58 m, which means the error standard deviation per meter travelled in the stride length estimation is roughly, $\frac{0.064 \text{ m}}{0.58 \text{ m}} = 0.11$ m/meter. It is much larger than that of the wheel encoder used in [47], which has a error standard deviation of 0.001 m/meter travelled.

The magnetometer-based digital compass is vulnerable to both its inherent bias and distortion of Earth's magnetic field caused by metallic furniture. This is illustrated in Fig. 5.4, which are the temporal fluctuations of yaw measurements of the digital compass for 3 walking paths involving a 90 degree turn. Paths taken in Fig. 5.4(b) and Fig. 5.4(c) have exactly the same starting directions but different starting locations, such that the path in Fig. 5.4(b) is far away from any metallic furniture but the path in Fig. 5.4(c) is in the proximity of a metallic cabinet. The path taken in Fig. 5.4(a) starts with a different orientation with no metallic furniture nearby.

Several observations can be made from Fig. 5.4. First, during the straight-line portions of the walking paths in Fig. 5.4(a) and Fig. 5.4(b), the orientation measurements fluctuate within a reasonable range. Second, although the actual turning angles are the same, the differences in average path orientation measurements before and after the turn are 77.9 degrees and 117.6 degrees, respectively,

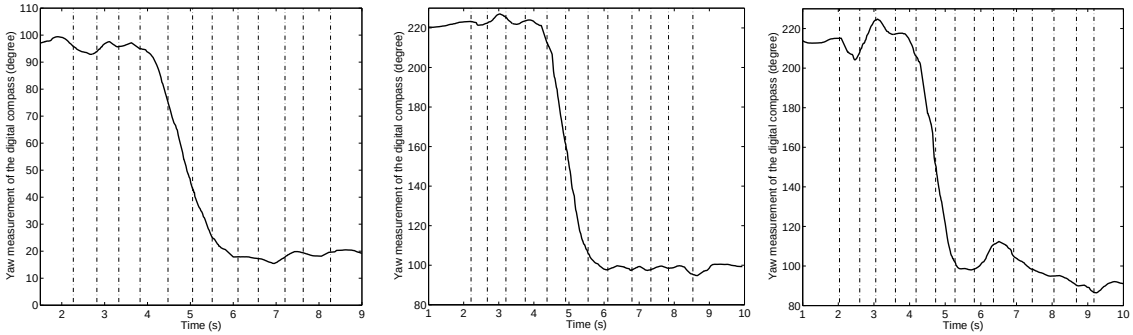

(a) Starting orientation 1 without metallic furniture.

(b) Starting orientation 2 without metallic furniture.

(c) Starting orientation 2 with metallic furniture.

Fig. 5.4: Difference in yaw measurements of the digital compass in walking trials with and without the presence of metallic furniture. Note: the vertical dash-dot lines mark the instances of detected steps.

for Fig. 5.4(a) and Fig. 5.4(b). Even for the case where both paths are far away from metallic furniture, Fig. 5.4(a) and Fig. 5.4(b) report different turning angles. More importantly, the existence of a metallic cabinet introduces significantly larger fluctuations in Fig. 5.4(c). Considering these factors, we reasonably set the standard deviation in the orientation measurement error to be 20 degrees.

Ranging Sub-system

Fig. 5.5 shows the histograms for the Cricket ranging data with BN-LN separation of 1 m and 2 m respectively. In both cases, the range measurements have some offsets from the true separations. Through experiments, we have discovered that there is a near-linear relationship between these offsets and the measured ranges. Therefore, the offsets can be easily compensated for any calibrated BN-LN combination. The offset versus measured range relationship is plotted in Fig. 5.6 for a particular BN-LN combination.

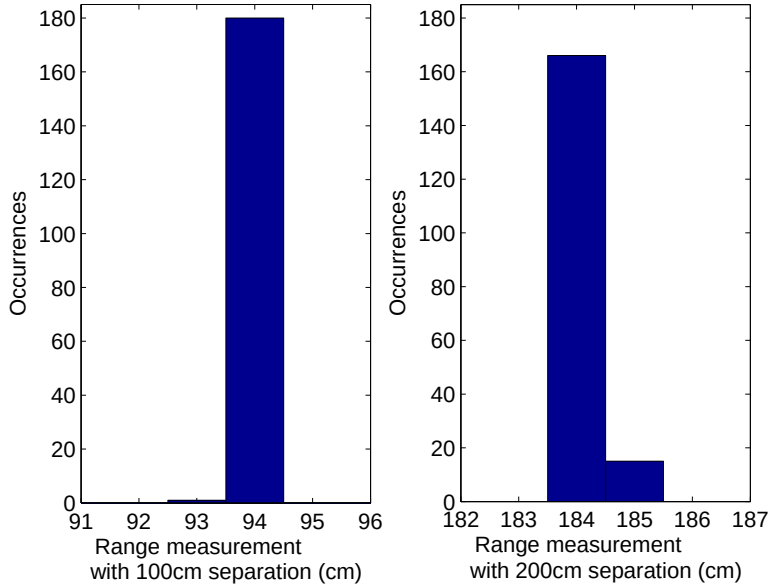

Fig. 5.5: Histograms for range measurements corresponding to 1m (left) and 2m (right) true separations.

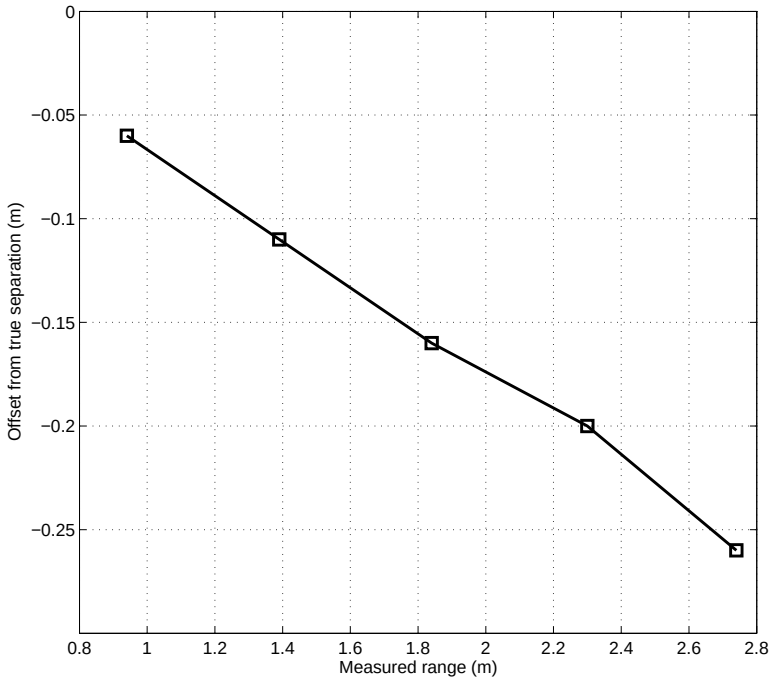

Fig. 5.6: Offset from true separation versus measured range.

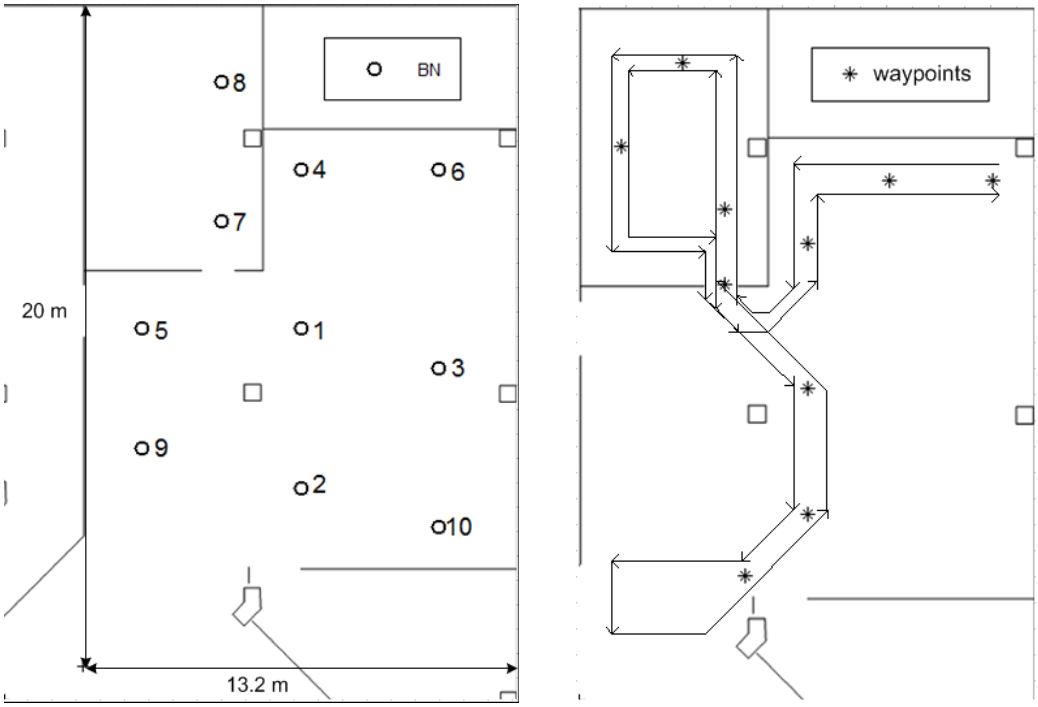

(a) Experimental testbed with dimensions and locations of BNs indicated.

(b) Experimental walking path with ground truth waypoints indicated.

Fig. 5.7: Experimental testbed and walking path.

5.7.2 Experimental Setup

Experimental Testbed and Infrastructure

In order to evaluate the tracking performance of the proposed scheme, we have chosen a laboratory on our campus as the indoor tracking testbed. The testbed is 13.2 m by 20.0 m by 2.5 m in dimension. It contains a common working area and a meeting room. The layout of the testbed is shown in Fig. 5.7(a) with walls and pillars indicated. As shown in Fig. 5.7(b), an indoor walking path is picked in our testbed. The path covers about 90 m in total distance, with various obstacles and turns. It takes about 2 minutes to walk along it, under normal indoor walking speed. Note that, actual distances covered and time taken for travel vary across

different experimental trials.

Ten Cricket Motes are installed on the ceiling in the testbed as BNs to form the ranging infrastructure. Therefore, the average BN density of our system is $0.04/\text{m}^2$. However, only a maximum of 6 BNs are actually used for range corrections in each round of our experiments. Compared to the trilateration system implemented with Cricket Motes in [4], in which 4 BNs are installed to cover a testbed of 3.04×2.43 m^2 with a BN density of $0.54/\text{m}^2$, our infrastructure deployment is much more sparse.

Note that, we intentionally choose such a sparse deployment of BNs in our testbed in order to illustrate that our system can benefit tremendously from very sparse side information. In practice, our proposed scheme has no difficulty working properly even when more than one range BN can be heard at any location.

In order to minimize the collisions between the BNs' RF packets, we implemented a simple TDMA-based BN transmission scheduling protocol, as follows. BN 1 transmits its RF packet (and the ultrasound pulse) once every second. Upon hearing BN 1's RF packet, BN n will wait for $t_w \cdot (n-1)$ amount of time before its own transmission. In our system, since there are 10 BNs, t_w is chosen to be 100 ms.

One Cricket Mote functioning as the LN is hand-held by the pedestrian together with the iPhone. The LN is kept at approximately 1.2 m above the ground. Whenever a range measurement, r, is made with respect to BN n, at time t, an RF packet containing the 3-tuple, $\{r_n,\ n,\ t\}$, is wirelessly sent to another Cricket Mote, labelled as the "Base Station", which is connected to a desktop personal computer (PC) through RS232 serial interface.

Through calibration, we have found that, although the RF beacon can be heard over a long distance, the ultrasound emitted by a BN mounted on the ceiling

cannot be heard by a LN at 1.2 m above ground when the horizontal distance is larger than 2.5 m. Therefore, due to our sparse testbed setup, the LN can measure the distance from *at most one* infrastructure BN at any given location. Moreover, the raw range measurements after compensation are only treated as valid if they fall within the range $[1.3\text{ m}, 2.8\text{ m}]$ (because $\sqrt{1.3^2 + 2.5^2} \approx 2.8$). We note that invalid readings may be caused by reflected ultrasound signals.

Synchronization of Sub-systems

Since the DR sub-system and the ranging sub-system are implemented on separate hardware with different system clocks, synchronization between these two sub-systems is critical for correct operation. For the convenience of off-line study, we synchronize both sub-systems to the desktop PC.

For the ranging sub-system, the LN reports its local timestamp t_{c} to the PC by sending a synchronization message through the RS-232 serial interface. The PC records its local timestamp t_{PC} when the LN's synchronization message is received. The clock offset for the ranging sub-system is computed as $\Delta_{\text{c}} = t_{\text{PC}} - t_{\text{c}}$.

Synchronization between the phone and the PC is accomplished wirelessly through a TCP socket connection, while they are both connected to the same wireless router. The PC sends a synchronization message SYNC1 to the phone and records the sending time t_1. Upon receiving SYNC1, the phone sends a synchronization message SYNC2 containing its local timestamp t_{p} back to the PC through the on-device Wi-Fi. The PC records the receiving time of SYNC2 as t_2. If we assume that both SYNC1 and SYNC2 spend almost the same amount of time travelling between the PC and the phone, the time offset between the phone and the PC can be computed as $\Delta_{\text{p}} = (t_1 + t_2)/2 - t_{\text{p}}$.

Ground Truth Collection

There are mainly two methods to collect ground truth for performance evaluation in the DR-based pedestrian tracking literature. The first method uses location coordinates provided by GPS [40]. It works only in the outdoor scenario. Moreover, commercial GPS's location estimation itself is subject to considerable error. The second method obtains ground truth relying on a reference DR unit [43], which is built on top of dedicated hardware with low noise and good updating rate. It can be foot-mounted on the tester so that ZUPT can be applied for noise cancellation. However, this approach is expensive and the reference DR system itself is still subject to error propagation over time.

For our experiment, we developed an efficient approach to collect accurate ground truth indoors, utilizing the mobile device and testbed setup. Along the walking path we have marked 10 distinctive locations as waypoints on the floor. Because each waypoint location is reached twice or thrice along the walking path, ground truth can be recorded and referred to for a total of 22 times in one walking trial. Note that, in order to maintain natural walking behavior, the pedestrians who participate in the experiment are not required to follow the path strictly as sketched in the figure, nor do they have to step on the waypoint locations precisely, as long as all the waypoints are *passed through exactly in the correct sequence*.

The pedestrian starts one trial of experiment by tabbing the "Start" button on the touch screen of the device. The device will instantly start sensor data collection. Whenever the pedestrian is passing through a certain waypoint on the walking path, he will tab the "Waypoint" button on the touch screen of the device, which will record the timestamp of this particular instance of passing. Therefore, 22 pieces of ground truth with timestamps can be collected accurately and efficiently for each trial of experiment. The estimated location, at the instance when

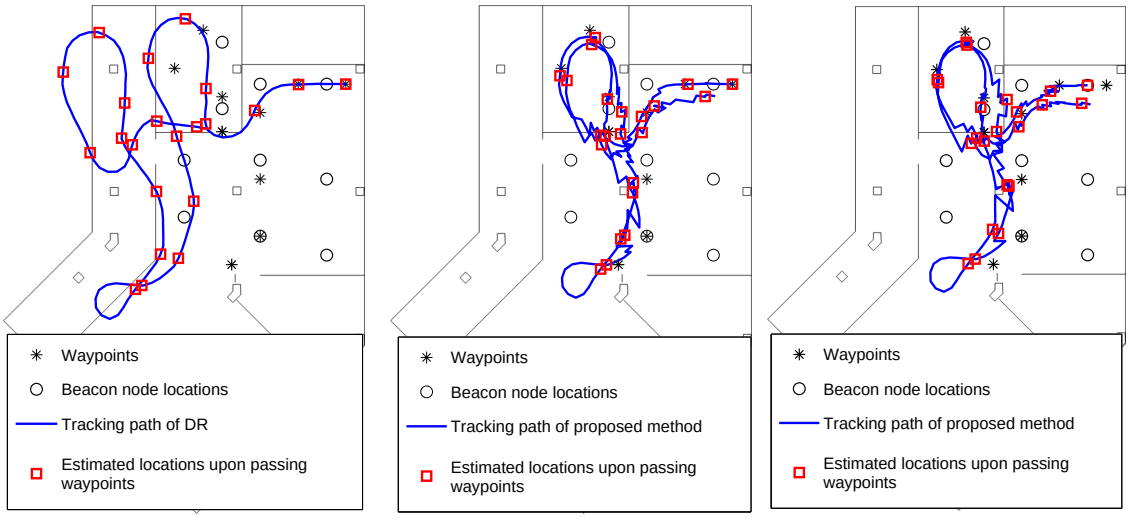

(a) Tracking path of DR.

(b) Tracking path of the proposed scheme with the knowledge of initial location.

(c) Tracking path of the proposed scheme without the knowledge of initial location.

Fig. 5.8: Tracking paths of DR and proposed scheme, both with and without the knowledge of the initial location.

a certain actual waypoint is passed by, can be compared to the actual waypoint location for error distance computation.

5.7.3 Tracking Performance

Sample Tracking Path

The estimated user trajectories by the proposed scheme, both with and without the knowledge of initial location, are visualized for better understanding in Fig. 5.8(b) and Fig. 5.8(c), respectively, for a sample experimental trial. The performance of the DR algorithm for the same trial is also provided for comparison purpose in Fig. 5.8(a). The corresponding temporal error propagations are shown in Fig. 5.9(a) and Fig. 5.9(b), respectively. As shown in these figures, errors in both the stride length estimation and the digital compass output cause the tracking errors in the DR estimation to accumulate quickly over time.

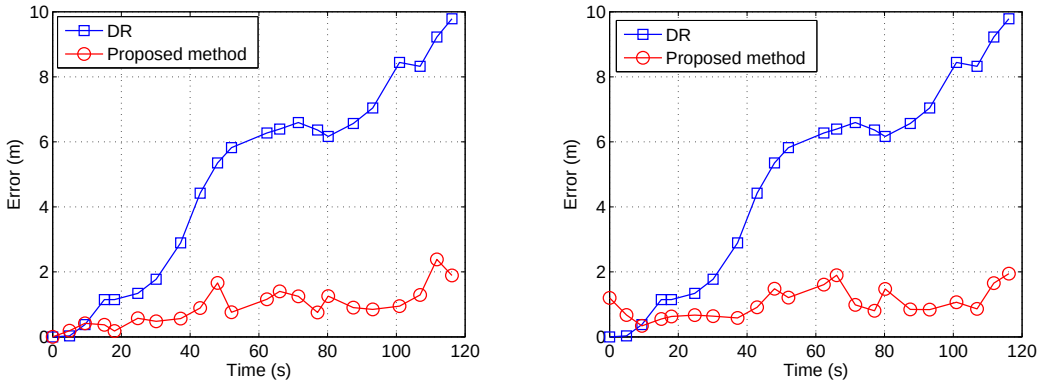

(a) Temporal error propagation of the proposed scheme with the knowledge of initial location.

(b) Temporal error propagation of the proposed scheme without the knowledge of initial location.

Fig. 5.9: Temporal tracking error propagation of the proposed scheme with and without the knowledge of the initial location.

On the other hand, the proposed scheme can effectively constrain error propagation with the aid of the sparse ranging infrastructure. Occasionally, when a range measurement is obtained from a certain BN, the particles representing the accumulated uncertainty in the user location are weighted by the likelihood of the reasonably accurate range measurement. Hence, the uncertainty in location can be significantly reduced.

Recall that, the proposed scheme starts tracking by making use of the first range measurement when the initial location is unknown. As shown in Fig. 5.9(b), initialization based solely on the first range measurement causes significantly larger tracking error at the beginning, compared to DR. However, as more range measurements are heard, the excess tracking error diminishes, and allows the proposed scheme to outperform the DR scheme rather rapidly.

After showing the sample tracking paths for the proposed scheme for a single trial of experiment, we study the performance of the proposed scheme under variations of different factors, including standard deviation of ranging errors, sparsity

of range corrections, and stride length errors. We use the average tracking error (in meter) as the performance metric. In the Fig. 5.10 to 5.13, each data point is the average of results obtained by repeating the tracking algorithm over 100 trials on the previously collected data. Each trial provides different results because there is some randomness in the injected range errors and the particle filter implementation. As mentioned, each trial provides 22 ground truth comparisons for tracking error computation. Therefore, each data point is the average of 2200 error values. We also show the 95% confidence interval for each data point on the graph whenever applicable, in order to indicate the reliability of the results.

Effect of Ranging Errors

Apart from the easily compensated near-linear offsets in the range measurements as described previously, the Cricket ranging technology provides rather accurate range information. In order to study the effect of ranging errors on tracking performance for a more general ranging system, we intentionally inject a zero-mean Gaussian random error into each range measurement. Fig. 5.10 shows the average tracking error corresponding to different standard deviations of the injected pseudo-random ranging error. As expected, the average error of the proposed scheme increases when the standard deviation of the range measurement's error gets larger. However, an interesting observation can also be made here; the excess tracking error caused by the lack of initial location information could be compensated by the availability of more accurate range measurements. For example, the average tracking error for the case where the initial location is known and the ranging error's standard deviation is 0.5 m, is comparable with that of the case where the initial location is unknown and the ranging error's standard deviation is 0.3 m.

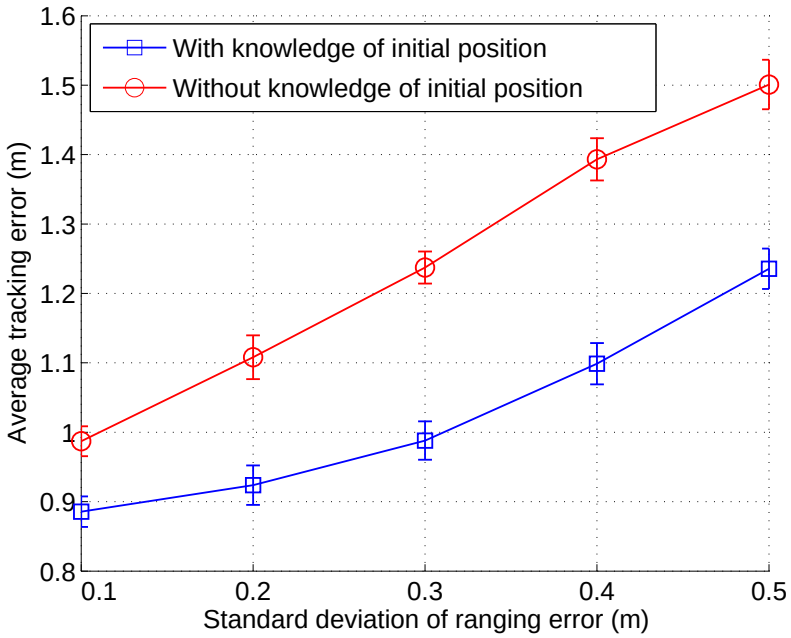

Fig. 5.10: Average tracking error vs. standard deviation of errors injected into range measurements.

Effect of Varying Sparsity

In this section, we study the robustness of the tracking performance when the range measurements become more sparse both temporally and spatially. In practice, temporal sparsity may be caused by heavy interference, or perhaps due to the user device's power conservation strategies that turn off its receiver every now and then. On the other hand, the shortage of infrastructure BNs may cause spatial sparsity.

In order to emulate temporal sparsity of range measurements, we repeat the algorithm on the collected data, for both cases with and without the knowledge of initial location. However, each time a range measurement occurs, the algorithm randomly decides whether to accept it or not, with chosen probability values of 0.25, 0.5, 0.75, or 1.

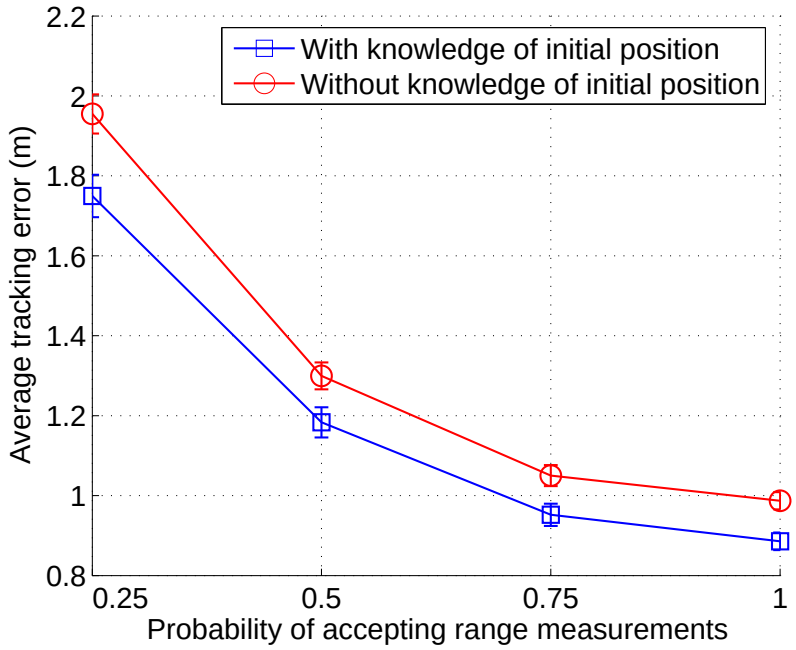

Fig. 5.11: Average tracking error vs. probability of accepting range measurements.

We set the ranging error's standard deviation to be 0.1 m. As shown in Fig. 5.11, the average tracking error decreases rapidly as the range measurements become more frequent. For comparison, note that the simple DR with known initial location delivers an average error of 4.79 m for our experimental walking path. We observe that even when the initial location information is not available, and only half of the range measurements are utilized for fusion, the proposed algorithm still reduces the average error by 72.9%, compared to the case of DR with knowledge of initial location.

In order to emulate the effect of spatial sparsity of BNs, we repeat the algorithm on the collected data for both cases with and without initial location information, by accepting range measurements from only a subset of BNs encountered on the path.

As shown in Fig. 5.12, as range measurements from more BNs are accepted for

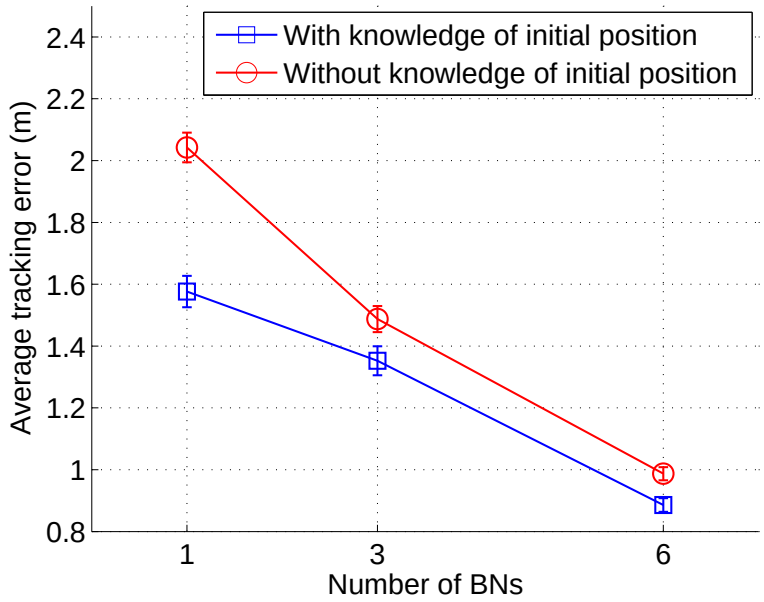

Fig. 5.12: Average tracking error vs. number of BNs whose range measurements are accepted.

fusion, the average tracking error decreases rapidly. Compared to simple DR with initial location given, the proposed scheme is able to reduce the average tracking error by 57.4%, even when the initial location information is not available, and range measurements from only one BN are used.

In order to study the performance of the proposed scheme when both spatial and temporal sparsity are present, we set the probability of accepting range measurements to be 0.25 and only utilize the range measurements from one BN (besides the first range measurement used for initialization). The average tracking errors for the experimental walking path under these settings are listed in Table 5.1, for both cases with and without the knowledge of initial location. As shown in the table, even when the range measurements are extremely sparse, the proposed scheme is still able to achieve observable error reductions of up to 43.6%

Table 5.1: Average error and rate of corrections of the proposed scheme with both temporal and spatial sparsity

	When all the range measurements are used from six BNs	**When 25% of the range measurements are used from only one BN**
Average tracking error with knowledge of initial location (meter)	0.88 (81.6%)	2.60 (45.7%)
Average tracking error without knowledge of initial location (meter)	0.98 (79.5%)	2.70 (43.6%)
Average correction rate (per second)	0.46	0.028

Note: The percentage values in the brackets represent the reduction in average tracking error compared to the DR approach. Each average error value reported in the table is computed over 2200 data samples. The worst case (maximum) 95% confidence interval among the average error values is 0.089 m.

when the knowledge of the initial location is not available. Note that, such a significant amount of error reduction is achieved when there are only 0.028 corrections per second on average.

Effect of Calibration Error in Stride Length Constant

The stride length ρ needs to be calibrated for each individual user. In this section, we study the effects of calibration errors in ρ on the tracking performance.

In our experiments, the value of the calibrated ρ is $\rho_{\text{cal}} = 0.58$ m. Fig. 5.13 shows the average tracking errors of the proposed scheme for the experimental walking path for $\rho = 0.5\rho_{\text{cal}}$ to $1.5\rho_{\text{cal}}$, with a $0.1\rho_{\text{cal}}$ step size. As can be observed, the average tracking errors are all kept below 2.5 m. The proposed scheme is able to limit the effects of the stride length calibration error because of the range corrections.

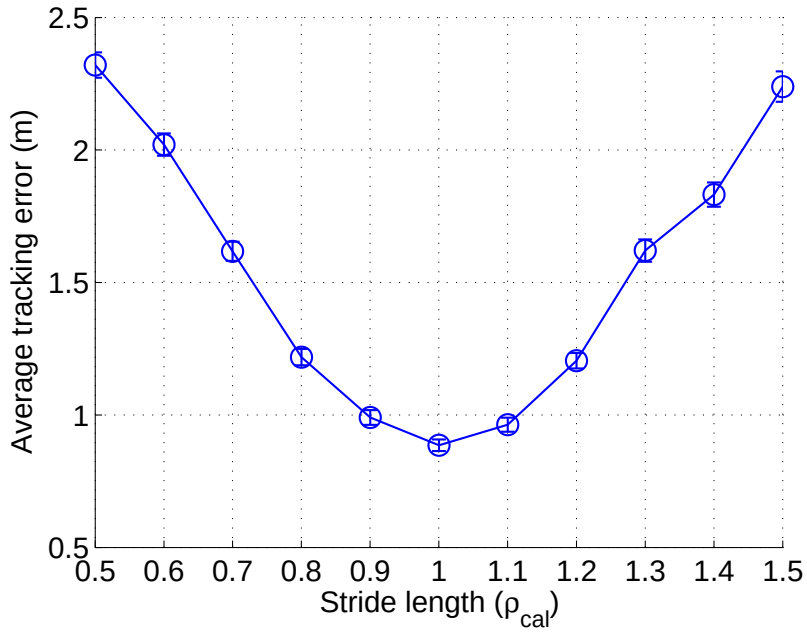

Fig. 5.13: Average tracking error vs. stride length.

Chapter 6

DR-based Robust Pedestrian Tracking with Two Sensor Modules

In this chapter, we propose a robust pedestrian tracking scheme using low cost DR sensors, which exploits the stable relative displacements between two sensor modules carried by the same pedestrian. We formulate the tracking task as a maximum a posteriori (MAP) sensor fusion problem and derive the optimal solution. We experimentally evaluate our proposed scheme by using, (i)two DR devices, each containing a single orientation sensor, mounted with arbitrary device orientations, (ii)one DR device, containing two different orientation sensors, mounted with fixed device orientation. Our proposed scheme has exhibited robust tracking performance with significant error reductions, compared to traditional DR, in both scenarios.

6.1 Dead Reckoning with Arbitrary Device Orientation

Before proceeding to describe the proposed method, we first briefly introduce the state-of-the-art pedestrian DR tracking algorithm with arbitrary device orientation.

We have used two Android-based smartphones (HTC Magic and Google NexusOne) as our experimental devices for the scenario of tracking with arbitrary device orientation in this chapter. Both smartphones are equipped with 3-axis accelerometer and 3-axis digital compass. We therefore based our discussions in this chapter on these sensors in the devices. However, despite the differences in the implementation details, the proposed scheme is applicable to generalized mobile devices equipped with similar sensors.

6.1.1 Orientation Projection for Arbitrary Device Posture

Practically, devices such as mobile phones or PDAs are very likely to be placed with arbitrary orientation. Therefore, the first step of pedestrian tracking in such scenarios is to project the phone's acceleration measurements reported in its x-y-z local coordinate system into the East-North-Up (E-N-U) world coordinate system, using the digital compass' orientation measurements.

The three orientation measurements (pitch, roll, yaw) reported by the Android API represent a sequence of rotations of the phone, starting from the initial orientation in which its x-y-z local coordinate system is aligned with the E-N-U world coordinate system. The three rotations are performed in an extrinsic manner. Rotations about the Up axis (yaw), the North axis (roll), and the East axis (pitch) are applied in sequence. In order to obtain the acceleration values in the

world coordinate system, we multiply the inverse of the corresponding rotation matrices in the reversed order (inverse pitch, inverse roll, and inverse yaw) to the acceleration vector reported in the local coordinate system.

6.1.2 Noise Filtering

Both the accelerometer and the digital compass in the smartphones give noisy measurements. In this chapter, we adopt low-pass filters (LPF) for noise reduction. However, the fluctuating orientation measurements reported by the Android API often experience sudden changes between two edge values such as 0 and 360 degrees, or -180 and 180 degrees. Applying LPF in these cases would cause the filtered measurements to be opposite or perpendicular to the true orientations. Therefore, we perform the filtering operation as follows. The raw acceleration measurements are passed into a pre-LPF with 200 ms window width. Next, the pre-filtered acceleration measurements are projected into the E-N-U world coordinate system, using the latest raw orientation measurements. Effects of the orientation noise are reduced indirectly by passing the projected accelerations to a post-LPF with 200 ms window width.

6.1.3 Step Detection and Stride Length Calibration

After the acceleration measurements have been projected into the E-N-U world coordinate system as described above, the step detection and stride length calibration can be executed similarly as described in Chapter 5.

6.1.4 Heading Orientation

In [42], PCA is applied to the horizontal E-N plane to find the heading orientation, after the original accelerations are projected into the E-N-U world coordinate system. The same approach is verified in [43] experimentally. However, [43] uses a dedicated inertial measurement unit (IMU), with a sensor data updating rate of 50 Hz. On the other hand, the low cost sensors in our Android smartphones have a non-uniform data updating rate of less than 25 Hz on average. Therefore, we only have fewer than half of the data samples compared to [43] for PCA-based heading detection, which delivers poor performance.

Limited by the low cost sensor's hardware data reporting rate, we choose a different heading detection scheme. The adopted scheme performs trapezoidal-rule-based numerical integration over the acceleration readings that are projected onto the E-N 2-D plane, over the latest 1.4 seconds (for about two steps), in order to approximate the current heading direction. Through experiments, it proves to be a simple and effective scheme.

6.2 System Architecture and Assumptions

Assume that the pedestrian is carrying two DR modules, each with arbitrary device orientation, labelled by module A and module B, respectively. Each module is capable of performing DR location tracking on its own, with *independent tracking error*.

We also assume that, the two modules have reasonably stable relative displacement with respect to each other. Mathematically speaking, if we let $\mathbf{l}_i^A$ and

$\mathbf{l}_i^B$ denote the coordinates of locations for the two modules at the i^{th} step, we have,

$$\mathbf{l}_i^A = \mathbf{m}_i^A + \mathbf{v}_i^A, \tag{6.1}$$

and,

$$\mathbf{l}_i^B = \mathbf{m}_i^B + \mathbf{v}_i^B, \tag{6.2}$$

where both $\mathbf{m}_i^A$ and $\mathbf{m}_i^B$ are vectors representing deterministic and fixed displacements with respect to the center of pedestrian motion, while $\mathbf{v}_i^A$ and $\mathbf{v}_i^B$ are random vectors which account for the limited local random movements of the two modules. $\mathbf{v}_i^A$ and $\mathbf{v}_i^B$ are uniformly distributed within a spherical region centered at $\mathbf{0}$ with radii r_A and r_B, respectively. In order to simplify notations, assume $r = r_A = r_B = \max\{r_A,\ r_B\}$.

Based on this model, we can normalize $\mathbf{m}_i^A = \mathbf{m}_i^B = \mathbf{m}_i$, where $\mathbf{m}_i$ is the center of motion at the i^{th} step, for the convenience of representation. Therefore the prior PDF for $\mathbf{l}_i^A$ and $\mathbf{l}_i^B$ is,

$$f(\mathbf{l}_i^A, \mathbf{l}_i^B) = \begin{cases} \kappa & \text{if } \|\mathbf{l}_i^A - \mathbf{l}_i^B\| \leq 2r, \\ 0 & \text{otherwise,} \end{cases} \tag{6.3}$$

where κ is a constant whose value is dependent on the dimension of the tracking problem and the radius of uncertainty region, r. $\|\cdot\|$ is the magnitude of a vector. Note that, (6.3) implies that it is equally likely for the two modules to be at any pair of locations as long as their inter-distance is less than or equal to $2r$.

6.3 The Robust Tracking Algorithm

6.3.1 Initialization

The DR system alone is only able to estimate the displacement vector but not the initial location. In order to initialize, the starting location, $\mathbf{m}_0$, must be provided to the DR system through either user indication or some other localization technologies.

Recall that, $\mathbf{l}_i^A = \mathbf{m}_i + \mathbf{v}_i^A$ and $\mathbf{l}_i^B = \mathbf{m}_i + \mathbf{v}_i^B$ are the locations of the two modules after the fixed displacements with respect to the center of motion are normalized. In order to initialize, we conveniently assume that, $\mathbf{v}_0^A = \mathbf{v}_0^B = \mathbf{0}$. Therefore, $\mathbf{l}_0^A = \mathbf{l}_0^B = \mathbf{m}_0$.

6.3.2 Maximum A Posteriori Sensor Fusion

Let $\hat{\mathbf{l}}_i^A$ and $\hat{\mathbf{l}}_i^B$ denote the DR estimates reported by the two modules independently at the i^{th} step. The fusion task is to find $\mathbf{l}_i^A$ and $\mathbf{l}_i^B$ which maximize the a posteriori PDF, $f(\mathbf{l}_i^A,\ \mathbf{l}_i^B \mid \hat{\mathbf{l}}_i^A,\ \hat{\mathbf{l}}_i^B)$. In other words, we need to solve the following optimization problem,

$$\underset{\mathbf{l}_i^A, \mathbf{l}_i^B}{\text{maximize}} \quad f(\mathbf{l}_i^A,\ \mathbf{l}_i^B \mid \hat{\mathbf{l}}_i^A,\ \hat{\mathbf{l}}_i^B)$$

From this point onwards, we can drop the index term i for simplicity of representation, because the following discussions are all referring to the fusion algorithm at the i^{th} step.

According to Bayes' Theorem, we have,

$$f(\mathbf{l}^A,\ \mathbf{l}^B \mid \hat{\mathbf{l}}^A,\ \hat{\mathbf{l}}^B) = \frac{f(\hat{\mathbf{l}}^A,\ \hat{\mathbf{l}}^B \mid \mathbf{l}^A,\ \mathbf{l}^B) \cdot f(\mathbf{l}^A,\ \mathbf{l}^B)}{f(\hat{\mathbf{l}}^A,\ \hat{\mathbf{l}}^B)}. \tag{6.4}$$

Because the two modules provide independent DR estimates,

$$f(\mathbf{l}^A,\ \mathbf{l}^B \mid \hat{\mathbf{l}}^A,\ \hat{\mathbf{l}}^B) = \frac{f(\hat{\mathbf{l}}^A|\ \mathbf{l}^A) \cdot f(\ \hat{\mathbf{l}}^B|\ \mathbf{l}^B) \cdot f(\mathbf{l}^A,\ \mathbf{l}^B)}{f(\hat{\mathbf{l}}^A,\ \hat{\mathbf{l}}^B)}. \tag{6.5}$$

On the right hand side of (6.5), the evidence PDF in the denominator, $f(\hat{\mathbf{l}}^A,\ \hat{\mathbf{l}}^B)$, is not affected by the choice of either $\mathbf{l}^A$ or $\mathbf{l}^B$ because,

$$f(\hat{\mathbf{l}}^A,\ \hat{\mathbf{l}}^B) = \int f(\hat{\mathbf{l}}^A|\ \mathbf{l}^A) \cdot f(\ \hat{\mathbf{l}}^B|\ \mathbf{l}^B) \cdot f(\mathbf{l}^A,\ \mathbf{l}^B) d(\mathbf{l}^A,\ \mathbf{l}^B). \tag{6.6}$$

Therefore, maximizing $f(\mathbf{l}^A,\ \mathbf{l}^B \mid \hat{\mathbf{l}}^A,\ \hat{\mathbf{l}}^B)$ is equivalent to maximizing $f(\hat{\mathbf{l}}^A|\ \mathbf{l}^A) \cdot f(\ \hat{\mathbf{l}}^B|\ \mathbf{l}^B) \cdot f(\mathbf{l}^A,\ \mathbf{l}^B)$.

The terms $f(\hat{\mathbf{l}}^A|\ \mathbf{l}^A)$ and $f(\hat{\mathbf{l}}^B|\ \mathbf{l}^B)$ are the likelihood PDFs of observing $\hat{\mathbf{l}}^A$ and $\hat{\mathbf{l}}^B$, conditioned on the actual locations, $\mathbf{l}^A$ and $\mathbf{l}^B$, respectively. Due to the residual noise in filtered sensor measurements and irregularity in pedestrian body movements, each step's displacement is estimated with independent error. The likelihood PDF for the DR estimation for each estimation instance can therefore be modelled as Gaussian, according to the Central Limit Theorem (CLT). Similar assumption has been made in [48] for fusing the DR estimates with WLAN-based localization result.

Therefore, both $f(\hat{\mathbf{l}}^A|\ \mathbf{l}^A)$ and $f(\hat{\mathbf{l}}^B|\ \mathbf{l}^B)$ are Gaussian. The value of the prior PDF $f(\mathbf{l}^A,\ \mathbf{l}^B)$ in (6.3) is a positive constant within a spherical region and 0 elsewhere. The robust tracking task therefore becomes a constrained optimization problem as,

$$\begin{aligned} \underset{\mathbf{l}^A,\mathbf{l}^B}{\text{maximize}} \quad & f(\hat{\mathbf{l}}^A|\ \mathbf{l}^A) \cdot f(\ \hat{\mathbf{l}}^B|\ \mathbf{l}^B) \\ \text{subject to} \quad & \|\mathbf{l}^A - \mathbf{l}^B\| \leq 2r. \end{aligned}$$

We further observe that there are two cases in which the maximal value can

be obtained.

In the first case, $\|\hat{\mathbf{l}}^A - \hat{\mathbf{l}}^B\| \leq 2r$, which means the location estimates reported by the two DR modules are within a distance of $2r$. In this case, both Gaussian PDFs can obtain their maximal values (hence their product is maximized) at $\tilde{\mathbf{l}}^A = \hat{\mathbf{l}}^A$ and $\tilde{\mathbf{l}}^B = \hat{\mathbf{l}}^B$, while satisfying $f(\tilde{\mathbf{l}}^A,\ \tilde{\mathbf{l}}^B) \neq 0$. However, in this case, because the optimal $\tilde{\mathbf{l}}^A$ and $\tilde{\mathbf{l}}^B$ are close to each other, it is not necessary for the fusion to take place.

In the second case, $\|\hat{\mathbf{l}}^A - \hat{\mathbf{l}}^B\| > 2r$. The estimates reported by the two modules deviate from each other to such an extent that error correction needs to be done. In order to satisfy that $f(\mathbf{l}^A,\ \mathbf{l}^B) \neq 0$, the distance between the optimal $\tilde{\mathbf{l}}^A$ and $\tilde{\mathbf{l}}^B$ must be $2r$ in this case. This can be proven, almost trivially, by contradiction as follows. For simplicity, we only consider the 2-D case here.

Given that, the reported location estimates, $\hat{\mathbf{l}}^A$ and $\hat{\mathbf{l}}^B$, satisfy,

$$\|\hat{\mathbf{l}}^A - \hat{\mathbf{l}}^B\| > 2r, \tag{6.7}$$

and $f(\hat{\mathbf{l}}^A|\ \mathbf{l}^A) \cdot f(\hat{\mathbf{l}}^B|\ \mathbf{l}^B)$ is maximized at optimal points, $\mathbf{l}^A = \tilde{\mathbf{l}}^A$ and $\mathbf{l}^B = \tilde{\mathbf{l}}^B$, respectively, which satisfy $\|\tilde{\mathbf{l}}^A - \tilde{\mathbf{l}}^B\| = d < 2r$, draw two circles C_A and C_B centered at $\tilde{\mathbf{l}}^A$ and $\tilde{\mathbf{l}}^B$ with arbitrarily small radii p_A and p_B, respectively, such that $p_A + p_B + d < 2r$. If any point on C_A or C_B results in a larger $f(\hat{\mathbf{l}}^A|\ \mathbf{l}^A) \cdot f(\hat{\mathbf{l}}^B|\ \mathbf{l}^B)$, it would contradict the condition that $\tilde{\mathbf{l}}^A$ and $\tilde{\mathbf{l}}^A$ are the optimal feasible points. Therefore, both $\tilde{\mathbf{l}}^A$ and $\tilde{\mathbf{l}}^B$ must be the local maximum of the likelihood PDFs $f(\hat{\mathbf{l}}^A|\ \mathbf{l}^A)$ and $f(\hat{\mathbf{l}}^B|\ \mathbf{l}^B)$, respectively. However, each Gaussian PDF has only one local maximum which is also the global maximum. Therefore, $\tilde{\mathbf{l}}^A = \hat{\mathbf{l}}^A$ and $\tilde{\mathbf{l}}^B = \hat{\mathbf{l}}^B$, which contradicts the fact that $\|\hat{\mathbf{l}}^A - \hat{\mathbf{l}}^B\| > 2r$. Therefore, we must have, $\|\tilde{\mathbf{l}}^A - \tilde{\mathbf{l}}^B\| = 2r$ when the distance between the two reported location estimates $\hat{\mathbf{l}}^A$

and $\hat{\mathbf{l}}^B$ is larger than $2r$.

Consequently, the constrained optimization problem becomes,

$$\begin{aligned} \underset{\mathbf{l}^A,\mathbf{l}^B}{\text{maximize}} \quad & f(\hat{\mathbf{l}}^A|\ \mathbf{l}^A) \cdot f(\ \hat{\mathbf{l}}^B|\ \mathbf{l}^B) \\ \text{subject to} \quad & \|\mathbf{l}^A - \mathbf{l}^B\| = 2r. \end{aligned}$$

In order to solve it, let,

$$\mathbf{l}^B = \mathbf{l}^A + \mathbf{q} = [x_A + 2r\cos\phi,\ y_A + 2r\sin\phi]^T, \tag{6.8}$$

which eliminates the constraint and adds one more free variable, ϕ, to the maximization problem.

The objective function to be maximized can therefore be written as,

$$F = f(\hat{\mathbf{l}}^A|\ \mathbf{l}^A) \cdot f(\ \hat{\mathbf{l}}^B|\ \mathbf{l}^B) = f(\hat{\mathbf{l}}^A|\ \mathbf{l}^A) \cdot f(\ \hat{\mathbf{l}}^B|\ \mathbf{l}^A + \mathbf{q}) = Q \cdot \exp[G], \tag{6.9}$$

where,

$$Q = \frac{1}{4\pi^2 \cdot |\mathbf{R}_A|^{\frac{1}{2}} \cdot |\mathbf{R}_B|^{\frac{1}{2}}}, \tag{6.10}$$

and $\mathbf{R}_A$ and $\mathbf{R}_B$ are the covariance matrices for the Gaussian PDFs $f(\hat{\mathbf{l}}^A|\ \mathbf{l}^A)$ and $f(\hat{\mathbf{l}}^B|\ \mathbf{l}^B)$, respectively. We also have in the exponent,

$$G = -\frac{1}{2}(\mathbf{l}^A - \hat{\mathbf{l}}^A)^T\mathbf{R}_A^{-1}(\mathbf{l}^A - \hat{\mathbf{l}}^A) - \frac{1}{2}(\mathbf{l}^A + \mathbf{q} - \hat{\mathbf{l}}^B)^T\mathbf{R}_B^{-1}(\mathbf{l}^A + \mathbf{q} - \hat{\mathbf{l}}^B). \tag{6.11}$$

For the unconstrained objective function in (6.9), at the optimal point, we

have the equalities about its partial derivatives,

$$\frac{\partial F}{\partial x_A} = 0, \tag{6.12}$$

$$\frac{\partial F}{\partial y_A} = 0, \tag{6.13}$$

$$\frac{\partial F}{\partial \phi} = 0. \tag{6.14}$$

Correspondingly, by the Chain Rule, we have,

$$\frac{\partial F}{\partial G} \cdot [\frac{\partial G}{\partial \mathbf{l}^A}]^T \cdot \frac{\partial \mathbf{l}^A}{\partial x_A} = 0, \tag{6.15}$$

$$\frac{\partial F}{\partial G} \cdot [\frac{\partial G}{\partial \mathbf{l}^A}]^T \cdot \frac{\partial \mathbf{l}^A}{\partial y_A} = 0, \tag{6.16}$$

$$\frac{\partial F}{\partial G} \cdot [\frac{\partial G}{\partial \mathbf{q}}]^T \cdot \frac{\partial \mathbf{q}}{\partial \phi} = 0. \tag{6.17}$$

The term, $\frac{\partial F}{\partial G} = Q \cdot \exp[G]$, is always nonzero. Therefore, we can ignore it in further discussions.

The term $\frac{\partial G}{\partial \mathbf{l}^A}$ is evaluated as,

$$\frac{\partial G}{\partial \mathbf{l}^A} = -\mathbf{R}_A^{-1}(\mathbf{l}^A - \hat{\mathbf{l}}^A) - \mathbf{R}_B^{-1}(\mathbf{l}^A + \mathbf{q} - \hat{\mathbf{l}}^B). \tag{6.18}$$

Let,

$$\mathbf{l}^A = [x_A, y_A]^T, \tag{6.19}$$

$$\hat{\mathbf{l}}_A = [\hat{x}_A, \hat{y}_A]^T, \tag{6.20}$$

$$\hat{\mathbf{l}}_B = [\hat{x}_B, \hat{y}_B]^T. \tag{6.21}$$

We have,

$$\frac{\partial \mathbf{l}^A}{\partial x_A} = [1,0]^T, \tag{6.22}$$

$$\frac{\partial \mathbf{l}^A}{\partial y_A} = [0,1]^T. \tag{6.23}$$

The term $\frac{\partial G}{\partial \mathbf{q}}$ is evaluated as,

$$\frac{\partial G}{\partial \mathbf{q}} = -\mathbf{R}_B^{-1}(\mathbf{l}^A + \mathbf{q} - \hat{\mathbf{l}}^B). \tag{6.24}$$

The term $\frac{\partial \mathbf{q}}{\partial \phi}$ is evaluated as,

$$\frac{\partial \mathbf{q}}{\partial \phi} = [-2r\sin\phi,\ 2r\cos\phi]^T. \tag{6.25}$$

For any specific $\hat{\mathbf{l}}^A$, $\hat{\mathbf{l}}^B$, $\mathbf{R}_A$, and $\mathbf{R}_B$, (6.15) to (6.17) give us three linear equations, which can be solved for x_A, y_A, and ϕ.

However, the covariance matrices, $\mathbf{R}_A$ and $\mathbf{R}_B$, for DR estimates, are difficult to evaluate or estimate in general. Therefore, we further assume that,

$$\mathbf{R}_A = \sigma_A^2\mathbf{I}, \tag{6.26}$$

$$\mathbf{R}_B = \sigma_B^2\mathbf{I}, \tag{6.27}$$

in which $\mathbf{I}$ denotes the identity matrix. Following this assumption, we can simplify (6.15) to (6.17) to,

$$\frac{x_A - \hat{x}_A}{\sigma_A^2} + \frac{x_A - \hat{x}_B + 2r\cos\phi}{\sigma_B^2} = 0, \tag{6.28}$$

$$\frac{y_A - \hat{y}_A}{\sigma_A^2} + \frac{y_A - \hat{y}_B + 2r\sin\phi}{\sigma_B^2} = 0, \tag{6.29}$$

$$x_A\sin\phi - \hat{x}_B\sin\phi - y_A\cos\phi + \hat{y}_B\cos\phi = 0. \tag{6.30}$$

Combining (6.28) and (6.29) gives us,

$$\tan\phi = \frac{\frac{y_A-\hat{y}_B}{\sigma_B^2} + \frac{y_A-\hat{y}_A}{\sigma_A^2}}{\frac{x_A-\hat{x}_B}{\sigma_B^2} + \frac{x_A-\hat{x}_A}{\sigma_A^2}}. \tag{6.31}$$

Dividing (6.30) by $\cos\phi$ gives us,

$$\begin{aligned} \tan\phi &= \frac{y_A - \hat{y}_B}{x_A - \hat{x}_B} && (6.32)\\ &= \frac{\frac{y_A-\hat{y}_B}{\sigma_B^2}}{\frac{x_A-\hat{x}_B}{\sigma_B^2}}. && (6.33) \end{aligned}$$

Combining (6.31) and (6.33) we have,

$$\begin{aligned} \tan\phi &= \frac{\frac{y_A-\hat{y}_B}{\sigma_B^2}}{\frac{x_A-\hat{x}_B}{\sigma_B^2}} = \frac{\frac{y_A-\hat{y}_A}{\sigma_A^2}}{\frac{x_A-\hat{x}_A}{\sigma_A^2}} = \frac{y_A - \hat{y}_A}{x_A - \hat{x}_A} && (6.34)\\ &= \frac{\hat{y}_B - \hat{y}_A}{\hat{x}_B - \hat{x}_A}. && (6.35) \end{aligned}$$

The result in (6.33) and (6.35) implies that, $\mathbf{l}^A = [x_A, y_A]^T$ lies on the line that connects $\hat{\mathbf{l}}^A$ and $\hat{\mathbf{l}}^B$.

Moreover, rewriting (6.28) and (6.29), we have,

$$\begin{aligned} x_A &= \frac{\sigma_B^2\hat{x}_A + \sigma_A^2\hat{x}_B - 2r\sigma_A^2\cos\phi}{\sigma_A^2 + \sigma_B^2}, && (6.36)\\ y_A &= \frac{\sigma_B^2\hat{y}_A + \sigma_A^2\hat{y}_B - 2r\sigma_A^2\sin\phi}{\sigma_A^2 + \sigma_B^2}. && (6.37) \end{aligned}$$

Consequently,

$$\begin{aligned} x_B &= \frac{\sigma_B^2\hat{x}_A + \sigma_A^2\hat{x}_B + 2r\sigma_B^2\cos\phi}{\sigma_A^2 + \sigma_B^2}, && (6.38)\\ y_B &= \frac{\sigma_B^2\hat{y}_A + \sigma_A^2\hat{y}_B + 2r\sigma_B^2\sin\phi}{\sigma_A^2 + \sigma_B^2}. && (6.39) \end{aligned}$$

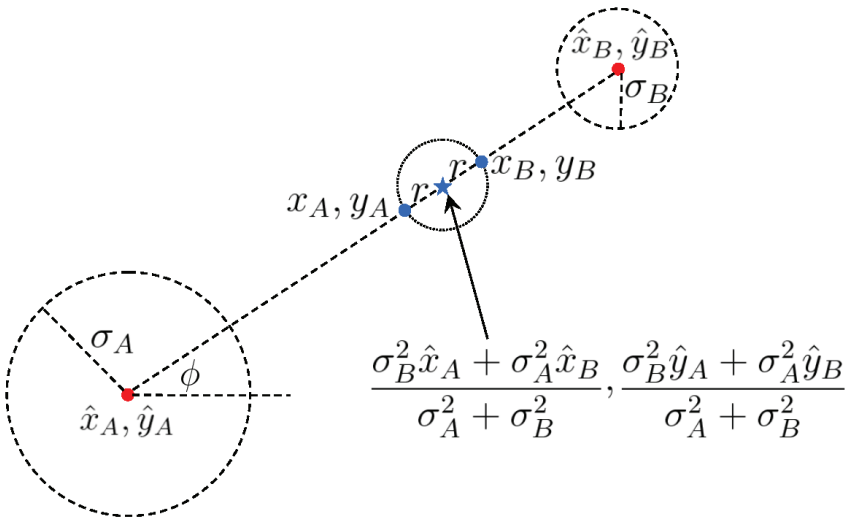

Fig. 6.1: Illustration for the geometry of the solution.

An illustration for the geometry of the solution is shown in Fig. 6.1. After fusion, both location estimates $\mathbf{l}^A$ and $\mathbf{l}^B$ lie on the line that connects $\hat{\mathbf{l}}^A$ and $\hat{\mathbf{l}}^B$. Moreover, $\mathbf{l}^A$ and $\mathbf{l}^B$ are both r meters away from the location which is the weighted average of $\hat{\mathbf{l}}^A$ and $\hat{\mathbf{l}}^B$, from both sides.

In practice, it is difficult to calibrate or estimate the real-time tracking error variances of the two modules. In the case where two devices are mounted at symmetrical locations on the same pedestrian's body, we assume the two sensor modules have equal variances.

6.4 The Special Case:A Single Device with Two Different Orientation Sensors

In the special case, where there is only one device, containing two different orientation sensors (e.g., gyroscope and magnetometer), our proposed scheme can

also be applied, as follows.

We compute two different DR estimates, $\mathbf{l}_i^A$ and $\mathbf{l}_i^B$, each utilizing one of the orientation sensors for heading direction, as well as the accelerometer for step detection. Next, because the two sets of estimates are from the same physical device, they experience the same random body movements. Therefore, we assume their DR tracking error variances to be equal. We also note that, $\|\mathbf{l}_i^A - \mathbf{l}_i^B\| = 0$ for all i as far as the same physical device is concerned. The generalized fusion algorithm becomes a simple mean computation for each detected step in this case.

6.5 Experiments and Discussions

6.5.1 Experimental Testbed Setup and Devices Used

In order to evaluate the performance of the proposed scheme, we use the same testbed setup as described in Chapter 5.

We have conducted experiments for two different scenarios. As shown in Fig. 6.2(a), in Scenario 1, we have used both Google NexusOne (Slave A) and HTC Magic (Slave B) as the slave devices, each containing a 3-axis digital compass for heading detection and a 3-axis accelerometer for step detection, carried with arbitrary device orientations in the pedestrian's two trouser pockets. We also use one HTC Hero as the master device for experiment control and ground truth collection purpose.

As shown in Fig. 6.2(b), in Scenario 2, we have used the Apple iPhone 4 as the slave device, containing both a 3-axis magnetometer (Slave compass) and a 3-axis gyroscope (Slave gyro) for heading detection, and a 3-axis accelerometer for step detection, mounted with fixed orientation on the pedestrian's side waist. We also use the Google NexusOne as the master device for experiment control and

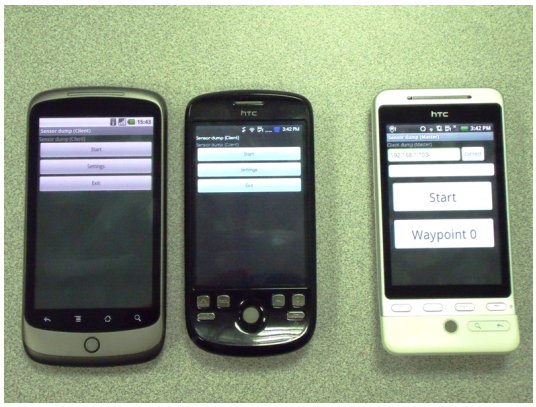

(a) Data collection devices for Scenario 1, from left to right: Google NexusOne (Slave A); HTC Magic (Slave B); HTC Hero (Master).

(b) Data collection devices for Scenario 2, from left to right: Apple iPhone 4 (Slave) and Google NexusOne (Master).

Fig. 6.2: Experimental devices for two testing scenarios.

ground truth collection purpose.

Note that, our proposed method itself does not require the user to carry multiple smartphones in practice. Instead, mobile devices such as a mobile phone, a tablet PC, or even a DR sensor set embedded in a customized key chain, can be grouped flexibly to form multiple sensor sets.

6.5.2 System Synchronization

The synchronization scheme between multiple smartphones are similar as the synchronization scheme between a smartphone and the PC in Chapter 5. All the devices are connected to the same Wi-Fi router for experimental purposes. Each smartphone records data using its own local clock with millisecond time resolution. The synchronization between the phones in both scenarios is performed as follows. As soon as the pedestrian taps the "Start" button on the master, it records down its local timestamp T_1, and sends out a START message to each slave. The slave records its local timestamp, T_2, and replies with an ACK message

immediately, when it receives the START message. The master records down the local timestamp T_3 when the ACK message is received from the slave. We assume both the START message and ACK message between master and slave take the same amount of transmission time. In order to synchronize with each other, the master subtracts $(T_1 + T_3)/2$ from all of its local timestamps, while the slave subtracts T_2 from all of its local timestamps.

6.5.3 Ground Truth Collection

The ground truth collection scheme is performed in the same way, using the smartphone's touch screen interface, as that in Chapter 5.

6.5.4 Tracking Performance

Performance with Two Devices

Fig. 6.3 shows the average location tracking error for Scenario 1, before and after the proposed fusion algorithm is applied, for 10 experimental trials. The radius of the local random movement sphere, r, is 0.075 m in this case, considering both modules' random local movements in the pedestrian's trouser pockets.

As shown in the figure, the effects of the proposed scheme can be categorized into two different cases.

In the first case (Trial 3, 4, 5, 6, and 8), both devices' average tracking errors using traditional DR have been significantly reduced with our proposed fusion scheme. The largest error reduction rate is reported in Trial 6 at 73.7%. We show the error propagation (Fig. 6.4) and actual tracking paths (Fig. 6.5) for this trial, as an example here. Fig. 6.5 shows that, individual DR systems of the two devices exhibit adverse error biases in location tracking estimates. On

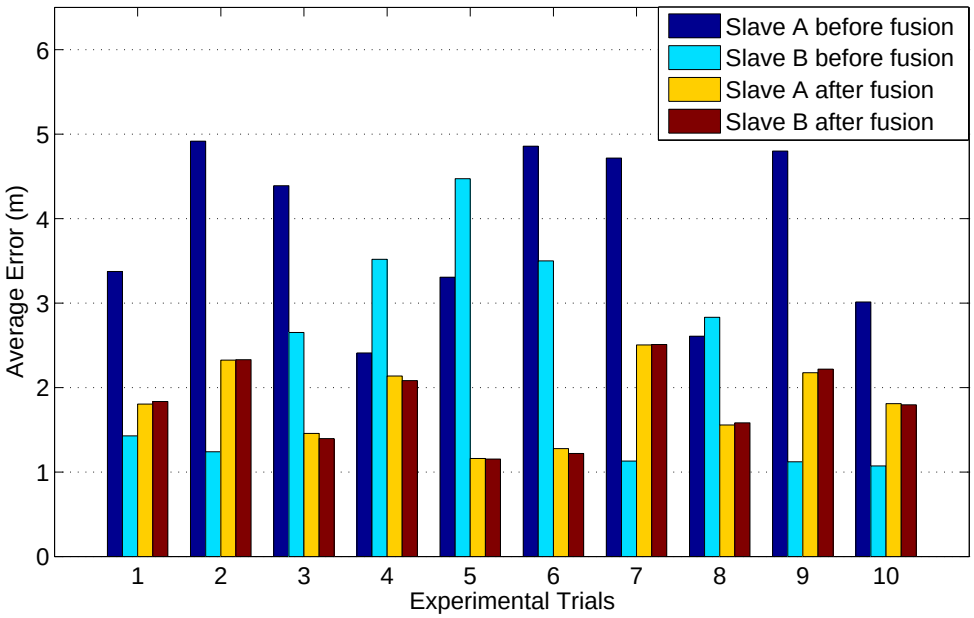

Fig. 6.3: Average tracking errors before and after fusion for 10 experimental trials for Scenario 1, using two devices, each containing one magnetometer as orientation sensor, mounted with arbitrary orientations.

the other hand, Fig. 6.4 shows that the difference between the magnitudes of the two devices' (adverse) error biases is not very significant. Therefore, the proposed scheme effectively cancels these error biases out, leaving small residual errors. As a result, the tracking errors of the proposed scheme for both devices are significantly smaller than those before fusion.

In the second case (Trial 1, 2, 7, 9, 10), the proposed algorithm delivers intermediate tracking performance, with average errors in between those of the two devices' individual DR systems. Here, we show the error propagation (Fig. 6.6) and actual tracking paths (Fig. 6.7) for Trial 7, as an example. Fig. 6.7 shows that, the two devices still give adverse error biases in location tracking estimates, as in the previous scenario. On the other hand, Fig. 6.6 shows that, the difference between the magnitudes of the two devices' (adverse) error biases is much larger than before; Device B's DR tracking error before fusion happens to be very small

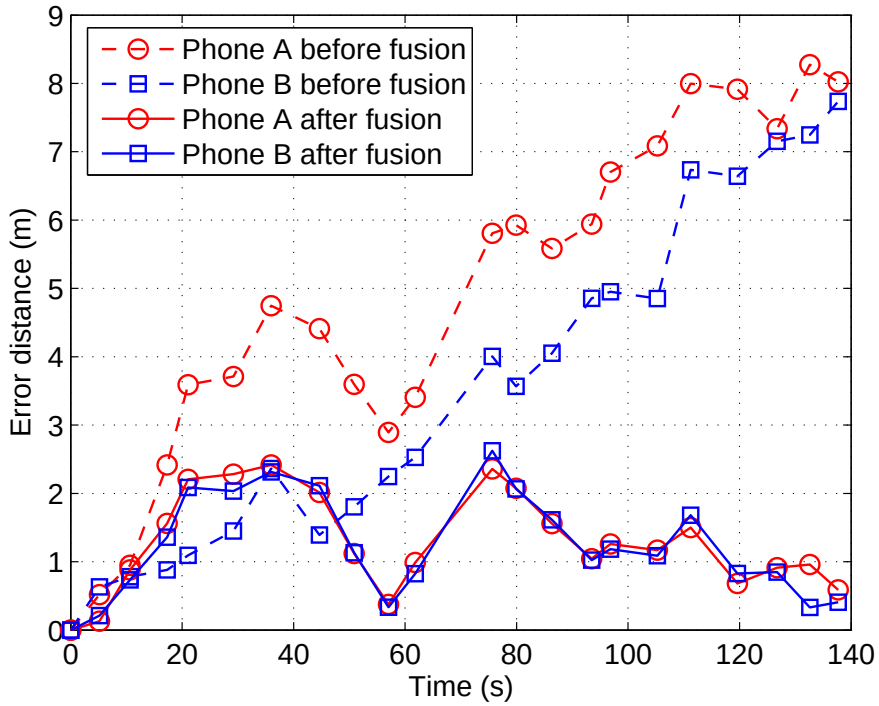

Fig. 6.4: Temporal error propagation before and after fusion for Trial 6.

in this particular trial. Therefore, even after the proposed scheme cancels part of the error bias out, a large residual error bias is still left in the fused results. Therefore, the tracking errors of the proposed scheme for the two devices are between those of the two device's original DR systems.

Performance with One Device

Fig. 6.8 shows the average location tracking error of Scenario 2, before and after the proposed fusion algorithm is applied, for 18 experimental trials. The radius of the local random movement sphere is 0 m in this case, because the two estimates are taken from the same physical device.

Similar to the previous case, the effects of the proposed scheme can be cate-

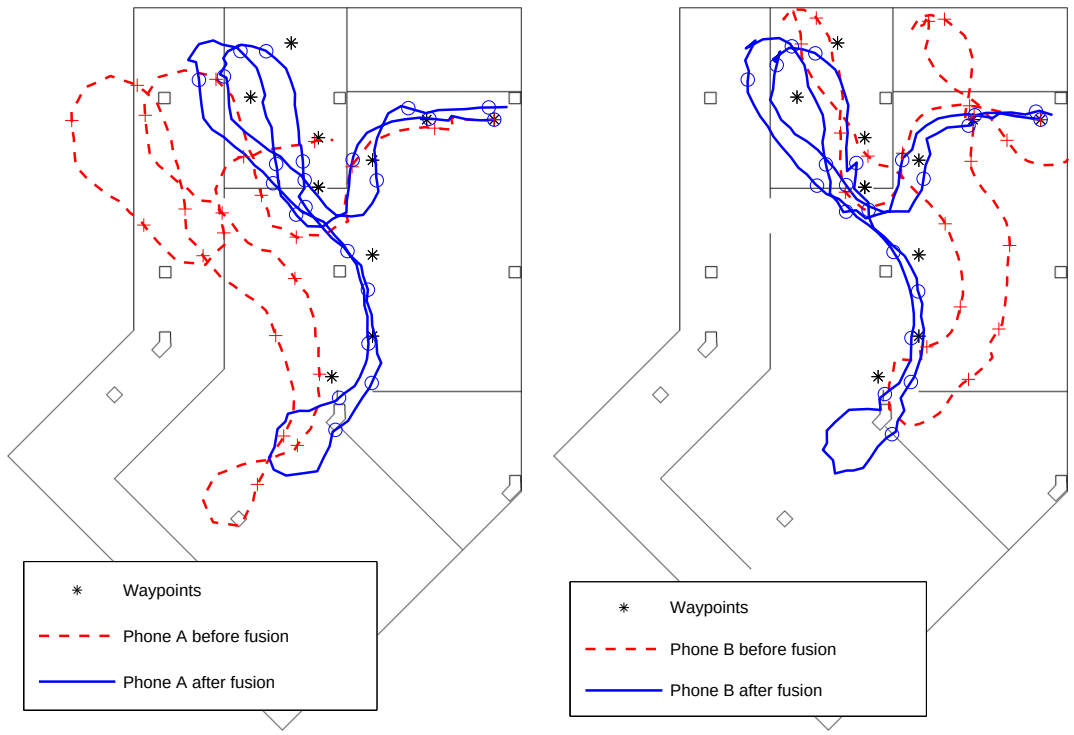

(a) Tracking paths before and after fusion for device A.

(b) Tracking paths before and after fusion for device B.

Fig. 6.5: Tracking paths before and after fusion for Trial 6.

gorized into two different cases.

In the first case, the proposed algorithm effectively reduces the average DR tracking error. For 13 out of 18 trials (Trial 2, 3, 4, 5, 7, 8, 9, 12, 13, 14, 16, 17, 18), both outputs' average tracking errors using traditional DR have been significantly reduced with our proposed fusion scheme. We show the error propagation (Fig. 6.9) and actual tracking paths (Fig. 6.11(a)) for Trial 4 as a typical example here. Fig. 6.11(a) shows that, the two individual DR outputs exhibit adverse error biases in location tracking estimates. On the other hand, Fig. 6.9 shows that the difference between the magnitudes of the two DR outputs' (adverse) error biases is not very big. Therefore, the proposed scheme effectively cancels out these error biases to a large extent, leaving small residual errors. As a result, the tracking

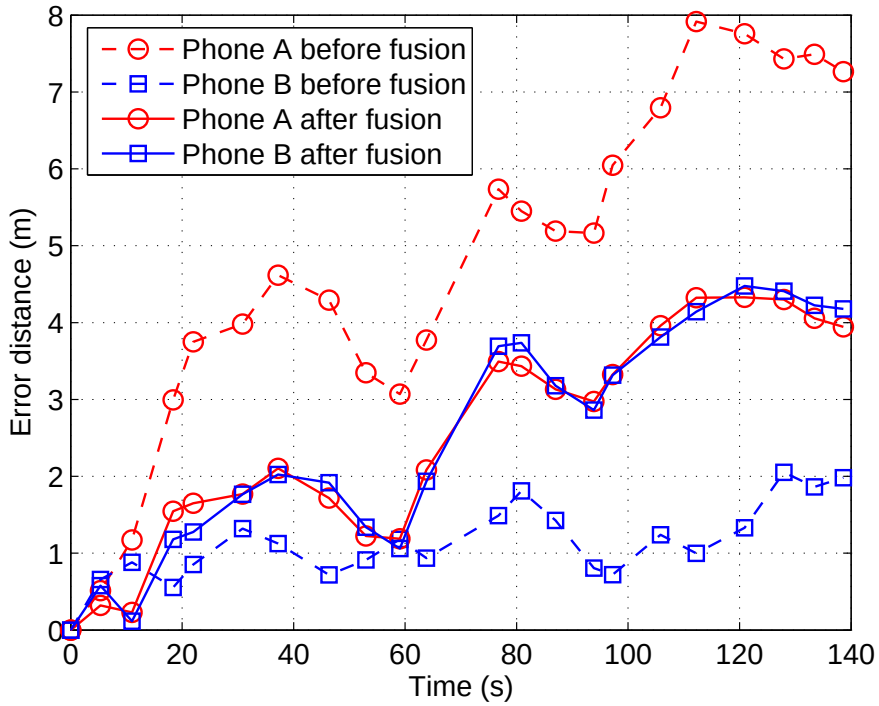

Fig. 6.6: Temporal error propagation before and after fusion for Trial 7.

errors of the proposed scheme for both outputs are significantly smaller than those before fusion, for most of the time.

In the second case, the proposed algorithm delivers intermediate tracking performance, with average errors in between those of the two individual DR outputs (Trial 1, 6, 10, 11, 15). Here, we show the error propagation (Fig. 6.10) and actual tracking paths (Fig. 6.11(b)) for Trial 11, as a typical example. Fig. 6.11(b) shows that, the two DR outputs still give adverse error biases in location tracking estimates, as in the previous scenario. On the other hand, Fig. 6.10 shows that, the difference between the magnitudes of the two outputs' (adverse) error biases is much larger than that observed in Fig. 6.9; Slave gyro's DR tracking error before fusion happens to be as large as in the previous case for this particular trial.

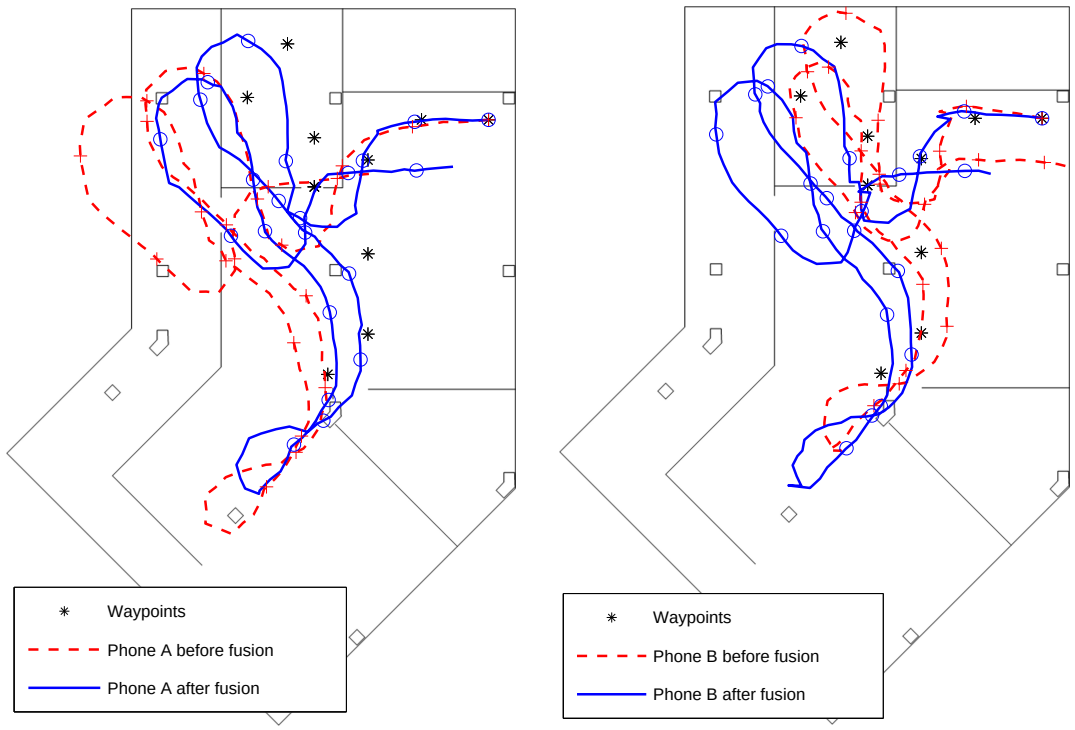

(a) Tracking paths before and after fusion for device A.

(b) Tracking paths before and after fusion for device B.

Fig. 6.7: Tracking paths before and after fusion for Trial 7.

However, Slave compass's error in this trial is much larger than before. Therefore, even after the proposed scheme cancels out part of the error bias, a large residual error bias is still left in the fused results. As a result, the tracking errors of the proposed scheme for the two outputs are between those of the two outputs' original DR systems.

In both scenarios, there are cases in which the proposed algorithm delivers intermediate tracking performance. However, we argue that, even in such cases, the proposed scheme is still useful, for two reasons. First, in practical application scenarios, it is hard, if not impossible, for the pedestrian user to determine which one of the two DR outputs is providing better tracking performance, especially when both are from the same physical device. This instability in performance is

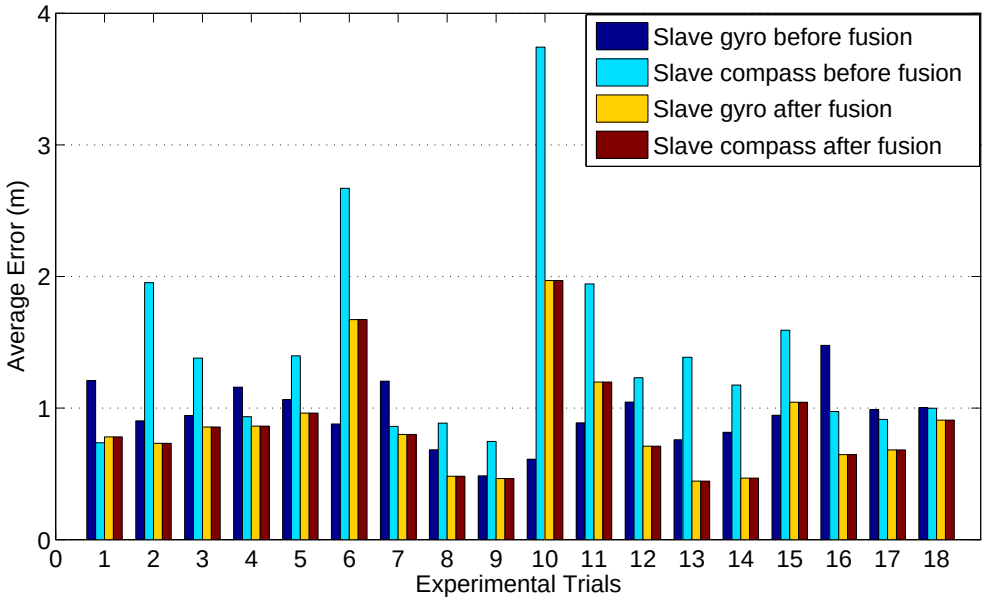

Fig. 6.8: Average tracking errors before and after fusion for 18 experimental trials for Scenario 2, using one device, containing two different orientation sensors, mounted with fixed device orientation.

also observed in our 18 experimental trials. Second, the absolute error reduction by the proposed scheme, from the more erroneous DR estimate, is significantly larger than the error that it has raised, from the estimate with small original errors. Overall, the proposed scheme is still giving robust and stable tracking performance.

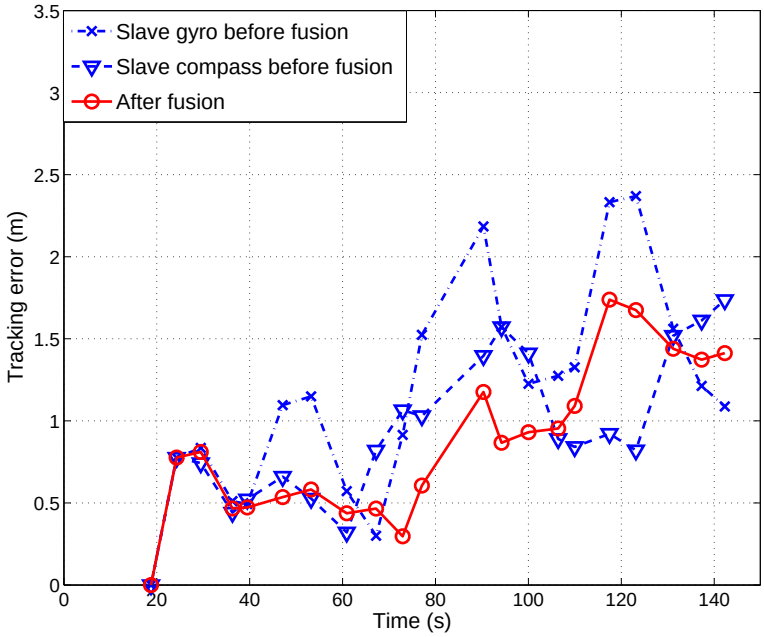

Fig. 6.9: Temporal error propagation before and after fusion for Trial 4.

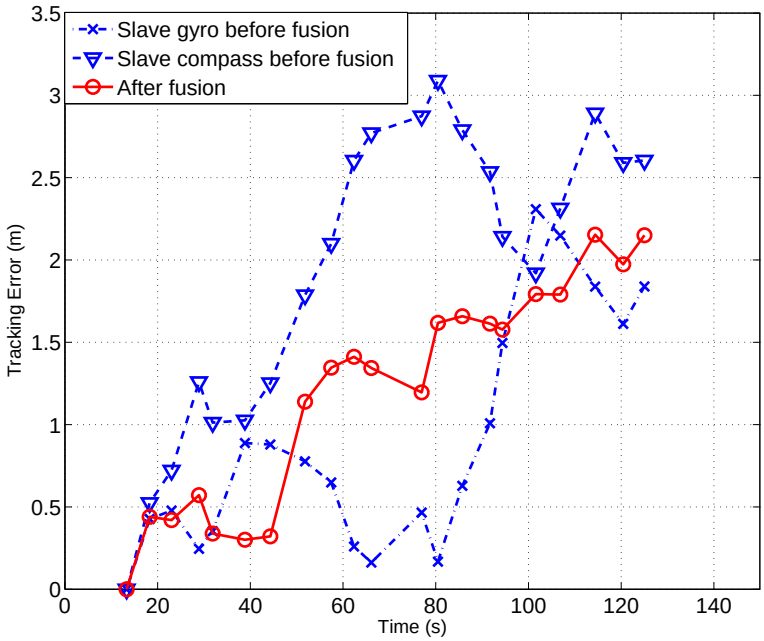

Fig. 6.10: Temporal error propagation before and after fusion for Trial 11.

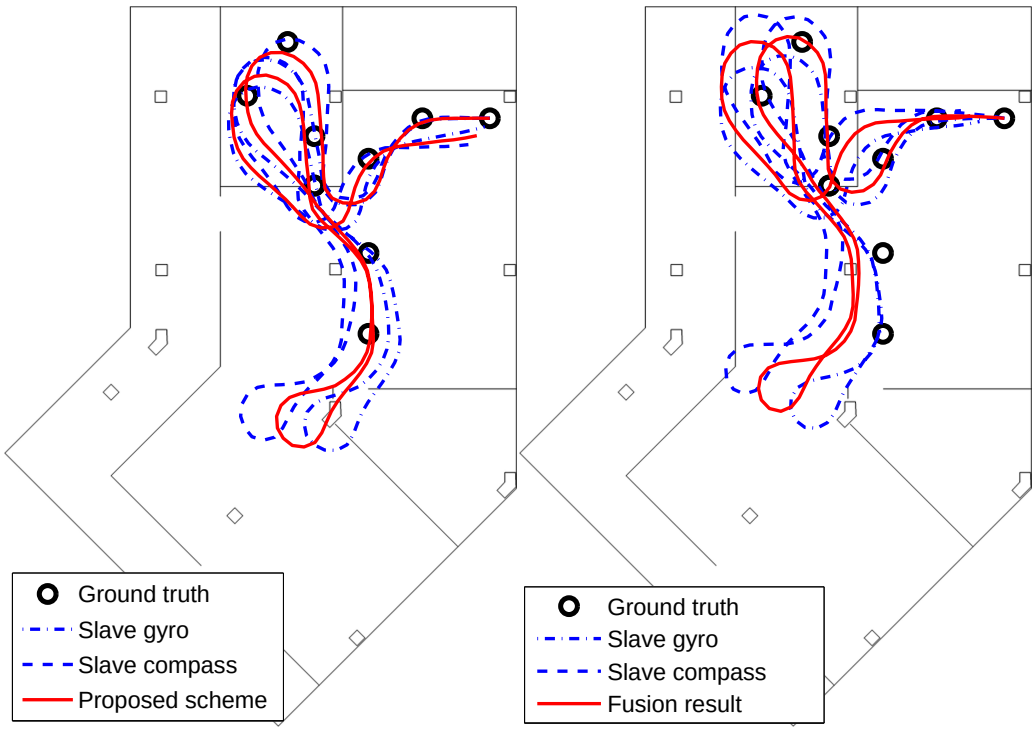

(a) Tracking paths before and after fusion for Trial 4.

(b) Tracking path before and after fusion for Trial 11.

Fig. 6.11: Tracking paths for two typical cases.

Chapter 7

Conclusion and Future Work

In this thesis, we have devoted our research efforts on the algorithms and performance analysis for practical indoor location tracking systems. Taking practical factors, such as system cost-effectiveness and indoor NLoS conditions, into consideration, we have chosen to focus our investigation into tracking methods that are based on existing wireless infrastructure and commercially accessible hand-held mobile devices with low cost MEMS sensors.

7.1 CIR-based Location Fingerprinting

The widely adopted RSS-fingerprint-based localization method is not only labor-intensive but also vulnerable to environmental changes after the training is completed. In Chapter 3, we proposed a CIR-based location fingerprint which can be efficiently derived from receiver's channel estimation. We have also developed the associated signal processing technique which transforms the fingerprint vector into logarithmic scale in order to eliminate the effect of propagation path loss and ensure each element in the fingerprint vector contributes fairly to the location

estimation.

Simulation results using a realistic indoor propagation simulator have shown that, the proposed CIR-based fingerprint and its associate logarithmic transformation exhibit superior performance advantage, compared to traditional RSS fingerprint-based methods, and also the scheme which combines neural network and extracted features from CIR. The significance of improvement in accuracy is verified under different bandwidth conditions. Results have also shown that, our proposed scheme is not only robust to real-time channel variations caused by random positions and orientations of human bodies, but is also more efficient in utilizing hardware infrastructure and training effort, compared to other schemes proposed in the literature.

We suggest two future directions based on this work. First, since channel estimation results are currently not accessible in off-the-shelf products, we aim to search or implement transceiver modules with suitable size and RF specifications, in order to verify our proposed method in a realistic and extended testbed. Second, our work in this thesis focuses on the task of locating static users. In practice, the users are moving from time to time. Making use of the real time variation of the channel-related information for mobile user tracking will be a challenging task which is worth exploring.

7.2 Error Analysis for Fingerprint-based Localization Systems

Very few works in the literature study the online error performance for location fingerprinting systems theoretically. Some existing solutions study only certain special cases, while others are validated empirically, without any theoreti-

cal justifications.

In Chapter 4, we derive the exact theoretical expressions of both the online error PDF and RoC for a generalized location fingerprinting system. Computations of both terms require the unknown joint PDF for the target location and the online signal parameter vector. We therefore propose to approximate this joint PDF by nonparametric kernel density estimation using the training fingerprints, without any extra calibration. Experimental results have shown that, the proposed scheme predicts the empirical error PDF closely for the two most popular location fingerprinting methods, namely, K nearest neighbour and the probabilistic approach, in a practical indoor testbed.

The online error PDF and RoC computations for a fingerprinting system require both training and online data. However, for ToA-based trilateration and DoA-based triangulation, only online received signals are present. Therefore, dedicated theoretical analysis, calibration efforts, and numerical techniques are required in order to obtain the error statistics for the geometric localization approach.

7.3 DR-based Robust Pedestrian Tracking

This thesis has taken two different approaches in realization of DR-based robust pedestrian tracking on top of hand-held devices with low cost MEMS sensors.

In Chapter 5, we present our first approach, which fuses the output of a DR sub-system and a sparsely deployed ranging sub-system. We have adopted the SIR PF-based approach to incorporate both DR and range measurements. In order to verify the effectiveness of the proposed system, we have implemented an indoor tracking system using the sensors on a hand-held mobile device and a

ranging system using Cricket technology. Experimental results have shown that, the proposed system not only delivers much better tracking performance compared to the DR approach, but also eliminates the location uncertainty rapidly and provides satisfactory tracking accuracy even when the initial user location is unknown. More importantly, even with very sparse and intermittent infrastructure support, in both time and space domains, the proposed scheme is still able to deliver significant improvements in tracking performance compared to DR alone.

In Chapter 6, we present our second approach, which exploits the stability of relative displacements between DR modules carried by the same pedestrian. We have formulated the robust tracking algorithm as a MAP sensor fusion problem, derived the optimal fusion solution, and then narrowed it to a special case for a single physical device. Prototypes of the proposed system, as well as an effective indoor ground truth collection system have been implemented with accompanying performance evaluation. The proposed scheme has shown significant performance improvement in a realistic indoor testbed when using (i) two sensor modules each containing a single orientation sensor, mounted with arbitrary device orientation, (ii) one sensor module containing two different orientation sensors, mounted with fixed device orientation.

We point out two future directions based on our work in robust DR pedestrian tracking. First, in both approaches, we have used a very simple assumption for DR error variance in order to simplify the solutions. A deeper understanding and better modelling of real-time DR error properties would definitely help make our proposed schemes more robust and effective. Second, map-matching technologies can also be fused into the proposed schemes to further reduce tracking error.

Bibliography

[1] H. Zang, F. Baccelli, and J. Bolot, "Bayesian inference for localization in cellular networks," in *Proc. IEEE INFOCOM*, pp. 1963–1971, Mar. 2010.

[2] R. Tesoriero, J. A. Gallud, M. ía D. Lozano, and V. M. R. Penichet, "Tracking autonomous entities using RFID technology," *IEEE Trans. Consumer Electronics*, vol. 55, pp. 650–655, May 2009.

[3] S. S. Saab and Z. S. Nakad, "A standalone RFID indoor positioning system using passive tags," *IEEE Trans. Industrial Electronics*, vol. 58, pp. 1961–1970, May 2011.

[4] N. B. Priyantha, A. Chakraborty, and H. Balakrishnan, "The Cricket location-support system," in *Proc. ACM MOBICOM*, pp. 32–43, 2000.

[5] Time Domain, *Time Domain Real Time Location System.* `http://http://www.timedomain.com`.

[6] R. Yamasaki, A. Ogino, T. Tamaki, T. Uta, N. Matsuzawa, and T. Kato, "TDOA location system for IEEE 802.11b WLAN," in *Proc. IEEE WCNC*, pp. 2338–2343, Mar. 2005.

[7] G. Giorgetti, A. Cidronali, S. K. S. Gupta, and G. Manes, "Single-anchor indoor localization using a switched-beam antenna," *IEEE Communications Letters*, vol. 13, pp. 58–60, Jan. 2009.

[8] R. O. Schmidt, "Multiple emitter location and signal parameter estimation," *IEEE Trans. Antennas Propagation*, vol. AP-34, pp. 276–280, Mar. 1986.

[9] B. N. Hood and P. Barooah, "Estimating DoA from radio-frequency RSSI measurements using an actuated reflector," *IEEE Sensors Journal*, vol. 11, pp. 413–417, Feb. 2011.

[10] S. A. Golden and S. S. Bateman, "Sensor measurements for Wi-Fi location with emphasis on time-of-arrival ranging," *IEEE Trans. Mobile Computing*, vol. 6, pp. 1185–1198, Oct. 2007.

[11] M. Ciurana, F. Barcelo-Arroyo, and F. Izquierdo, "A ranging method with IEEE 802.11 data frames for indoor localization," in *Proc. IEEE WCNC*, pp. 2092–2096, Mar. 2007.

[12] P. Bahl and V. Padmanabhan, "RADAR: An in-building RF-based user location and tracking system," in *Proc. IEEE INFOCOM*, pp. 775–784, Mar. 2000.

[13] R. Roy and T. Kailath, "ESPRIT - Estimation of signal parameters via rotational invariance techniques," *IEEE Trans. ASSP*, vol. 37, pp. 984–995, Jul. 1989.

[14] H. Krim and M. Viberg, "Two decades of array signal processing research: the parametric approach," *IEEE Signal Processing Magazine*, vol. 13, pp. 67–94, Jul. 1996.

[15] T. J. Shan, M. Wax, and T. Kailath, "On spatial smoothing for direction of arrival estimation of coherent signals," *IEEE Trans. ASSP*, vol. 33, pp. 806–811, Apr. 1985.

[16] N. Patwari, J. N. Ash, S. Kyperountas, A. O. I. Hero, R. L. Moses, and N. S. Correal, "Locating the nodes: cooperative localization in wireless sensor networks," *IEEE Signal Processing Magazine*, vol. 22, pp. 54–69, Jul. 2005.

[17] K. Pahlavan, X. Li, and J. P. Makela, "Indoor geolocation: science and technology," *IEEE Communications Magazine*, vol. 40, pp. 112–118, Feb. 2002.

[18] X. Li and K. Pahlavan, "Super-resolution TOA estimation with diversity for indoor geolocation," *IEEE Trans. Wireless Communication*, vol. 3, pp. 224–234, Jan. 2004.

[19] J. Y. Lee and R. A. Scholtz, "Ranging in a dense multipath environment using an UWB radio link," *IEEE JSAC*, vol. 20, pp. 1677–1683, Dec. 2002.

[20] H. Lim, L.-C. Kung, J. C. Hou, and H. Luo, "Zero-configuration, robust indoor localization: theory and experimentation," in *Proc. IEEE INFOCOM*, pp. 1–12, Apr. 2006.

[21] Y. T. Chan and K. C. Ho, "A simple and efficient estimator for hyperbolic location," *IEEE Trans. Signal Processing*, vol. 42, pp. 1905–1915, Aug. 1994.

[22] B. T. Fang, "Simple solutions for hyperbolic and related position fixes," *IEEE Trans. Aerospace and Electronic Systems*, pp. 748–753, Sep. 1990.

[23] Y. T. Chan, W. Y. Tsui, and P. C. Ching, "Time-of-Arrival based localization under NLOS conditions," *IEEE Trans. Vehicular Technology*, vol. 55, pp. 17–24, Jan. 2006.

[24] H. Miao, K. Yu, and M. J. Juntti, "Positioning for NLOS propagation: algorithm derivations and Cramer-Rao bounds," *IEEE Trans. Vehicular Technology*, vol. 56, pp. 2568–2580, Sep. 2007.

[25] C. K. Seow and S. Y. Tan, "Non-Line-of-Sight localization in multipath environments," *IEEE Trans. Mobile Computing*, vol. 7, pp. 647–660, May 2008.

[26] M. Brunato and R. Battiti, "Statistical learning theory for location fingerprinting in wireless LANs," *Computer Networks*, vol. 47, pp. 825–845, Apr. 2005.

[27] P. Myllymäki, T. Roos, H. Tirri, P. Misikangas, and J. Sievänen, "A probabilistic approach to WLAN user location estimation," *International Journal of Wireless Information Networks*, vol. 9, pp. 155–164, Jul. 2002.

[28] A. Kushki, K. N. Plataniotis, and A. N. Venetsanopoulos, "Kernel-based positioning in wireless local area networks," *IEEE Trans. Mobile Computing*, vol. 6, pp. 689–705, Jun. 2007.

[29] D. W. Scott, *Multivatiate Density Estimation, Theory, Practice, and Visualization*. Wiley-Interscience, 1992.

[30] C. Nerguizian, C. Despins, and S. Affés, "Geolocation in mines with an impulse response fingerprinting technique and neural networks," *IEEE Trans. Wireless Communications*, vol. 5, pp. 603–611, Mar. 2006.

[31] H. Wu, M. Siegel, R. Stiefelhagen, and J. Yang, "Sensor fusion using Dempster-Shafer theory," in *Proc. IEEE IMTC*, pp. 7–12, 2002.

[32] N. Swangmuang and P. Krishnamurthy, "Location fingerprint analyses toward efficient indoor positioning," in *Proc. IEEE PERCOM*, pp. 100–109, Mar. 2008.

[33] J. Yang and Y. Chen, "A theoretical analysis of wireless localization using RF-based fingerprint matching," in *Proc. IEEE IPDPS*, pp. 1–6, Apr. 2008.

[34] Y. Gwon, R. Jain, and T. Kawahara, "Robust indoor location estimation of stationary and mobile users," in *Proc. IEEE INFOCOM*, pp. 1032–1043, Mar. 2004.

[35] Y. K. Thong, M. S. Woolfson, J. A. Crowe, B. R. Hayes-Gill, and R. E. Challis, "Dependence of inertial measurements of distance on accelerometer noise," *Meas. Sci. Technol.*, vol. 13, pp. 1163–1172, 2002.

[36] E. Foxlin, "Pedestrian tracking with shoe-mounted inertial sensors," *IEEE Computer graphics and applications*, vol. 25, pp. 38–46, Nov.-Dec. 2005.

[37] S. Beauregard, "Omnidirectional pedestrian navigation for first responders," in *Proc. IEEE WCNC*, pp. 33–36, Mar. 2007.

[38] L. Ojeda and J. Borenstein, "Personal dead-reckoning system for GPS-denied environents," in *Proc. IEEE SSRR*, pp. 1–6, Sep. 2007.

[39] L. Fang, P. J. Antsaklis, L. A. Montestruque, M. B. McMickell, M. Lemmon, Y. Sun, H. Fang, I. Koutroulis, M. Haenggi, M. Xie, and X. Xie, "Design of a wireless assisted pedestrian dead reckoning system –The NavMote experience," *IEEE Trans. Instrumentation and Measurement*, vol. 54, pp. 2342–2358, Dec. 2005.

[40] S. Beauregard, "A helmet-mounted pedestrian dead reckoning system," in *Proc. IFAWC*, Mar. 2006.

[41] D. Mizell, "Using gravity to estimate accelerometer orientation," in *Proc. IEEE ISWC*, pp. 252–253, Nov. 2003.

[42] K. Kunze, P. Lukowicz, K. Partridge, and B. Begole, "Which way am I facing: inferring horizontal device orientation from an accelerometer signal," in *Proc. IEEE ISWC*, pp. 149–150, Sep. 2009.

[43] U. Steinhoff and B. Schiele, "Dead reckoning from the pocket - an experimental study," in *Proc. IEEE PERCOM*, pp. 162–170, Mar. 2010.

[44] Z. Li and W. Chen, "A new approach to map-matching and parameter correcting for vehicle navigation system in the area of shadow of GPS signal," in *Proc. IEEE ITS*, pp. 449–454, Sep. 2005.

[45] R. Jirawimut, P. Ptasinski, V. Garaj, F. Cecelja, and W. Balachandran, "A method for dead reckoning parameter correction in pedestrian navigation system," *IEEE Trans. Instrumentation and Measurement*, vol. 52, pp. 209–215, Feb. 2003.

[46] R. K. A. Owusu, "Particle filtering and information fusion of innovative location and tracking device targeting GPS hostile environments," in *Proc. IEEE ISABEL*, pp. 1–7, Oct. 2008.

[47] D. Kurth, G. Kantor, and S. Singh, "Experimental results in range-only localization with radio," in *Proc. IEEE IROS*, pp. 974–979, Oct. 2003.

[48] H. Wang, H. Lenz, A. Szabo, J. Bamberger, and U. D. Hanebeck, "WLAN-based pedestrian tracking using particle filters and low-cost MEMS sensors," in *IEEE WPNC*, pp. 1–7, Mar. 2007.

[49] T. S. Rappaport, *Wireless Communications, Principles and Practice*. Prentice Hall, 2002.

[50] J.-J. van de Beek, O. Edfors, M. Sandell, S. K. Wilson, and P. O. Börjesson, "On channel estimation in OFDM systems," in *Proc. IEEE VTC*, pp. 815–819, Jul. 1995.

[51] I. Rhodes, "Tutorial introduction to estimation and filtering," *IEEE Trans. Automatic Control*, vol. 16, pp. 688–706, Dec. 1971.

[52] W. Hädle, M. Müller, S. Sperlich, and A. Werwatz, *Nonparametric and Semiparametric Models*. Springer, 2004.

[53] B. W. Silverman, *Density Estimation for Statistics and Data Analysis*. Chapman and Hall, 1986.

[54] S. R. Saunders, *Antennas and Propagation for Wireless Communication Systems*. John Wiley & Sons, 1999.

[55] ACTIX, *Radioplan Product Overview*. `http://www.actix.com/Docs/OurProducts/Radioplan/ActixRadioplanProductOverview.pdf`.

[56] H. Yang, M. H. A. J. Herben, and P. F. M. Smulders, "Indoor radio channel fading analysis via deterministic simulations at 60 GHz," in *Proc. ISWCS*, pp. 144–148, 2006.

[57] A. Papoulis and S. U. Pillai, *Probability, Random Variables and Stochastic Processes*. McGraw-Hill, 2002.

[58] D. F. Specht, "A general regression neural network," *IEEE Trans. Neural Networks*, vol. 2, pp. 568–576, Nov. 1991.

[59] H. Weinberg, *Using the ADX1202 in pedometer and personal navigation applications*. Analog Devices, 2002. `http://www.analog.com/static/imported-files/application_notes/513772624AN602.pdf`.

[60] M. S. Arulampalam, S. Maskell, N. Gordon, and T. Clapp, "A tutorial on particle filters for online nonlinear/non-Gaussian bayesian tracking," *IEEE Trans. Signal Processing*, vol. 50, pp. 174–188, Feb. 2002.

List of Publications

1. Y. Jin, H.-S. Toh, W.-S. Soh, and W.-C. Wong, "Robust dead-reckoning pedestrian tracking system with low cost sensors," *Elsevier Journal on Pervasive and Mobile Computing* (as an extension of the IEEE PERCOM paper, currently under revision).

2. Y. Jin, W.-S. Soh, M. Motani, J. Zhang, and W.-C. Wong, "A robust indoor pedestrian tracking system with sparse infrastructure support," *IEEE Transactions on Mobile Computing* (currently under review).

3. Y. Jin, W.-S. Soh, and W.-C. Wong, "Error analysis for fingerprint-based localization," *IEEE Communications Letters,* vol. 14, no. 5, pp. 393-395, May 2010.

4. Y. Jin, W.-S. Soh, and W.-C. Wong, "Indoor localization with channel impulse response based fingerprint and nonparametric regression," *IEEE Transactions on Wireless Communications,* vol. 9, no. 3, pp. 1120-1127, Mar. 2010.

5. Y. Jin, H.-S. Toh, W.-S. Soh, and W.-C. Wong, "Robust dead-reckoning pedestrian tracking system with low cost sensors," in *Proc. IEEE PERCOM,* pp. 222-230, Mar. 2011.

6. Y. Jin, M. Motani, W.-S. Soh, and J. Zhang, "SparseTrack: Enhancing indoor pedestrian tracking with sparse infrastructure support," in *Proc. IEEE INFOCOM,* pp. 1-9, Mar. 2010.

7. A. K. M. Mahtab Hossain, H. Nguyen Van, Y. Jin, and W.-S. Soh, "Indoor localization using multiple wireless technologies," in *Proc. IEEE MASS,* pp. 1-8, Oct. 2007.